CENTRO DE INVESTIGACIÓN Y DE ESTUDIOS AVANZADOS DEL INSTITUTO POLITÉCNICO NACIONAL

UNIDAD QUERETARO

ANISOTROPÍAS MAGNÉTICAS DE PRIMEROS PRINCIPIOS

Tesis que presenta

Luis Enrique Díaz Sánchez

para obtener el Grado de

Doctor en Ciencias

en la Especialidad de

Materiales

Director de la Tesis: Dr. Aldo Humberto Romero Castro

Santiago de Querétaro, Qro.   Enero de 2009

Dedicada a:

Los mejores hijos del mundo
Yasodhara y Ulises
todo esto es por ustedes

Mi amada esposa
Lety
un paso mas en nuestro proyecto de vida

Mis padres
Fernando y Francisca
estoy aquí gracias a ustedes

Mis hermanos
Fernando y Dalia
sin ustedes la vida habría sido muy triste.

A mi sobrino
Ruy, "Mio Cid"
por las batallas que has de ganar

Acknowledgements

Anisotropías Magnéticas desde Primeros Principios

M. en C. Luis Enrique Díaz Sánchez

Resumen

De manera reciente, ha adquirido especial importancia entender el comportamiento magnético de los sistemas en los que la dirección del momento magné tico es no-colineal. Por no-colineal nos referimos a que los momentos magnéticos asociados con los iones del cristal no están alineados a lo largo de un mismo eje. Los dos formalismos teóricos básicos para el estudio y comprensión de este tipo de efecto magnético son la teoría de magnetismo no-colineal y la teoría de interacción espín-órbita. La teoría de magnetismo no-colineal permite considerar todos los grados de libertad del espín de los electrones, es decir, la dirección de la magnetización se convierte en una variable que cambia de manera continua con respecto a la posición. La no-colinealidad desacopla el espín de los electrones de la red cristalina. Una vez que el espín es desacoplado de la red, la interacción espín-órbita permite acoplar esta magnetización con el momento angular del electrón, el cual se mueve alrededor del núcleo. La interacción espín-órbita es también responsable de muchos otros fenómenos físicos, algunos de ellos presentados en este trabajo. Algo extraño es que la interacción espín-órbita es un efecto relativista que los investigadores no suelen tener en cuenta en los cálculos computacionales, incluso para los sistemas con elementos pesados en el que resulta necesario tener en cuenta dicha interacción. Por otro lado, la teoría funcional de la densidad es uno de los métodos más utilizados para realizar cálculos de dinámica molecular, *ab initio*, para estudiar las estructura de los átomos, moléculas, cristales, superficies y sus interacciones en general. Dentro de esta teoría es posible utilizar las dos aproximaciones mencionadas anteriormente, las cuales son importantes como ya se había mencionado, para estudiar las anisotropías magnéticas. En particular, hemos utilizado el código ABINIT, el cual es un código basado en la teoría funcional de densidad, para mostrar la importancia que tiene la interacción espín-órbita en el cálculo de propiedades vibracionales y termodinámicas para bismuto y antimonio. También estudiamos propiedades de magnetismo colineal y no colineal considerando al mismo tiempo la interacción espín-órbita, es decir, considerando ambas aproximaciones de manera simultanea para estudiar paladio y bismuto. En general este tipo de estudios han adquirido especial interés en entender no solo las anisotropías magnéticas, sino también la espintrónica, ondas de espín o magnetorresistencia gigante.

Magnetic anisotropies from first principles

M. en C. Luis Enrique Díaz Sánchez

Abstract

Nowadays, there is a growing realization of the importance of understanding the magnetic behaviour of systems in which the magnetic order is noncollinear. By noncollinear we mean that the magnetic moments associated with individual ions in the crystal are not aligned along the same axis. The two basic theoretical formalisms to study this kind of magnetic effect are the *noncollinear magnetism* and the *spin-orbit interaction* theories. The noncollinear magnetic theory permits to consider all the degrees of freedom in the spin of the electron, i.e., the direction of the magnetization becomes a continuous variable of position. The noncollinearity decouples the spin of the electron from the lattice of the crystal. Once the spin is decoupled from the lattice, the spin-orbit interaction permit to couple this magnetization with the angular magnetic moment of the electron that is moving around the nucleus. The spin-orbit interaction is also responsible for many others physical phenomena some of them presented in this work. Something unexpected is that the spin-orbit interaction is a relativistic effect that researchers not normally take into account in computational calculations even for systems with heavy elements where it might be necessary to consider this interaction. On the other hand, *density functional theory* is one of the most widely used methods for molecular dynamic *ab initio* calculations of the structure of atoms, molecules, crystals, surfaces, and their interactions. Within this theory it is possible to use both considerations, previously mentioned, which are important in studying magnetic anisotropies. In particular we used the ABINIT software, which is an *ab initio* code based in density functional theory, to show the importance role of the spin-orbit interaction in calculating vibrational and thermodynamic properties for *bismuth* and *antimony*. We also studied collinear and non collinear magnetic properties considering spin-orbit interaction, i.e., considering both approximations for *palladium* and bismuth. In general these kind of studies have acquired special interest in understanding not only magnetic anisotropies but also in *spintronic*, *spin waves*, or *giant magnetoresistance*.

Contents

List of Figures

List of Tables

Chapter 1

Introduction

At present theoretical computational physics has acquired importance due to the advances in different theories that have permitted to reproduce, demonstrate and predict experimental results in many kind of systems. In particular, at present the Density Functional Theory (DFT) is one of the most used theories that researchers have been used in order to understand ground states or excited states. These properties are important in studying electronic, magnetic and many others properties. The DFT has been mainly used because the simplicity of the theory and also because the reliability to implement such equations in an *ab initio* code.

The topic of this thesis "Magnetic anisotropies from first principles" was chosen because the interest, mine specially, that have grown in understand many properties like in spintronic, giant magnetoresistan, magnetic memories, or spin waves, just to give some examples. The basic theories to study these kind of magnetic effects are the the noncollinear magnetism and the spin-orbit interaction theory. The non-collinear magnetic theory permit to consider all the degrees of freedom in the spin of the electron. For that reason, the noncollinearity decouples the spin of the electron from the lattice of the crystal. Once the spin is decoupled from the lattice, the spin-orbit coupling is the responsible of coupling again this magnetization with the angular magnetic moment of the electron that is moving around the nucleus. The spin-orbit interaction is a relativistic effect normally not taken into account in computational calculations. Not considering this approximation is appropriate in studying light atoms because the energy contribution coming from the spin-orbit coupling is small compared to the rest of the total energy. Once one starts working with heavy atoms, transition metals and specially those above the five period in the periodic table, the inclusion of the spin-orbit interaction becomes crucial in order to reproduce experimental

1

results.

This thesis is divided in two main parts. In the *first part* the theoretical background about the density functional theory is explained in detail, though in a general way. The noncollinear magnetism and the spin-orbit interaction theories are the two main theories necessary to understand magnetic anisotropies. For that reason, we extended the treatment of both theories at the end of the first part. In the *second part* we focused mainly in applications. First, we show the important of considering the spin-orbit interaction relativistic effect in studying vibrational and thermodynamic properties for bismuth and antimony solids. In particular bismuth, with atomic number Z=83, is an ideal candidate to analyze the effect of the spin-orbit interaction on those perturbational properties. Because palladium clusters have magnetic properties, it is a good material to start analyzing noncollinear magnetic effects. We determine magnetic properties for palladium dimer using the spin-polarized approximation as a first step. In particular, we obtain the total energy of the dimer as a function of the magnetization at different fixed distances between palladium atoms. After this, we continue with a more general case according to our objectives, i.e., we consider the full charge density matrix in order to include the noncollinearity in the direction of the magnetization. The next step was to include the spin-orbit interaction approximation in the calculi. Continue with this treatment we finally use the full approximation, i.e., the noncollinear magnetic theory and the relativistic spin-orbit interaction effect were considered both at the same time to study palladium and bismuth dimers. Finally a theoretical like tight-binding study for bismuth atom is done in order to explain with a simple model the effect of the spin-orbit interaction on the independent electron energies (eigenvalues).

Finally, four appendixes are included. In the first one, we present the derivation of the density matrix and the spin density vector, usefull in the comprehension of the continuous variation of the orientation of the magnetization. The second one is devoted to explain the experimental setup used to experimentally measure phonon dispersion curves. This is done by observing the coherent inelastic scattering of monoenergetic neutrons due to a process in which a single phonon is created in a sample crystal. In the fourth appendix the experimental setup used to measure the heat capacity at low temperatures is presented. This quantity is determined by the pulse δQ supplied to the sample and the temperature rise δT, then the heat capacity is obtained by applying the identity $C = \delta Q / \delta T$. Finally the list of published papers in presented.

Part I

Background Theory

Chapter 2

Theory

2.1 Elements of solid state physics

2.1.1 adiabatic approximation

The *adiabatic approximation* is based on the fact that typical electronic velocities are much greater than typical ionic velocities. The significant electronic velocity is $v_e \approx 10^8 cm/sec$. On the other hand, typical ionic velocities are at most of order $10^5 cm/sec$. The ions can not follow the motion of the electrons and they see only a time-averaged adiabatic electronic potential. One therefore assumes that because the ions move so slowly on the scale of velocities of relevance to the electrons, at any moment the electrons will be in their ground state for that particular instantaneous ionic configuration, i.e., we can consider the electrons as moving in the field of fixed nuclei. That assumption comes from the fact that the mass of the nuclei are much higher than the mass of the electrons. Even the lightest of all nuclei, the proton (^{1}H), weighs roughly 1,800 times more than an electron, and for a typical nucleus such as carbon the mass ratio well exceeds 20,000. As a result, electrons can respond to ionic motion almost instantaneously or, in other words, to the electrons the ions are essentially stationary. In computing the Interatomic Force Constants (IFC), that will be explained later on, one must then supplement the interaction between ion cores with terms representing the dependence of the additional electronic energy on the instantaneous ionic configuration [1, 2].

The *adiabatic approximation* is also known as the Born-Oppenheimer. This is the basic approximation which allows one to decouple the vibrational from the electronic degrees of freedom in a solid [3]. Part of this approximation is to

assume that we can separate the electronic and nuclear coordinates and writing the total wavefunction as $\Psi = (\mathbf{r}, \mathbf{R}) = \phi(\mathbf{r})\Phi(\mathbf{R})$. With the Born-Oppenheimer approximation the Hamiltonian describing a perfect crystal can be expressed as the sum of three terms,

$$\hat{H} = \hat{H}_{ions}(\mathbf{R}_J) + \hat{H}_e(\mathbf{r}_i, \mathbf{R}_{J0}) + \hat{H}_{e-ion}(\mathbf{r}_i, \delta\mathbf{R}_J), \qquad (2.1)$$

where $\hat{H}_{ion}(\mathbf{R}_J)$ is the Hamiltonian describing the ionic motion under the influence of the ionic potential plus the time-averaged adiabatic electronic potential. $\hat{H}_e(\mathbf{r}_i, \mathbf{R}_{J0})$ is the Hamiltonian for the electrons with ions frozen in their equilibrium position $\mathbf{R}_{J0}$, and $\hat{H}_{e-ion}(\mathbf{r}_i, \delta\mathbf{R}_J)$ describes the changes in the electronic energy as a result of the displacements $\delta\mathbf{R}_J$ of the ions from their equilibrium position. $\hat{H}_{e-ion}$ is known as the *electron-phonon interaction* and is responsible for electrical resistance in reasonably pure semiconductors at room temperature [4].

2.1.1.1   Lattice dynamics from electronic-structure theory

Within the *adiabatic approximation*, the *lattice-dynamical* properties of a system are determined by the eigenvalues ε and eigenfunctions Φ of the Schrödinger equation [5]:

$$\left(-\sum_l \frac{\hbar^2}{2M_I} \frac{\partial^2}{\partial\mathbf{R}_I^2} + E(\mathbf{R}) \right) \Phi(\mathbf{R}) = \varepsilon\Phi(\mathbf{R}), \qquad (2.2)$$

where $\mathbf{R}_I$ is the coordinate of the Ith nucleus, M_I its mass, $\mathbf{R} \equiv \mathbf{R}_I$ is the set of all nuclear coordinates, and $E(\mathbf{R})$ the clamped-ion energy of the system, which is often referred to as the *Born-Oppenheimer energy surface*. In practice, $E(\mathbf{R})$ is the ground-state energy of a system of interacting electrons moving in the field of fixed nuclei, whose Hamiltonian - which acts onto the electronic variables and depends parametrically upon $\mathbf{R}$ - reads

$$H_{BO}(\mathbf{R}) = -\frac{\hbar^2}{2m} \sum_i \frac{\partial^2}{\partial\mathbf{r}_i^2} + \frac{e^2}{2} \sum_{i \neq j} \frac{1}{\mid \mathbf{r}_i - \mathbf{r}_j \mid} - \sum_{iI} \frac{Z_I e^2}{\mid \mathbf{r}_i - \mathbf{R}_I \mid} + E_N(\mathbf{R}),$$
$$(2.3)$$

where Z_I is the charge of the Ith nucleus, $-e$ is the electron charge, and $E_N(\mathbf{R})$ is the electrostatic interaction between different nuclei:

$$E_N(\mathbf{R}) = \frac{e^2}{2} \sum_{I \neq J} \frac{Z_I Z_J}{|\mathbf{R}_I - \mathbf{R}_J|}. \tag{2.4}$$

The equilibrium geometry of the system is given by the condition that the forces acting on individual nuclei vanish. This assumption comes from the fact that if the nuclei are fixed in space and do not move, their kinetic energy is zero and the potential energy due to the nucleolus-nucleus repulsion is merely a constant:

$$\mathbf{F}_I \equiv -\frac{\partial E(\mathbf{R})}{\partial \mathbf{R}_I} = 0, \tag{2.5}$$

whereas the vibrational frequencies ω are determined by the eigenvalues of the Hessian of the Born-Oppenheimer energy, scaled by the nuclear masses:

$$\det \left| \frac{1}{\sqrt{M_I M_J}} \frac{\partial^2 E(\mathbf{R})}{\partial \mathbf{R}_I \partial \mathbf{R}_J} - \omega^2 \right| = 0. \tag{2.6}$$

The calculation of the equilibrium geometry and of the vibrational properties of a system thus amounts to computing the first and second derivatives of its Born Oppenheimer energy surface. The basic tool for accomplishing this goal is the Hellmann-Feynman theorem (Hellmann 1937; Feynman 1939), which states that the first derivative of the eigenvalues of a Hamiltonian, H_λ, that depends on a parameter λ is given by the expectation value of the derivative of the Hamiltonian:

$$\frac{\partial E_\lambda}{\partial \lambda} = \left\langle \Psi_\lambda \left| \frac{\partial H_\lambda}{\partial \lambda} \right| \Psi_\lambda \right\rangle, \tag{2.7}$$

where Ψ_λ is the eigenfunction of H_λ corresponding to the E_λ eigenvalues: $H_\lambda \Psi_\lambda = E_\lambda \Psi_\lambda$. In the Born-Oppenheimer approximation, nuclear coordinates act as parameters in the electronic Hamiltonian, Eq. (2.3). The force acting on the Ith nucleus in the electronic ground state is thus.

$$F_I = -\frac{\partial E(\mathbf{R})}{\partial \mathbf{R}_I} = -\left\langle \Psi \left| \frac{\partial H_{BO}(\mathbf{R})}{\partial \mathbf{R}_I} \right| \Psi \right\rangle, \tag{2.8}$$

where $\Psi(\mathbf{r}, \mathbf{R})$ is the electronic ground-state wave function of the Born-Oppenheimer Hamiltonian. This Hamiltonian depends on $\mathbf{R}$ via the electronic-ion interaction that couples to the electronic degrees of freedom only through the electron charge density. The Hellmann-Feynman theorem states in this case that

$$\mathbf{F}_I = -\int n_{\mathbf{R}}(\mathbf{r})\frac{\partial V_{\mathbf{R}}(\mathbf{r})}{\partial \mathbf{R}_I}d\mathbf{r} - \frac{\partial E_N(\mathbf{r})}{\partial \mathbf{R}_I}, \qquad (2.9)$$

where $V_{\mathbf{R}}(\mathbf{r})$ is the electron-nucleus interaction,

$$V_{\mathbf{R}}(\mathbf{r}) = -\sum_{iI}\frac{Z_I e^2}{|\mathbf{r}_i - \mathbf{R}_I|}, \qquad (2.10)$$

and $n_{\mathbf{R}}(\mathbf{r})$ is the ground-state electron charge density corresponding to the nuclear configuration $\mathbf{R}$. The Hessian of the Born-Oppenheimer energy surface appearing in Eq. (2.6) is obtained by differentiating the Hellmann-Feynman forces with respect to nuclear coordinates,

$$\frac{\partial^2 E(\mathbf{R})}{\partial \mathbf{R}_I \partial \mathbf{R}_J} = -\frac{\partial \mathbf{F}_I}{\partial \mathbf{F}_J}. \qquad (2.11)$$

This equation states that the calculation of the Hessian of the Born-Oppenheimer energy surfaces requires the calculation of the ground-state electron charge density $n_{\mathbf{R}}(\mathbf{r})$ as well as of its *linear response* to a distortion of the nuclear geometry, $\partial n_{\mathbf{R}}(\mathbf{r})/\partial \mathbf{R}_I$. This fundamental result was first stated in the late 1960s by De Cicco and Johnson (1969) and by Pick, Cohen, and Martin (1970). The Hessian matrix is usually called the matrix of the *interatomic force constants*.

2.1.2   The Bloch's theorem

Because the ions in a perfect crystal are arranged in a regular periodic array, we are led to consider the problem of an electron in a potential $U(\mathbf{r})$ with the periodicity of the underlying Bravais lattice, i.e.,

$$U(\mathbf{r} + \mathbf{R}) = U(\mathbf{r}), \qquad (2.12)$$

for all Bravais lattice vectors $\mathbf{R}$. Since the scale of periodicity of the potential $U(\sim 10^{-8}\text{cm})$ is the size of a typical de Broglie wavelength of an electron in the Sommerfeld free electron model, it is essential to use quantum mechanics in accounting for the effect of periodicity on electronic motion. F. Bloch proved that the eigenstates ψ of the one-electron Hamiltonian can be chosen to have the form of a plane wave times a function with the periodicity of the Bravais lattice [1, 6]:

$$\psi_{nk}(\mathbf{r}) = u_{nk}(\mathbf{r})e^{(i\mathbf{k}\cdot\mathbf{r})}, \qquad (2.13)$$

8

where $u_k(\mathbf{r})$ has the period of the crystal lattice,

$$u_{nk}(\mathbf{r}) = u_{nk}(\mathbf{r} + \mathbf{R}), \tag{2.14}$$

for all R in the Bravais lattice. The eigenfunctions of the wave equation for a periodic potential are the product of a plane wave $\exp(i\mathbf{k} \cdot \mathbf{r})$ times a functional $u_k(\mathbf{r})$ with the periodicity of the crystal lattice.

Considering the expression 2.14 for the periodic potential and the equation (2.13), it is easy to show that,

$$\psi_{nk}(\mathbf{r} + \mathbf{R}) = e^{i\mathbf{k}\cdot\mathbf{R}}\psi_{nk}(\mathbf{r}), \tag{2.15}$$

for every R in the Bravais lattice. Bloch's theorem is sometimes stated n this alternative form. The eigenstates of H can be chosen so that associated with each ψ is a wave vector $\mathbf{k}$ such that,

$$\psi(\mathbf{r} + \mathbf{R}) = e^{i\mathbf{k}\cdot\mathbf{R}}\psi(\mathbf{r}), \tag{2.16}$$

for every $\mathbf{R}$ in the Bravais lattice.

2.2 The Density Functional Theory

2.2.1 Functionals

In this section we start studying the Density Functional Theory in detail. In order to discuss it more carefully it is necessary to introduce a useful mathematical tool, *the functional*. Roughly speaking, a functional $F[f]$ is a mapping of an entire function f onto a value [7].

A functional $F[n]$ can be defined as a rule for going from a function to a number, In other words, a functional takes a function as its arguments or input and returns an scalar, just as a function $y = f(x)$ is a rule (f) for going from a number (x) to a number (y). Its use goes back to the calculus of variations where one searches for a function which minimises a certain functional. A particularly important application in physics is to search for a state of a system which minimises the energy functional. A simple example of a functional is the particle number, which is a rule for obtaining the number N, given the function $n(\mathbf{r})$ [8, 9],

$$N = \int d^3 r\, n(\mathbf{r}) = N[n], \tag{2.17}$$

the name given to the argument of n is completely irrelevant, since the functional depends on the *function* itself, not on its variable. Hence we do not need to distinguish $F[n(\mathbf{r})]$ from, e.g., $F[n(\mathbf{r}')]$. Another important case is that in which the functional depends on a parameter,

$$V_H[n(\mathbf{r})] = q^2 \int d^3r' \frac{n(\mathbf{r};)}{|\mathbf{r} - \mathbf{r}'|}, \qquad (2.18)$$

which is a rule that for any value of the parameter $\mathbf{r}$ associates a value $V_H[n(\mathbf{r})]$ with the function $n(\mathbf{r}')$. This term is the so called Hartree potential, which we will repeatedly encounter below.

2.2.1.1   Functional variation

Following the previous example of a function of one variable, $y = f(x)$, one can think of two types of variations of y, the first coming from variations of x and the second from variations of f. The variation study in ordinary calculus shows that for a fixed functional dependence $f(x)$, the ordinary differential dy measures how y changes as a result of a variation $x \rightarrow x + dx$ of the variable x. On the other hand, the variation studied in variational calculus shows that for a fixed point x, the functional variation δy measures how the value y at this point changes as a result of a variation in the functional form $f(x)$.

2.2.1.2   Functional derivative

The differential of a functional is the part of the difference $F[f + \delta f] - F[f]$ that depends on δf linearly. Each $\delta f(x)$ may contribute to this difference. For very small δf,

$$\delta F = \int \frac{\delta F}{\delta f(x)} \delta f(x) dx, \qquad (2.19)$$

where the quantity $\delta F/\delta f(x)$ is the first-order functional derivative of F with respect to f at the point x. The integral arises because the variation in the functional F is determined by variations in the function at all points in space. This equation is the rule for operating on $\delta f(x)$ to give a number δF, and is the extension to continuous variables of the formula for the total differential of a function $F(f_1, f_2, ...)$: $dF = \sum_i (\partial F/\partial f_i) df_i$.

The following general formula covers many cases of interest. Consider the functional,

$$F[n] = \int f(x; n, n^{(1)}, n^{(2)}, ..., n^{(n)}) dx, \qquad (2.20)$$

where $n^{(i)}(x) = d^{(i)} n(x)/dx^i$, n vanishes at the boundary of x. Then a general expression $\delta F[n]/\delta n(x)$ for obtaining functional derivatives with respect to $n(x)$ is given by,

$$\frac{\delta F[n]}{\delta n(x)} = \frac{\partial f}{\partial n} - \frac{d}{dx} \frac{\partial f}{\partial n^{(1)}} + \frac{d^2}{dx^2} \frac{\partial f}{\partial n^{(2)}} - \frac{d^3}{dx^3} \frac{\partial f}{\partial n^{(3)}}. \qquad (2.21)$$

This expression is frequently used in DFT to obtain XC potentials from XC energies.

2.2.2   An introduction to DFT

In order to introduce the Density Functional Theory (DFT) we start with a short introduction to the classical quantum mechanics. In this context the time independent non-relativistic Schrödinger equation [2] is written as,

$$\hat{H}\Psi_i(\mathbf{r}_1, \mathbf{r}_2, \cdots, \mathbf{r}_N, \mathbf{R}_1, \mathbf{R}_2, \cdots, \mathbf{R}_M) = E\Psi_i(\mathbf{r}_1, \mathbf{r}_2, \cdots, \mathbf{r}_N, \mathbf{R}_1, \mathbf{R}_2, \cdots, \mathbf{R}_M) \qquad (2.22)$$

where $\hat{H}$ is the Hamiltonian operator representing the total energy for a molecular system consisting of M nuclei and N electrons in the absence of magnetic or electric fields. The Hamiltonian $\hat{H}$ describing a perfect crystal can be written as,

$$\hat{H} = \sum_{i=1}^{N} \frac{p_i^2}{2m_i} + \sum_{I=1}^{M} \frac{P_I^2}{2M_I} + \frac{1}{2} \sum_{I \neq J}^{M} \frac{Z_I Z_J e^2}{|\mathbf{R}_I - \mathbf{R}_J|}$$
$$- \sum_{i,I=1}^{NM} \frac{Z_I e^2}{|\mathbf{r}_i - \mathbf{R}_I|} + \frac{1}{2} \sum_{i \neq j}^{N} \frac{e^2}{|\mathbf{r}_i - \mathbf{r}_j|}, \qquad (2.23)$$

here, A and B run over the M nuclei while i and j denote the N electrons in the system. The first two terms describe the kinetic energy of the electrons and the nuclei respectively. The remaining three terms define the potential part of the Hamiltonian and represent the attractive electrostatic interaction between the nuclei and the electrons and the repulsive potential due to the electron-electron

11

and nucleus-nucleus interactions, respectively. Ψ_i stands for the wave function of the i'th state of the system, which depends on the 3N spatial coordinates, the N spin coordinates of the electrons, and the 3M spatial coordinates of the nuclei. The wave function Ψ_i contains all information that can possibly be known about the quantum system at hand. Finally, E_i is the numerical value of the energy of the state described by Ψ_i.

Taking advantage of the *adiabatic approximation* (see section 2.1.1), it is possible to write the Schrödinger equation for N interacting electrons under an external potential (usually the Coulomb potential of the nuclei) as,

$$\left[-\frac{\hbar^2}{2m} \sum_i^N \nabla_i^2 + \sum_i^N V_{ext}(\mathbf{r}_i) + \frac{1}{2} \sum_{i \neq j} \frac{e^2}{|\mathbf{r}_i - \mathbf{r}_j|} \right] \Psi(\mathbf{r}_1, \mathbf{r}_2, \cdots, \mathbf{r}_N)$$
$$= E\Psi(\mathbf{r}_1, \mathbf{r}_2, \cdots, \mathbf{r}_N). \tag{2.24}$$

To solve this equation is not easy even from the computational point of view. A simple estimate of the computational complexity of this task is to imagine a real-space representation of Ψ on a mesh, in which each coordinate is discretized by using 20 mesh points (which is not very much). For N electrons, Ψ becomes a function of $3N$ coordinates (ignoring spin, and taking Ψ to be real), and 20^{3N} values are required to describe Ψ on the mesh. The density $n(\mathbf{r})$ is a function of three coordinates, and requires 20^3 values on the same mesh. The Kohn-Sham formulation of DFT additionally employ sets of single-particle orbitals. N such orbitals, used to build the density, require $20^3\ N$ values on the same mesh. For $N = 10$ electrons, the many-body wave function thus requires $2030/203 \approx 1035$ times more storage space than the density, and $2030/(10 \times 203) \approx 1034$ times more than sets of single-particle orbitals. Clever use of symmetries can reduce these ratios, but the full many-body wave function remains unaccessible for real systems with more than a few electrons [9].

2.2.3 Fundamentals of Density Functional Theory

Density Functional Theory (DFT) has proved to be highly successful in describing structural and electronic properties in vast class of materials. Furthermore DFT is computationally very simple. For these reasons DFT has become a common tool in *first-principles* calculations aimed at describing - or even predicting - properties of molecular and condensed matter systems.

There exist two fundamental of DFT. The first is that [10], *any* property of a system of many interacting particles can be viewed as a *functional* of the

ground state density $n_0(\mathbf{r})$; that is, one scalar function of position $n_0(\mathbf{r})$, in principle, determines all the information in the many-body wavefunction for the ground state and all excited states. The second is that [11], the original many-body problem can be replaced by an auxiliary independent particle problem. In principle, it leads to exact calculations of properties of many-body systems using independent-particle methods. This approach involves *independent particles* but and *interacting density* [7].

2.2.4 The Hohenberg-Kohn theorem

According to the Hohenberg-Kohn theorem, no two different potentials acting on the electrons of a given system can give rise to a same ground-state electronic charge density [10].

Let us consider a system of N interacting (spinless) electrons under an external potential $V_{ext}(\mathbf{r})$ (usually the Coulomb potential of the nuclei as mentioned in a previous section). If the system has a nondegenerate ground state, it is obvious that there is only one ground-state charge density $n(\mathbf{r})$ that correspond to a given $V_{ext}(\mathbf{r})$. Far less obvious result is that in 1964 Hohenberg and Kohn [10] demonstrated the opposite; there is only one external potential $V_{ext}(\mathbf{r})$ that yields a given ground-state charge density $n(\mathbf{r})$. The demonstration is very simple and uses a *reductio ad absurdum* argument [12].

Let us consider a many-electron Hamiltonian $H = T + U + V_{ext}$, with ground state wavefunction Ψ. T is the kinetic energy, U the electron-electron interaction, and V_{ext} the external potential. The charge density $n(\mathbf{r})$, which plays a central role in electronic structure theory, is given by the expectation value of the density operator $\hat{n}(\mathbf{r}) = \sum_{i=1,N} \delta(\mathbf{r} - \mathbf{r}_i)$,

$$n(\mathbf{r}) = \frac{\langle \Psi | \hat{n}(\mathbf{r}) | \Psi \rangle}{\langle \Psi | \Psi \rangle} = N \int |\Psi(\mathbf{r}, \mathbf{r}_2, \mathbf{r}_3, \ldots, \mathbf{r}_N)|^2 d_2 \ldots d\mathbf{r}_N, \qquad (2.25)$$

that obeying the orthonormality constraint,

$$\langle \Psi | \Psi \rangle = 1. \qquad (2.26)$$

Let us consider now a *different* Hamiltonian $H' = T + U + V'_{ext}$ (V_{ext} and V'_{ext} do not differ simply by a constant: $V_{ext} - V'_{ext} \neq$ const.) with ground state wavefunction Ψ'. Let us assume that the ground state charge densities are the same: $n[V_{ext}] = n[V'_{ext}]$. The following inequality holds:

$$E' = \langle \Psi'|H'|\Psi' \rangle < \langle \Psi|H'|\Psi \rangle = \langle \Psi|H + V'_{ext} - V_{ext}|\Psi \rangle, \qquad (2.27)$$

that is,

$$E' < E + \int (V_{ext}(\mathbf{r}) - V'_{ext}(\mathbf{r}))n(\mathbf{r})d\mathbf{r}. \qquad (2.28)$$

The inequality is strict because Ψ and Ψ' are different, being eigenstates of different Hamiltonians. By reversing the primed and unprimed quantities, one obtains an absurd result. This demonstrates that no two different potentials can have the same charge density. The density uniquely determines the external potential to within a constant. Therefore all properties of the system are completely determined given only the ground state density $n_0(\mathbf{r})$.

A straightforward consequence of the first Hohenberg and Kohn theorem is that the ground state energy E is a *functional* $E[n(\mathbf{r})]$ of $n(\mathbf{r})$. We can write,

$$\begin{aligned} E[n(\mathbf{r})] &= \langle \Psi|T + U + V_{ext}|\Psi \rangle = \langle \Psi|T + U|\Psi \rangle + \langle \Psi|V_{ext}|\Psi \rangle \\ &= F[n(\mathbf{r})] + \int n(\mathbf{r})V_{ext}(\mathbf{r})d\mathbf{r}, \qquad (2.29) \end{aligned}$$

where $F[n(\mathbf{r})]$ is a *universal* functional of the charge density $n(\mathbf{r})$ (and *not* of $V_{ext}(\mathbf{r})$). By *universal* it is meant here that the functional is independent of the external potential acting on the electrons, though it obviously depends on the form of the electron-electron interaction. For this functional, $E[n(\mathbf{r})]$, a variational principle holds: the ground-state energy corresponding to the external potential $V_{ext}(r)$ is *minimised* by the ground-state electron charge density under the constraint that the integral of $n(r)$ equals the total number of electrons. The reason why this is possible is that the density and the potential are conjugate variables, which means that the contribution of the external potential to the total energy occurs only via an integral of the potential times the density.

In this way, DFT exactly reduces the N-body problem to the determination of a 3-dimensional function $n(\mathbf{r})$ which minimises a functional $E[n(\mathbf{r})]$. Furthermore, the value of the minimum coincides with the ground-state energy, i.e., the functional $E[n(\mathbf{r})]$ alone is sufficient to determine the exact ground-state energy and density. Unfortunately this is of little use as $F[n(\mathbf{r})]$ is not known. That problem can be handled by mapping the system onto an auxiliary system of noninteracting electrons (see section 2.2.5). An schematic representation for the relation established by Hohenberg and Kohn is illustrated in Fig. 2.1.

$$
\begin{array}{ccc}
V_{ext}(\mathbf{r}) & \overset{\text{HK}}{\Longleftarrow} & n_0(\mathbf{r}) \\
\Downarrow & & \Uparrow \\
\Psi_i(\{\mathbf{r}\}) & \Rightarrow & \Psi_0(\{\mathbf{r}\})
\end{array}
$$
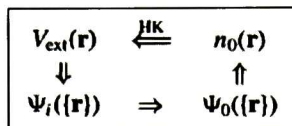
Figure 2.1: Schematic representation of Hohenberg-Kohn theorem. The smaller arrows denote the usual solution of the Schrödinger equation where the potential $V_{ext}(\mathbf{r})$ determines all states of the system $\Psi_i(\mathbf{r})$, including the ground state $\Psi_0(\mathbf{r})$ and ground state density $n_0(\mathbf{r})$. The long arrow labeled "HK" denotes the Hohenberg-Kohn theorem, which completes the circle (Figure taken from [7]).

2.2.5   The Kohn-Sham scheme

2.2.5.1   Practical implementation of DFT

In 1965 Kohn and Sham [11] replaced the original many-body problem by an auxiliary independent particle problem. The Kohn-Sham equations represent a mapping of the interacting many-electron system onto a system of noninteracting electrons moving in an effective potential due to all the other electrons [13].

Practical implementations of DFT require an explicit construction of the Hohenberg-Kohn free-energy functional, $F[n] = F_{HK}[n]$, given above. It is customary to write $F_{HK}[n]$ for interacting electrons as a sum of the noninteracting kinetic energy, $T_s[n]$, and two interaction terms, the electrostatic energy and the exchange-correlation energy [12]:

$$
F_{HK}[n(\mathbf{r})] = T_s[n(\mathbf{r})] + E_H[n(\mathbf{r})] + E_{XC}[n(\mathbf{r})], \tag{2.30}
$$

where the last term, $E_{XC}[n]$, is defined as the remainder and thus contains everything that is not included in the first two terms. Each of the three terms on the right hand side is in principle a functional of the independent variable $n(\mathbf{r})$. Only the second term, the electrostatic energy also known as the Hartree energy, is easily expressed explicitly:

$$
E_H[n(\mathbf{r})] = \frac{e^2}{2} \int \frac{n(\mathbf{r})n(\mathbf{r}')}{|\mathbf{r} - \mathbf{r}'|} . d\mathbf{r} d\mathbf{r}' \tag{2.31}
$$

The first and last terms are much more complicated: knowledge of the former implies a full understanding of the quantum mechanical noninteracting

15

problem; the latter contains all of the manybody physics, and is in principle even more complex.

For a system of non-interacting electrons the ground-state charge density is representable as a sum over one-electron orbitals (the Kohn-Sham (KS) orbitals) $\psi_i(\mathbf{r})$. The associated electronic one-body density or charge density,

$$n(\mathbf{r}) = \sum_i^{occ} f_i |\psi_i(\mathbf{r})|^2, \qquad (2.32)$$

is obtained from a single Slater determinant built from the occupied orbitals, where f_i are integer occupation numbers. The KS orbitals are the solutions of the Schrödinger equation,

$$\left(-\frac{\hbar^2}{2m} \nabla^2 + V_{KS}(\mathbf{r}) \right) \psi_i(\mathbf{r}) = \varepsilon_i \psi_i(\mathbf{r}), \qquad (2.33)$$

obeying the orthonormality constraints,

$$\int \psi_i^*(\mathbf{r}) \psi_j(\mathbf{r}) \, d\mathbf{r} = \delta_{ij}. \qquad (2.34)$$

The existence of a unique potential $V_{KS}(\mathbf{r})$ having $n(\mathbf{r})$ as its ground state charge density is a consequence of the Hohenberg and Kohn theorem, which holds irrespective of the form of the electron-electron interaction U.

2.2.5.2 The Kohn-Sham equations from variational principle

As a self-consistent method, the Kohn-Sham approach involves *independent particles* but an *interacting density*, in such a way that now the problem is to determine $V_{KS}(\mathbf{r})$ for a given $n(\mathbf{r})$. The set of wave functions ψ_i are given by the self-consistent solutions to the Kohn-Sham equations. In order to do it, it is necessary to determine the set of wave functions ψ_i that minimise the Kohn-Sham energy functional. This problem is solved by considering the variational property of the energy but considering the orthonormality constraints given in Eq. (2.34) [12, 14],

$$E' = E - \sum_{ij} \lambda_{ij} \left(\int \psi_i^*(\mathbf{r}) \psi_j^*(\mathbf{r}) \, d\mathbf{r} - \delta_{ij} \right), \qquad (2.35)$$

where λ_{ij} are Lagrange multipliers, must vanish,

$$\frac{\delta E'}{\delta \psi_i^*(\mathbf{r})} = \frac{\delta E'}{\delta \psi_i(\mathbf{r})} = 0. \qquad (2.36)$$

It is convenient to rewrite the energy functional as follows,

$$E = T_s[n(\mathbf{r})] + E_H[n(\mathbf{r})] + E_{XC}[n(\mathbf{r})] + \int n(\mathbf{r})V_{ext}(\mathbf{r})d\mathbf{r}. \qquad (2.37)$$

The first term is the kinetic energy of *non-interacting* electrons,

$$T_s[n(\mathbf{r})] = -\frac{\hbar^2}{2m}2\sum_i \int \psi_i^*(\mathbf{r})\nabla^2\psi_i(\mathbf{r})d\mathbf{r}, \qquad (2.38)$$

the second term, called the Hartree energy, contains the electrostatic interactions between clouds of charge,

$$E_H[n(\mathbf{r})] = \frac{e^2}{2}\int \frac{n(\mathbf{r})n(\mathbf{r})'}{|\mathbf{r}-\mathbf{r}'|}d\mathbf{r}d\mathbf{r}', \qquad (2.39)$$

the third term, called the *exchange-correlation energy*, contains all the remaining terms: our ignorance is hidden there. The logic behind such procedure is to subtract out easily computable terms which account for a large fraction of the total energy.

Using,

$$\frac{\delta n(\mathbf{r})}{\delta\psi_i^*(\mathbf{r}')} = \psi_i(\mathbf{r})\delta(\mathbf{r}-\mathbf{r}'), \qquad (2.40)$$

and the formulae given in section 2.2.1, one finds,

$$\frac{\delta T_s}{\delta\psi_i^*(\mathbf{r})} = -\frac{\hbar^2}{2m}2\sum_i \nabla^2\psi_i(\mathbf{r}), \qquad (2.41)$$

$$\frac{\delta E_H}{\delta\psi_i^*(\mathbf{r})} = e^2\int \frac{n(\mathbf{r}')}{|\mathbf{r}-\mathbf{r}'|}d\mathbf{r}'\psi_i(\mathbf{r}), \qquad (2.42)$$

and finally,

$$\left[-\frac{\hbar^2}{2m}\nabla^2 + V_H(\mathbf{r}) + V_{XC}([n(\mathbf{r})]) + V_{ext}(\mathbf{r})\right]\psi_i(\mathbf{r}) = \sum_j \lambda_{ij}\psi_j(\mathbf{r}), \quad (2.43)$$

where ψ_i is the wave function of electronic state i, and V_H is the Hartree potential of the electrons given by,

$$V_H(r) = e^2 \int \frac{n(\mathbf{r}')}{|\mathbf{r} - \mathbf{r}'|} d^3\mathbf{r}', \qquad (2.44)$$

the exchange-correlation potential, V_{XC}, is given formally by the functional derivative,

$$V_{XC}[n(\mathbf{r})] = \frac{\partial E_{XC}[n(\mathbf{r})]}{\partial n(\mathbf{r})} \qquad (2.45)$$

The Lagrange multiplier λ_{ij} are obtained by multiplying both sides of Eq. (2.43) by $\psi_k^*(\mathbf{r})$ and integrating,

$$\lambda_{ik} = \int \psi_k^*(\mathbf{r}) \left(-\frac{\hbar^2}{2m}\nabla^2 + V_H(\mathbf{r}) + V_{XC}[n(\mathbf{r})] + V_{ext}(\mathbf{r}) \right) \psi_i(\mathbf{r})d\mathbf{r}. \qquad (2.46)$$

For an insulator, whose states are either fully occupied or completely empty, it is always possible to make a subspace rotation in the space of ψ's (leaving the charge density invariant). We finally get the KS equations,

$$(H_{KS} - \varepsilon_i)\psi_i(\mathbf{r}) = 0, \qquad (2.47)$$

where $\lambda ij = \delta_{ij}\varepsilon_j$ and the operator H_{KS}, called KS Hamiltonian, is defined as,

$$H_{KS} = -\frac{\hbar^2}{2m}\nabla^2 + V_H(\mathbf{r}) + V_{XC}(\mathbf{r}) + V_{ext}(\mathbf{r}) = -\frac{\hbar^2}{2m}\nabla^2 + V_{KS}(\mathbf{r}), \qquad (2.48)$$

with,

$$V_{KS}(\mathbf{r}) = V_H(\mathbf{r}) + V_{XC}(\mathbf{r}) + V_{ext}(\mathbf{r}). \qquad (2.49)$$

Equation (2.48) is related to the functional derivative of the energy:

$$\frac{\delta E}{\delta\psi_i^*(\mathbf{r})} = H_{KS}\psi_i(\mathbf{r}). \qquad (2.50)$$

Finally, Eq. (2.47) can be written as a Schrödinger equation for this auxiliary (independent particle) system as,

$$\left[-\frac{\hbar^2}{2m}\nabla^2 + V_{KS}(\mathbf{r}) \right] \psi_i(\mathbf{r}) = \varepsilon_i\psi_i(\mathbf{r}), \qquad (2.51)$$

where $V_{KS}(\mathbf{r})$ is given in Eq. (2.52).

2.2.5.3   Self consistency cycle

Since both V_H and V_{XC} depend on $n(\mathbf{r})$, which depends on the ψ_i, which in turn depend on V_{KS} , the problem of solving the KS equations is a nonlinear one. The usual way of solving such problems is to start with an initial guess for $n(\mathbf{r})$, calculate the corresponding $V_{KS}(\mathbf{r})$,

$$V_{KS}(\mathbf{r}) = V_H(\mathbf{r}) + V_{XC}(\mathbf{r}) + V_{ext}(\mathbf{r}), \qquad (2.52)$$

and then solve the differential equation,

$$\left[-\frac{\hbar^2}{2m}\nabla^2 + V_{KS}(\mathbf{r}) \right] \psi_i(\mathbf{r}) = \varepsilon_i \psi_i(\mathbf{r}), \qquad (2.53)$$

for the ψ_i. From these equation one calculates a new density using,

$$n(\mathbf{r}) \equiv n_s(\mathbf{r}) = \sum_i^{occ} f_i \mid \psi_i(\mathbf{r}) \mid^2, \qquad (2.54)$$

and starts again. The process is repeated until it converges. The technical name for this procedure is *self-consistency cycle*. Different convergence criteria (such as convergence in the energy, the density, or some observable calculated from these) and various convergence accelerating algorithms (such as mixing of old and new effective potentials) are in common use [15]. The most popular are the conjugate gradient and those of Pulay [16] and Broyden [17].

    Once one has a converged solution $n_0(\mathbf{r})$, one can calculate the total energy. In particular we used the Pulay mixing of the potential based on the seven-Pulay previous iterations [16].

2.2.6   Exchange-Correlation Functional

The most difficult problem in any electronic structure calculation is posed by the need to take account of the effects of the electron-electron interaction. Electrons repel reach other due to the Coulomb interaction between their charges. The Coulomb energy of a system of electrons can be reduced by keeping the electrons spatially separated, but this has to balanced against the kinetic energy cost of deforming the electronic wave functions in order to separate the electrons. The effects of the electron-electron interaction are briefly described below.

The exchange-correlation functional is often decomposed as $E_{XC} = E_X + E_C$, where E_X is due to the Pauli principle (exchange energy) and E_C is due to correlations.

2.2.6.1 Exchange

The wave function of a many-electron system must be antisymmetric under exchange f any two electrons because the electrons are fermions. The antisymmetry of the wave function produces a spatial separation between electrons that have the same spin and thus reduces the Coulomb energy of the electronic system. The reduction in the energy of the electronic system due to the antisymmetry of the wave function is called the exchange energy. It is straightforward to include exchange in a total energy calculation, and this is generally referred to as the Hartree-Fock approximation [9].

The exchange energy can be written explicitly in terms of the single-particle orbitals as,

$$E_X[\psi_i[n]] = -\frac{e^2}{2} \sum_{jk} \int \frac{\psi_j^*(\mathbf{r})\psi_k^*(\mathbf{r}')\psi_j^*(\mathbf{r}')\psi_k^*(\mathbf{r})}{|\mathbf{r} - \mathbf{r}'|} \, d\mathbf{r} \, d\mathbf{r}', \qquad (2.55)$$

which is known as the Fock term, but no general exact expression in terms of the density is known.

2.2.6.2 Correlation

For the correlation energy no general explicit expression is known, neither in terms of orbitals nor densities. Different ways to understand correlations are described below [9].

Correlation energy: variational approach. A simple way to understand the origin of correlation is to recall that the Hartree energy is obtained in a variational calculation in which the many-body wave function is approximated as a product of single-particle orbitals. Use of an antisymmetrized product (a Slater determinant) produces the Hartree and the exchange energy. The correlation energy is then defined as the difference between the full ground-state energy (obtained with the correct many-body wave function) and the one obtained from the (Hartree-Fock or Kohn-Sham) Slater determinant. Since it arises from a more general trial wave function than a single Slater determinant, correlation cannot raise the total energy, and $E_C[n] \leq 0$. Since a Slater determinant is itself

20

more general than a simple product we also have $E_X \leq 0$, and thus the upper bound $E_X C[n] \leq 0$.

Correlation energy: probabilistic approach. Recalling the quantum mechanical interpretation of the wave function as a probability amplitude, we see that a product form of the many-body wave function corresponds to treating the probability amplitude of the many-electron system as a product of the probability amplitudes of individual electrons (the orbitals). Mathematically, the probability of a composed event is only equal to the probability of the individual events if the individual events are independent (i.e., uncorrelated). Physically, this means that the electrons described by the product wave function are independent. Such wave functions thus neglect the fact that, as a consequence of the Coulomb interaction, the electrons try to avoid each other.

The fact that both exchange and correlation tend to keep electrons apart has given rise to the terminology of electron holes, describing the region of reduced probability for encountering a second electron around a given reference electron. Unfortunately we shall not discuss this topic here.

2.2.7 The Local Density Approximation

As was mentioned in section 2.2.5 it is necessary to approximate the E_{XC} energy in order to solve self consistency the Kohn-Sham equations.

In the Local Density Approximation (LDA) the exchange-correlation energy of an electronic system is constructed by assuming that the exchange-correlation energy per electron at a point $\mathbf{r}$ in the electron gas, $\varepsilon_{XC}(\mathbf{r})$, is equal to the exchange-correlation energy per electron in a homogeneous electron gas that has the same density as the electron gas at point $\mathbf{r}$. Thus,

$$E_{XC}[n(\mathbf{r})] = \int \varepsilon_{XC}(\mathbf{r})n(\mathbf{r})d^3\mathbf{r}, \qquad (2.56)$$

and,

$$\frac{\delta E_{XC}[n(\mathbf{r})]}{\delta n(\mathbf{r})} = \frac{\partial [n(\mathbf{r})\varepsilon_{XC}^{hom}[n(\mathbf{r})]]}{\partial n(\mathbf{r})} = \left(\varepsilon_{XC}^{hom} + n(\mathbf{r})\frac{d\varepsilon_{XC}^{hom}}{dn(\mathbf{r})} \right). \qquad (2.57)$$

The LDA approximation assumes that the exchange-correlation energy functional is purely local. In the research work done for this thesis we also tested the generalized gradient approximation (see subsection 2.2.8) and we did not find any improvement in our results, that is the reason why we only will mention the

LDA in next chapters. At this point it is also important to mention that even in such simple case the exact form of ε_{XC} is unknown, for that reason we used the *local density approximation* as parameterised by Perdew and Zunger [18].

Structural and vibrational properties of solids are in general accurately described. The correct crystal structure is usually found to have the lowest energy, bond length, bulk moduli, phonon frequencies are accurate within a few percent. We shall show that we got errors $\sim 1\%$, with respect to experimental results, for lattice constants and frequencies.

2.2.8 The Generalized Gradient Approximation

It is well know that LDA fails in situations where the density undergoes rapid changes such as in molecules. Nowadays there exist many other approximations for the E_{XC} that are able to consider this nonuniform charge densities. One of these is the *Generalized Gradient Approximation* (GGA). In this approximation a gradient of the density at the point where we want to calculate E_{XC} is included. This still results in a local expression for E_{XC}, and gives the various gradient-corrected functionals. Symbolically this can be written as,

$$E_{XC} = E_{XC}[n(\mathbf{r}), \nabla n(\mathbf{r})].\qquad(2.58)$$

Some good reviews can be found in the literature about this approximation [19–22].

2.2.9 Plane waves basis set

Due to Bloch's theorem *plane waves* (PWs) are the natural choice for the representation of electron orbitals in a periodic system like crystals.

The eigenstates of any independent particle Schrodinger-like equation in which each electron moves in an effective potential (also called V_{KS}), such as the Kohn-Sham equations, satisfy the eigenvalue equation given by Eq. (2.53),

$$\left[-\frac{\hbar^2}{2m}\nabla^2 + V_{KS}(\mathbf{r})\right]\psi_i(\mathbf{r}) = \varepsilon_i\psi_i(\mathbf{r}),\qquad(2.59)$$

In a solid it is convenient to require the states to be normalized and obey periodic boundary conditions in a large volume Ω that is allowed to go to infinity. Using the fact that any periodic function can be expanded in the complete set of Fourier components, an eigenfunction $\psi_i(\mathbf{r})$ can be written as [7],

$$\psi_i(\mathbf{r}) = \sum_{\mathbf{q}} c_{i,\mathbf{q}} \times \frac{1}{\sqrt{\Omega}} e^{i\mathbf{q}\cdot\mathbf{r}} \equiv \sum_{\mathbf{q}} c_{i,\mathbf{q}} \times |\mathbf{q}\rangle, \qquad (2.60)$$

where $c_{i,\mathbf{q}}$ are the expansion coefficients of the wavefunction in the basis of orthonormal PWs $|\mathbf{q}\rangle$ satisfying,

$$\langle \mathbf{q}'|\mathbf{q}\rangle \equiv \frac{1}{\Omega} \int_{\Omega} e^{-i\mathbf{q}'\cdot\mathbf{r}} e^{i\mathbf{q}\cdot\mathbf{r}} = \delta_{\mathbf{q},\mathbf{q}'} \qquad (2.61)$$

Combining the three last equations leads to the Schrödinger equation in the Fourier space,

$$\sum_{\mathbf{q}} \langle \mathbf{q}'|H_{KS}|\mathbf{q}\rangle c_{i,\mathbf{q}} = \varepsilon_i \sum_{\mathbf{q}} \langle \mathbf{q}'|\mathbf{q}\rangle c_{i,\mathbf{q}} = \varepsilon_i c_{i,\mathbf{q}'} \qquad (2.62)$$

Finally the independent-particle Schrödinger equation for any given $\mathbf{k}$ can be written as the matrix equation,

$$\sum_{m'} H_{m,m'}(\mathbf{k}) c_{i,m'}(\mathbf{k}) = \varepsilon_i(\mathbf{k}) c_{i,m}(\mathbf{k}), \qquad (2.63)$$

were we define $\mathbf{q} = \mathbf{k} + \mathbf{G}_m$ and $\mathbf{q}' = \mathbf{k} + \mathbf{G}'_m$,

$$H_{m,m'}(\mathbf{k}) = \langle \mathbf{k} + \mathbf{G}_m | H_{KS} | \mathbf{k} + \mathbf{G}_{m'} \rangle = \frac{\hbar^2}{2m_e} |\mathbf{k} + \mathbf{G}|^2 \delta_{m,m'} + V_{KS}(\mathbf{Q}_m - \mathbf{Q}_{m'}), \qquad (2.64)$$

where $\mathbf{G}_m$ are the reciprocal lattice vectors. The eigenvalues and eigenfunctions are labeled as $i = 1, 2, \ldots$ for the discrete set of solutions of the matrix equations for a given $\mathbf{k}$. Equations 2.63 and 2.64 are the basic Schrodinger equations in a periodic crystal.

In the following we will assume that our system is a crystal with lattice vectors $\mathbf{R}$ and reciprocal lattice vectors $\mathbf{G}$. It is not relevant whether the cell is a real unit cell of a real periodic crystal or if it is a super cell describing an aperiodic system. The KS wavefunctions are classified by a band index and a Bloch vector $\mathbf{k}$ in the Brillouin Zone (BZ).

As we showed, the plane wave basis set can be defined as,

$$\langle \mathbf{r}|\mathbf{k}+\mathbf{G}\rangle = \frac{1}{\Omega} e^{i(\mathbf{k}+\mathbf{G})\cdot\mathbf{r}} \quad \text{with} \quad \frac{\hbar^2}{2m}|\mathbf{k}+\mathbf{G}|^2 \leq E_{cut}, \qquad (2.65)$$

where E_{cut} is a cutoff on the kinetic energy of PWs (from now on, simply "the cutoff"). PWs have many attractive features: they are simple to use (matrix elements of the Hamiltonian have a very simple form), orthonormal by construction, unbiased (there is no freedom in choosing PWs: the basis is fixed by the crystal structure and by the cutoff) and it is very simple to check for convergence (by increasing the cutoff) [12].

Unfortunately the extended character of PWs makes it very difficult to accurately reproduce localised functions such as the charge density around a nucleus or even worse, the orthogonalisation wiggles of inner (core) states. In order to describe features which vary on a length scale δ, one needs Fourier components up to $\mathbf{q} \sim 2\pi/\delta$. In a solid, this means $4\pi(2\pi/\delta)^3/3\Omega$ PWs (where Ω is the dimension of the BZ). A simple estimate for diamond is instructive. The $1s$ wavefunction of the carbon atom has its maximum around 0.3 a.u., so $\delta \simeq 0.1$ a.u. is a reasonable value. Diamond has an fcc lattice ($\Omega = (2\pi)^3/(a_0^3/4)$) with lattice parameter $a_0 = 6.74$ a.u., thus yielding $\sim 250,000$ PWs. This is clearly too much for practical use.

In order to decrease to number of plane waves it is necessary to introduce the use of pseudopotentials (see section 2.2.10).

2.2.10 Pseudopotentials

2.2.10.1 An introduction to pseudopotentials

Pseudopotentials were originally introduced to simplify electronic structure calculations by eliminating the need to include atomic core states and the strong potentials responsible for binding them.

The physically reasoning behind the pseudopotential (PP) approximation is simple: since the core-electron wave functions of an atom remain essentially unchanged when placed into different chemical environments and since that the core wave functions only major contribution to chemical bonding is to enforce the valence wave functions orthogonality to the core states, the true atomic potential can justifiably be replaced by a pseudopotential that effectively reproduces the effects of the core electrons [23].

The valence electrons must be constrained to be orthogonal to the core electrons. In the all-electron case this means that the valence wavefunctions have a large number of nodes near the nucleus. One of the reasons we are pseudizing is to make the wavefunction variations smoother, so these must be eliminated. A cut-off radius is chosen, and the pseudopotentials bound states will reproduce the valence wave-functions outside this radius, and be smooth inside [24].

Most pseudopotentials are then constructed such that they satisfy four general conditions. The first is that the valence (the principal quantum number n is further omitted for simplicity) pseudo-wave-functions generated from the pseudopotential should contain no nodes. This stems from the fact that we would like to construct smooth pseudo-wave-functions and therefore the wiggles associated with the nodes are undesirable. Second, the normalised atomic radial pseudo-wave-functions (PP) with angular momentum l is equal to the normalised radial all-electron wave function (AE) beyond a chosen cutoff radius r_{cl},

$$R_l^{PP}(r) = R_l^{AE}(r) \quad \text{for} \quad r > r_{cl}, \tag{2.66}$$

or converges rapidly to that value. Third, the charge enclosed within r_{cl} for the two wave functions must be equal,

$$\int_l^{r_{cl}} \mid R_l^{PP}(r) \mid^2 r^2 dr = \int_l^{r_{cl}} \mid R_l^{AE}(r) \mid^2 r^2 dr. \tag{2.67}$$

Fourth, almost redundantly, the valence all-electron and pseudopotential eigenvalues must be equal,

$$\varepsilon_l^{PP} = \varepsilon_l^{AE} \tag{2.68}$$

2.2.10.2 Norm-Conserving pseudopotentials

Norm-conserving pseudopotentials were first introduced and used by Hamann, Schluter, and Chiang [26]. In their scheme, inside some core radius, the all-electron (AE) wave function is replaced by a soft nodeless pseudo (PS) wave function, with the crucial restriction that the PS wave function must have the same norm as the all-electron wave function within the chosen core radius; outside the core radius the PS and AE wave function are identical. It is now well established that good transferability requires a core radius around the outermost maximum of the AE wave function, because only then the charge distribution and moments of the AE wave functions are well reproduced by the PS wave functions see. Therefore, for elements with strongly localised orbitals like first-row, $3d$, and rare-earth elements the resulting pseudopotentials require a large plane-wave basis set. To work around this, compromises are often made by increasing the core radius significantly beyond the outermost maximum in the AE wave function. But this is usually not a satisfactory solution because the transferability is always adversely affected when the core radius is increased, and

for any new chemical environment, additional tests are required to establish the reliability of such soft PPs [25].

2.2.10.3 Ultrasoft pseudopotentials

An elegant solution to this problem was proposed by Vanderbilt [27]. In his method, the norm-conservation constraint is relaxed and to make up for the resulting charge deficit, localised atom-centred augmentation charges are introduced. These augmentation charges are defined as the charge density difference between the AE and the PS wave function, but for convenience they are pseudized to allow an efficient treatment of the augmentation charges on a regular grid. The core radius of the pseudopotential can now be chosen around half the nearest-neighbour distanceindependent of the position of the maximum of the AE wave function. Only for the augmentation charges a small cutoff radius must be used to restore the moments and the charge distribution of the AE wave function accurately. The pseudized augmentation charges are usually treated on a regular grid in real space, which is not necessarily the same as the one used for the representation of the wave functions [25].

2.2.10.4 Separable pseudopotentials

One major advance was the introduction of a separable form by Kleinmann and Bylander [28], that significantly reduces the computational effort for the calculations of the nonlocal part, expecially when using a plane-wave basis set. A simple way was discovered to put model pseudopotentials,

$$V(\mathbf{r}) = \sum_{lm} | Y_{lm} \rangle V_l(r) \langle Y_{lm} |, \qquad (2.69)$$

into a form which reduces the number of integrals of $V(\mathbf{r})$ required for an energy-band calculation from $mn(n+1)/2$ to mn for each l in the sum. n is the number of plane waves used in the expansion and m the number of points in the Brillouin zone at which the calculation is performed.

2.2.10.5 Relativistic Pseudopotentials

We use the Hartwigsen-Goedecker-Hutter (HGH) pseudopotential which is a relativistic separable dual-space Gaussian PP, specially because it consider relativistic effects relevant for heavier elements and because it is generated on the

basis of a fully relativistic all-electron calculation, i.e., solving the two components Dirac equation [29]. It is important to mention that there exist some other PP like the Troullier-Martins that also consider this relativistic interaction but please read an appropriate review for further details [30].

Here we just shall mention that the inclusion of the spin-orbit interaction in our computational calculations were done through the use of this HGH pseudopotential. A detailed explanation about this pseudopotential will be given in the subsection 2.5.2 devoted to the physical origin of the spin-orbit coupling. In that subsection, the inclusion of the spin-orbit coupling will be explained in detail.

2.3   Density Functional Perturbation Theory

The formalism which calculates the response functions of a DFT system is known as the Density Functional Perturbation Theory (DFPT). This formalism is used to calculate linear-response functions, including phonon frequencies, heat capacities, thermal expansion coefficients, temperature dependence of the band gap, elastic, dielectric, and piezoelectric constants, and optical response in various materials.

In general, the formalism for nonlinear responses has been derived using the "$2n + 1$" theorem of perturbation theory

In section 2.1.1 we mentioned that the electron-density linear response of a system determines the matrix of its interatomic force constants. Let us see now how this response can be obtained within density-functional theory. The procedure described in the following is usually referred to as density-functional perturbation theory [31–34]. In order to simplify the notation and make the argument more general, we assume that the external potential acting on the electrons is a differentiable function of a set of parameters, $\lambda \equiv \lambda_i$ ($\lambda_i \equiv \mathbf{R}_I$ in the case of lattice dynamics). According to the Hellmann-Feynman theorem, the first and second derivatives of the ground-state energy read,

$$\frac{\partial E}{\partial \lambda_i} = \int \frac{\partial V_\lambda(\mathbf{r})}{\partial \lambda_i} n_\lambda(\mathbf{r}) d\mathbf{r}, \tag{2.70}$$

$$\frac{\partial^2 E}{\partial \lambda_i \partial \lambda_j} = \int \frac{\partial^2 V_\lambda(\mathbf{r})}{\partial \lambda_i \partial \lambda_j} n_\lambda(\mathbf{r}) d\mathbf{r} + \int \frac{\partial n_\lambda(\mathbf{r})}{\partial \lambda_i} \frac{\partial V_\lambda(\mathbf{r})}{\partial \lambda_i} d\mathbf{r}. \tag{2.71}$$

The electron-density response, $\partial n_\lambda(\mathbf{r})/\partial \lambda_i$, appearing in Eq. (2.71) can be evaluated by linearizing the equations that appear in subsection 2.2.5.3 with

27

respect to wave function, density, and potential variation. Linearization of equation (2.54) leads to,

$$\Delta n(\mathbf{r}) = 2\text{Re} \sum_i^{occ} \psi_n^*(\mathbf{r})\Delta\psi_n(\mathbf{r}), \qquad (2.72)$$

where the finite-difference operator Δ^λ is defined as,

$$\Delta^\lambda F = \sum_i \frac{\partial F_\lambda}{\partial\lambda_i}\Delta\lambda_i. \qquad (2.73)$$

The superscript λ has been omitted in Eq. (2.72), as well as in any subsequent formulas where such an omission does not give rise to ambiguities. Since the external potential (both unperturbed and perturbed) is real, each Kohn-Sham eigenfunction and its complex conjugate are degenerate. As a consequence, the imaginary part of the sum appearing in Eq. (2.72) vanishes, so that the prescription to keep only the real part can be dropped.

The first-order correction to a given eigenfunction of the Schrödinger equation is often expressed in terms of a sum over the spectrum of the unperturbed Hamiltonian,

$$\Delta\psi_n(\mathbf{r}) = \sum_{m\neq n} \psi_m(\mathbf{r})\frac{\langle\psi_m|\Delta V_{KS}|\psi_n\rangle}{\varepsilon_n - \varepsilon_m}, \qquad (2.74)$$

running over all the states of the system, occupied and empty, with the exception of the state being considered, for which the energy denominator would vanish. Using Eq. (2.74), the electron charge-density response, Eq. (2.72), can be cast into the form,

$$\Delta n(\mathbf{r}) = 2 \sum_i^{occ} \sum_{m\neq n} \psi_n^*(\mathbf{r})\psi_m(\mathbf{r})\frac{\langle\psi_m|\Delta V_{KS}|\psi_n\rangle}{\varepsilon_n - \varepsilon_m}. \qquad (2.75)$$

Equation (2.75) shows that the contributions to the electron-density response coming from products of occupied states cancel each other, so that the m index can be thought of as attaching to conduction states only. This is equivalent to saying that the electron-density distribution does not respond to a perturbation, which acts only on the occupied-state manifold (or, more generally, to the component of any perturbation which couples occupied states among each other).

2.3.1 Phonons

In crystalline solids, the nuclear positions appearing in the definition of the interatomic force constants Eq. (2.6), are labeled by an index I, which indicates the unit cell l to which a given atom belongs and the positions of the atom within that unit cell $I \equiv \{l, s\}$. The position of the Ith atom is thus [31],

$$\mathbf{R}_I \equiv \mathbf{R}_l + \boldsymbol{\tau}_s + \mathbf{u}_s(l), \tag{2.76}$$

where $\mathbf{R}_l$ is the position of the lth unit cell in the Bravais lattice, $\boldsymbol{\tau}_s$ is the equilibrium position of the atom in the unit cell, and $\mathbf{u}_s(l)$ indicates the deviation from equilibrium of the nuclear position. Because of translational invariance, the matrix of the interatomic force constants, Eq. (2.11), depends on l and m only through the difference $\mathbf{R} \equiv \mathbf{R}_l - \mathbf{R}_m$:

$$C_{st}^{\alpha\beta}(l, m) \equiv \frac{\partial^2 E}{\partial u_s^\alpha(l) \partial u_t^\beta(m)} = C_{st}^{\alpha\beta}(\mathbf{R}_l - \mathbf{R}_m), \tag{2.77}$$

where the Greek superscripts indicate Cartesian components. The Fourier transform of $C_{st}^{\alpha\beta}(\mathbf{R})$ with respect to $\mathbf{R}$, $\tilde{C}_{st}^{\alpha\beta}(q)$, can be seen as the second derivative of the Born-Oppenheimer energy surface with respect to the amplitude of a lattice distortion of definite wave vector:

$$\tilde{C}_{st}^{\alpha\beta}(\mathbf{q}) \equiv \sum_{\mathbf{R}} e^{-i\mathbf{q}\cdot\mathbf{R}} C_{st}^{\alpha\beta}(\mathbf{R}) = \frac{1}{N_c} \frac{\partial^2 E}{\partial u_s^{*\alpha}(\mathbf{q}) \partial u_t^{*\beta}(\mathbf{q})}, \tag{2.78}$$

where N_c is the number of unit cells in the crystal, and the vector $\mathbf{u}_s(q)$ is defined by the distortion pattern,

$$\mathbf{R}_I[\mathbf{u}_s(\mathbf{q})] = \mathbf{R}_l + \boldsymbol{\tau}_s + \mathbf{u}_s(\mathbf{q}) e^{i\mathbf{q}\cdot\mathbf{R}_l} \tag{2.79}$$

Phonon frequencies $\omega(q)$ are solutions of the secular equation,

$$\det \left| \frac{1}{\sqrt{M_s M_t}} \tilde{C}_{st}^{\alpha\beta}(\mathbf{q}) - \omega^2(\mathbf{q}) \right| = 0. \tag{2.80}$$

Translational invariance can be alternatively stated in this context by saying that a lattice distortion of wave vector $\mathbf{q}$ does not induce a force response in the crystal at wave vector $\mathbf{q}' \neq \mathbf{q}$, in agreement with the analysis carried out in Sec. 2.3. Because of this property, interatomic force constants are most easily calculated in reciprocal space and, when they are needed in direct space, can be readily obtained by Fourier transform.

If the dynamical matrices were known everywhere in the Brillouin zone, the IFCs could be built by inverting Eq. (2.78), which defines the dynamical matrix from the IFCs [34].

Unfortunately, the dynamical matrices are not known everywhere in the Brillouin zone: for computational reasons they are only obtained for a small set of wave vectors. For that purpose, the use of a discrete Fourier transform is tempting: the dynamical matrices on a regular grid of $(l \times m \times n)$ points in the Brillouin zone [35] will generate approximate IFCs in a large box, made of $(l \times m \times n)$ periodic cells. Outside of this box, the IFC's, are supposed to vanish.

2.3.2 Heat capacity

The specific heat is calculated in the harmonic approximation from the vibrational free energy $F(T)$. First it is necessary to obtain the entire phonon dispersion relations from total energy calculations, using DFPT, and to use them to evaluate $F(T)$. The references that the reader can consult are the same as the presented through this section.

The thermodynamic properties of a system are determined by the appropriate thermodynamic potential relevant to the given ensemble. In an ensemble where the sample volume and temperature are independent variables, the relevant potential is the Helmholtz free energy, $F = E - TS$. For a solid in the adiabatic approximation, the free energy can be written as the sum of an electric and a vibrational term. The electronic entropy contribution is easily evaluated in metals, although usually neglected, whereas it is totally negligible for insulators, $F_{el} \simeq E_{el}$. The key quantity to calculate in order to have access to the thermal properties and to the phase stability is the vibrational free energy $F(T)$ given by,

$$F(T) = - \int_0^\infty \left\{ \frac{\hbar\omega}{2} + k_B T \ln[2n_B(\omega)] \right\} \rho(\omega) d\omega. \tag{2.81}$$

From Eq. (2.81), the heat capacity is obtained with,

$$C_v = -T \left(\frac{\partial^2 F}{\partial T^2} \right)_v. \tag{2.82}$$

In Eq. (2.82), k_B is the Boltzmann constant, n_B the Bose-Einstein factor, and $\rho(\omega)$ the phonon density of states (PDOS). The high-frequency cutoff of the latter defines the upper limit of integration in Eq. (2.81).

2.4 Non-Collinear Magnetism Theory

Nowadays, there is a growing realisation of the importance of understanding the magnetic behaviour of systems in which the magnetic order is noncollinear. By noncollinear we mean that the magnetic moments associated with individual ions in the crystal are not aligned along the same axis . In some cases the existence of noncollinear arrangements of the magnetic moments does not imply a reduction of the symmetry associated with the high temperature space group. Noncollinear magnetism occurs even in chemically ordered systems, as well as a large number of systems based on rare earths [52]. In order to describe ferromagnetic or antiferromagnetic order, usually encountered in crystals, it is only necessary to consider spin alignment throughout the system. This approach is suitable for describing collinear magnetic structures and usually it is referred as spin-polarised approximation. However, noncollinearity is crucial for dealing with spin waves, magnetism at finite temperature, or to deal with magnetic excitations.

To correctly study the noncollinear magnetic structures it is necessary to introduce a two-component spinor wave function Ψ for the Kohn-Sham orbitals.

$$\Psi_i(\mathbf{r}, s) = \begin{pmatrix} \Psi_i^\alpha(\mathbf{r}) \\ \Psi_i^\beta(\mathbf{r}) \end{pmatrix}, \tag{2.83}$$

where the index i specifies the orbital among the set of Kohn-Sham orbitals $\{\Psi_i\}$ and $s \equiv \{\alpha, \beta\}$ the two spin indexes. The electron density, $n(\mathbf{r})$, and the vectorial spin density, $\mathbf{m}(\mathbf{r})$, used to represent the noncollinear magnetic structure are directly related to the density matrix ρ (see Appendix A for a more detailed information about this dependence). This matrix can be expanded in terms of the Pauli spin matrices and the scalar electron density as follow [53],

$$\begin{aligned} \rho(\mathbf{r}) &= \frac{1}{2}n(\mathbf{r})\mathbf{I} + \frac{1}{2}\left[m_x(\mathbf{r})\sigma_x + m_y(\mathbf{r})\sigma_y + m_z(\mathbf{r})\sigma_z\right], \\ &= \frac{1}{2}n(\mathbf{r})\mathbf{I} + \frac{1}{2}\mathbf{m}(\mathbf{r}) \cdot \boldsymbol{\sigma}. \end{aligned} \tag{2.84}$$

The elements of the density matrix in terms of the Kohn-Sham orbitals $\Psi^{\alpha,\beta}$ (see Eq. (2.83)) are given explicitly by,

31

$$\rho^{\alpha,\beta}(\mathbf{r}) = \begin{pmatrix} \rho^{\alpha,\alpha} & \rho^{\alpha,\beta} \\ \rho^{\beta,\alpha} & \rho^{\beta,\beta} \end{pmatrix}, \tag{2.85}$$

$$= \begin{pmatrix} \sum_i f_i \Psi_i^{*\alpha}(\mathbf{r})\Psi_i^{\alpha}(\mathbf{r}) & \sum_i f_i \Psi_i^{*\alpha}(\mathbf{r})\Psi_i^{\beta}(\mathbf{r}) \\ \sum_i f_i \Psi_i^{*\beta}(\mathbf{r})\Psi_i^{\alpha}(\mathbf{r}) & \sum_i f_i \Psi_i^{*\beta}(\mathbf{r})\Psi_i^{\beta}(\mathbf{r}) \end{pmatrix}, \tag{2.86}$$

where f_i is the occupation number of the ith Kohn-Sham orbital. In this scheme the individual eigenstates can have different spin quantisation directions. Furthermore, the spin quantisation axis of each state can vary with position. The electron and the vectorial spin densities can be written in terms of the matrix density in a really simple way,

$$n(\mathbf{r}) = \text{Tr}\rho, \tag{2.87}$$

$$\mathbf{m}(\mathbf{r}) = \text{Tr}(\rho\boldsymbol{\sigma}). \tag{2.88}$$

The full details about how to get these expressions, can be found in Appendix A. At this point, it is necessary to generalise all the equations that have been presented in previous chapters, but now, in terms of the density matrix. Because the purpose of this chapter is just to show the general noncollinear magnetism theory and not a deep comprehension of the same, here we shall present only the general Kohn-Sham expressions in terms of the density matrix. There exist many papers and reviews devoted to show in detail such generalization [36–43].

The exact Kohn-Sham density functional becomes (we use atomic units, $\hbar = m = e^2 = 1$),

$$E = \sum_{\alpha i} f_i \langle \Psi_i^{\alpha} | -\frac{1}{2}\nabla | \Psi_i^{\alpha} \rangle + E_H[\rho] + E_{XC} \tag{2.89}$$

The exchange-correlation energy $E_{XC}[n(\mathbf{r}), |\mathbf{m}(\mathbf{r})|]$ is computed with the formula given by Perdew and Zunger [18]. In the LDA approximation E_{XC} is indeed a functional of $n(\mathbf{r})$ and $|\mathbf{m}(\mathbf{r})|$. The expression for the exchange-correlation potential $V_{XC}^{\alpha,\beta}(r)$ can be obtained from E_{XC}. This exchange-correlation energy is defined in terms of the magnetization density (Eq. 2.87) and the total charge density (Eq. 2.88) as outlined below,

$$V_{XC}[\rho] \;=\; \int \frac{\delta E_{XC}[\rho]}{\delta \mathbf{n}(\mathbf{r})} d\mathbf{r} + \int \frac{\delta E_{XC}[\rho]}{\delta \mathbf{m}(\mathbf{r})} \mathbf{m}(\mathbf{r}) d\mathbf{r}, \tag{2.90}$$

$$=\; \int \frac{\delta E_{XC}[\rho]}{\delta \mathbf{n}(\mathbf{r})} d\mathbf{r} + \int \frac{\delta E_{XC}[\rho]}{\delta |\mathbf{m}(\mathbf{r})|} \frac{\partial |\mathbf{m}(\mathbf{r})|}{\partial \mathbf{m}(\mathbf{r})} \cdot \mathbf{m}(\mathbf{r}) d\mathbf{r}, \tag{2.91}$$

$$=\; \int \frac{\delta E_{XC}[\rho]}{\delta \mathbf{n}(\mathbf{r})} d\mathbf{r} + \int \frac{\delta E_{XC}[\rho]}{\delta |\mathbf{m}(\mathbf{r})|} |\mathbf{m}(\mathbf{r})| d\mathbf{r}, \tag{2.92}$$

the variations of the total energy with respect to the electronic density and the spin magnetic moment can be transformed and calculated from the equations used in the conventional collinear spin calculations. As is clear from Eq. (2.88), the $|\mathbf{m}(\mathbf{r})|$ has not only $\rho^{\alpha\alpha}$ and $\rho^{\beta\beta}$ but also $\rho^{\alpha\beta} \rho^{\beta\alpha}$. Therefore the exchange-correlation potential, V_{XC}, made from E_{XC} can be divided into diagonal and off-diagonal parts. Using the notation $V_{XC}^{\alpha\alpha}$ and $V_{XC}^{\beta\beta}$ for the diagonal part, and $V_{XC}^{\alpha\beta}$ and $V_{XC}^{\beta\alpha}$ for the off-diagonal part, the Kohn-Sham equation is finally written as,

$$\begin{pmatrix} -\dfrac{1}{2}\nabla^2 + V_H + V_{ext} + V_{XC}^{\alpha\alpha} & V_{XC}^{\alpha\beta} \\[2mm] V_{XC}^{\beta\alpha} & -\dfrac{1}{2}\nabla^2 + V_H + V_{ext} + V_{XC}^{\beta\beta} \end{pmatrix} \tag{2.93}$$

$$\times \begin{pmatrix} \Psi_i^{\alpha}(\mathbf{r}) \\ \Psi_i^{\beta}(\mathbf{r}) \end{pmatrix} = \varepsilon_i \begin{pmatrix} \Psi_i^{\alpha}(\mathbf{r}) \\ \Psi_i^{\beta}(\mathbf{r}) \end{pmatrix}, \tag{2.94}$$

each term was defined in previous chapters.

Note that in this scheme the individual eigenstates can have different spin quantization directions. Furthermore, the spin quantization axis of each state can vary with position. The theory presented in this section predict well defined sets of directions for the spins. When uncoupled from the underlying crystal lattice, all that is important is the relative orientation of the spins, *spin-orbit coupling* being necessary to couple the magnetization direction to the crystal lattice.

2.5 Spin-Orbit Coupling Theory

We start this section with an explanation, from the physical point of view, about the origin of the spin-orbit interaction. From a *qualitative point of view* the spin-orbit interaction can be understand as follow. Considering a central force, the valence electron experiences the electric field [54],

$$\mathbf{E} \ = \ -\frac{1}{e}\boldsymbol{\nabla}V_c(r), \tag{2.95}$$

$$= \ -\frac{1}{e}\frac{dV(r)}{dr}\frac{\mathbf{r}}{r} \tag{2.96}$$

where $V(r) = -\dfrac{e^2}{r}$. When the moving charge (an electron moving at a velocity $\mathbf{v} = \mathbf{p}/m_e$) is subjected to an electric field, e.g. the electrostatic field $\mathbf{E}$ created by the proton, it "feels" an effective magnetic field given by,

$$\mathbf{B}_{eff} = -\left(\frac{\mathbf{v}}{c}\right) \times \mathbf{E}. \tag{2.97}$$

Because the electron has an intrinsic magnetic moment $\boldsymbol{\mu}$ given by,

$$\boldsymbol{\mu} = \frac{e\mathbf{S}}{m_e c}, \tag{2.98}$$

it is easy to guess that the spin-orbit potential contributes to H as follows:

$$H_{LS} \ = \ -\boldsymbol{\mu}\cdot\mathbf{B}_{eff}, \tag{2.99}$$

in such a way that substituting las equations in this previous one, one gets,

$$
\begin{aligned}
H_{LS} \ &= \ -\boldsymbol{\mu}\cdot\mathbf{B}_{eff}, \\
&= \ \boldsymbol{\mu}\cdot\left(\frac{\mathbf{v}}{c}\times\mathbf{E}\right), \\
&= \ \frac{e\mathbf{S}}{m_e c}\cdot\left[\frac{\mathbf{p}}{m_e c}\times\left(-\frac{1}{e}\boldsymbol{\nabla}V_c(r)\right)\right], \\
&= \ \frac{e\mathbf{S}}{m_e c}\cdot\left[\frac{\mathbf{p}}{m_e c}\times\left(-\frac{1}{e}\frac{dV(r)}{dr}\frac{\mathbf{r}}{r}\right)\right], \\
&= \ \frac{1}{m_e^2 c^2}\frac{1}{r}\frac{dV_c}{dr}(\mathbf{L}\cdot\mathbf{S}), \\
&= \ \frac{e^2}{m_e^2 c^2}\frac{1}{r^3}(\mathbf{L}\cdot\mathbf{S}). \tag{2.100}
\end{aligned}
$$

here we have used the expression, $\mathbf{p}\times\mathbf{r} = -\mathbf{L}$, for the angular momentum quantum mechanical operator. In last equation it is necessary to introduce a $1/2$

factor because the motion of the electron around the nucleus is not rectilinear. This term is called the giromagnetic ratio. The electron spin therefore rotates with respect to the laboratory reference frame.

In general Eq. (2.100) then represents the interaction of the magnetic moment of the electron spin within the magnetic field "seen" by the electron because of its motion in the electrostatic field of the proton.

2.5.1 The Dirac equation

The object is to derive a relativistic wave equation for a spin-$\frac{1}{2}$ particle. It is possible to incorporate the spin into the general framework of relativistic quantum mechanics by taking the operator analog of the classical expression [7, 55],

$$(E^2/c^2) - \mathbf{p}^2 = (mc)^2, \qquad (2.101)$$

and rewritten the equation as,

$$\left(\frac{\hat{E}}{c} - \boldsymbol{\sigma} \cdot \mathbf{p} \right) \left(\frac{\hat{E}}{c} + \boldsymbol{\sigma} \cdot \mathbf{p} \right) = (mc)^2, \qquad (2.102)$$

this alternative form is indistinguishable from the previous one for all practical purposes when there is no vector potential. It is easy to show such asseveration using the identity,

$$(\boldsymbol{\sigma} \cdot \mathbf{A})(\boldsymbol{\sigma} \cdot \mathbf{B}) = \mathbf{A} \cdot \mathbf{B} + i\boldsymbol{\sigma} \cdot (\mathbf{A} \times \mathbf{B}). \qquad (2.103)$$

Considering the operators,

$$\hat{E} = i\hbar \frac{\partial}{\partial t} = i\hbar c \frac{\partial}{\partial x_0}; \qquad\qquad \mathbf{p} = -i\hbar \boldsymbol{\nabla}, \qquad (2.104)$$

it is possible to find a second order derivative equation for a free electron as,

$$\left(i\hbar \frac{\partial}{\partial x_0} + \boldsymbol{\sigma} \cdot i\hbar \boldsymbol{\nabla} \right) \left(i\hbar \frac{\partial}{\partial x_0} - \boldsymbol{\sigma} \cdot i\hbar \boldsymbol{\nabla} \right) \Psi = (mc)^2 \Psi, \qquad (2.105)$$

where Ψ is a *two-component* wave function.

It is desirable to obtain a wave equation of first order in the time derivative. The price that we have to pay in order to get it is to increase the number of

components when we work with the first order equation. It is possible to show that the famous Dirac equation can be written as,

$$\left(\boldsymbol{\gamma} \cdot \boldsymbol{\nabla} + \gamma_4 \frac{\partial}{\partial(ix_0)} \right) \Psi + \frac{mc}{\hbar} \Psi = 0, \tag{2.106}$$

or more convenient as,

$$\left(\gamma_\mu \frac{\partial}{\partial x_\mu} + \frac{mc}{\hbar} \right) \Psi = 0, \tag{2.107}$$

where γ_μ with $\mu = 1, 2, 3, 4$ are the 4×4 matrices given by,

$$\gamma_\mu = \begin{pmatrix} 0 & -i\sigma_i \\ i\sigma_i & 0 \end{pmatrix}, \quad \gamma_4 = \begin{pmatrix} \mathbf{I} & 0 \\ 0 & -\mathbf{I} \end{pmatrix}, \tag{2.108}$$

which really mean,

$$\gamma_3 = \begin{pmatrix} 0 & 0 & -i & 0 \\ 0 & 0 & 0 & i \\ i & 0 & 0 & 0 \\ 0 & -i & 0 & 0 \end{pmatrix}, \quad \gamma_4 = \begin{pmatrix} 1 & 0 & 0 & 0 \\ 0 & 1 & 0 & 0 \\ 0 & 0 & -1 & 0 \\ 0 & 0 & 0 & -1 \end{pmatrix}, \quad \text{etc.} \tag{2.109}$$

Equation 2.107 is the famous Dirac equation. Here we just write γ_3 but γ_1 and γ_2 can be written remembering the 2×2 Pauli matrices defined in Appendix A.

Here it is important to emphasize that Eq. (2.107) is actually a four differential equations that couple the four components of Ψ represented by a single-column matrix,

$$\Psi = \begin{pmatrix} \psi_1 \\ \psi_2 \\ \psi_3 \\ \psi_4 \end{pmatrix}. \tag{2.110}$$

A four-component object of this kind is known as a *bispinor*. Multiplying Eq. (2.106) by γ_4, we see that the Dirac equation can also be written in the Hamiltonian form,

$$H\Psi = i\hbar(\partial\psi/\partial t), \tag{2.111}$$

where,

$$H\Psi = (-ic\hbar\boldsymbol{\alpha}\cdot\boldsymbol{\nabla} + \beta mc^2)\Psi, \tag{2.112}$$

$$= (c\,\boldsymbol{\alpha}\cdot\mathbf{p} + \beta mc^2)\Psi = i\hbar\frac{\partial}{\partial t}\Psi, \tag{2.113}$$

with,

$$\beta = \gamma_4 = \begin{pmatrix} \mathbf{I} & 0 \\ 0 & -\mathbf{I} \end{pmatrix}, \quad \alpha_k = i\gamma_4\gamma_k = \begin{pmatrix} 0 & \sigma_k \\ \sigma_k & 0 \end{pmatrix}. \tag{2.114}$$

Until here we have just written the general expression for the Dirac equation but the aim of this subsection is to obtain the spin-orbit interaction term, in a natural way, from the Dirac equation.

In the case of a spherical potential $V(r)$, one can make use of conservation of parity an total angular momentum denoted by quantum numbers jm. Then the wavefunction for each principle quantum number n can be written in terms of radial and angular-spin functions.

$$\Psi^l_{njm} = \begin{pmatrix} g_{nj}(r)\psi^l_{jm} \\ \\ if_{nj}(r)\dfrac{\boldsymbol{\sigma}\cdot\mathbf{r}}{r}\psi^l_{jm} \end{pmatrix}, \tag{2.115}$$

which defines two functions with the same jm but opposite parity for the two possible values $l = j \pm \frac{1}{2}$. The two-component functions ψ^l_{jm} can be written explicitly in terms of the spherical harmonics (see for instance R. Martin book, page 194 [7]). The resulting equations for the radial functions are simplified if we define the energy,

$$\varepsilon' = \varepsilon - mc^2, \tag{2.116}$$

a radially varying mass,

$$M(r) = m + \frac{\varepsilon' - V(r)}{2c^2}, \tag{2.117}$$

and the quantum number κ,

$$\kappa = \pm(j+\tfrac{1}{2}) \quad \begin{cases} +, & \text{if } l = j + \dfrac{1}{2} \Rightarrow \kappa = l \\ -, & \text{if } l = j - \dfrac{1}{2} \Rightarrow \kappa = -(l+1) \end{cases} \tag{2.118}$$

Note that $\kappa(\kappa+1) = l(l+1)$ in either case. Then the coupled equations can be written in the form of the radial equations,

$$
\begin{aligned}
&-\frac{\hbar^2}{2M}\frac{1}{r^2}\frac{d}{dr}\left(r^2\frac{dg_{n\kappa}}{dr}\right) + \left[V + \frac{\hbar^2}{2M}\frac{l(l+1)}{r^2}\right]g_{n\kappa} \\
&-\frac{\hbar^2}{4M^2c^2}\frac{dV}{dr}\frac{dg_{n\kappa}}{dr} - \frac{\hbar^2}{4M^2c^2}\frac{dV}{dr}\frac{1+\kappa}{r}g_{n\kappa} = \varepsilon'g_{n\kappa},
\end{aligned} \tag{2.119}
$$

$$
\tag{2.120}
$$

and,

$$
\frac{df_{n\kappa}}{dr} = \frac{1}{\hbar c}(V - \varepsilon')g_{n\kappa} + \frac{\kappa-1}{r}f_{n\kappa}. \tag{2.121}
$$

These are general equations for a spherical potential; no approximations have been made thus far. Equation (2.119) is the same as an ordinary Schrödinger equation except that the mass M is a function of radius and there are two added terms on the left-hand side, which are, respectively, the Darwin term and the spin-orbit coupling. The latter can be written out explicitly in terms of the spin using the relation,

$$
\mathbf{L}\cdot\boldsymbol{\sigma}\,\psi_{\kappa m} = -\hbar(1+\kappa)\psi_{\kappa m}, \tag{2.122}
$$

where $\psi_{\kappa m}$ is the appropriate ψ^l_{jm} determined by κ.

2.5.1.1   Scalar Relativistic Equation (Spin-Orbit Coupling)

If we make the approximation that the spin-orbit term is small, then we can omit it in the radial equations for g and f and treat it by perturbation theory. Then last three equations depend only upon the principle quantum number n and orbital angular momentum l and can be written in terms of the approximate functions, $\tilde{g}_{nl}$ and $\tilde{f}_{nl}$, leading to [7, 44],

$$
-\frac{\hbar^2}{2M}\frac{1}{r^2}\frac{d}{dr}\left(r^2\frac{d\tilde{g}_{nl}}{dr}\right) + \left[V + \frac{\hbar^2}{2M}\frac{l(l+1)}{r^2}\right]\tilde{g}_{nl} - \frac{\hbar^2}{4M^2c^2}\frac{dV}{dr}\frac{d\tilde{g}_{nl}}{dr}
$$
$$
= \varepsilon'\tilde{g}_{nl}, \tag{2.123}
$$

and,

$$\tilde{f}_{nl} = \frac{\hbar}{2Mc}\frac{d\tilde{g}_{nl}}{dr}, \tag{2.124}$$

with the normalization condition,

$$\int (\tilde{g}_{nl}^2 + \tilde{f}_{nl}^2) r^2 dr = 1. \tag{2.125}$$

Equation (2.123) is the scalar relativistic radial equation, which can be solved by the same techniques as the usual non-relativistic equation. The other equations can then be treated easily on the radial grid. Together with relation (2.122) the spin-orbit Hamiltonian coupling the large components of the wavefunction has the form,

$$\hat{H}_{SO} = -\frac{\hbar^2}{2M^2c^2}\frac{1}{r}\frac{dV}{dr}\mathbf{L}\cdot\boldsymbol{\sigma}, \tag{2.126}$$

which can often be treated as a small perturbation. Since this term originates deep in the core near the nucleus where $\frac{1}{r}\frac{dV}{dr}$ is large, the present spherical derivation of the spin-orbit term carries over from the atom to a solid or molecule.

$$\left[\frac{\mathbf{p}^2}{2m} + eA_0 - \frac{\mathbf{p}^4}{8m^3c^2} - \frac{e\hbar\,\boldsymbol{\sigma}\cdot(\mathbf{E}\times\mathbf{p})}{4m^2c^2} - \frac{e\hbar^2}{8m^2c^2}\,\boldsymbol{\nabla}\cdot\mathbf{E}\right]\Psi = E\Psi. \tag{2.127}$$

Another way to get the spin-orbit approximation term is applying the Zero-Order Regular Approximation (ZORA) to the Dirac equation. It is done solving the ZORA equation, which is obtained as the zero-order equation in the regular expansion in $E/(2c^2 - V)$ of the Dirac equation. The one-electron relativistic KohnSham equations are solved in the scalar relativistic and in the fully relativistic case (including the spinorbit operator) [56].

2.5.2   Relativistic Effects Using Pseudopotentials

The way to include relativistic contributions, like the spin-orbit interaction, in DFT is through the use of pseudopotentials [45]. As was explained in section 2.2.10 there exist different kinds of pseudopotentials such relativistic interaction. The Hartwigsen-Goedecker-Hutter (HGH) pseudopotential is just one of these.

Pseudopotentials are an essential ingredient for efficient electronic and vibrational structure calculations . First, by eliminating the core electrons, the number of orbitals that has to be calculated is reduced. Second, the pseudo-wave-functions are much smoother in the core region than the all-electron wave functions and the number of basis functions can therefore be reduced. Especially if plane waves are used as a basis set this reduction of the size of the basis set is essential. Concerning relativistic pseudopotentials the introduction of the norm-conserving property [46] made pseudopotentials an easy to handle and popular tool for electronic structure calculations. Many attempts have since then been made to construct norm-conserving pseudopotentials [47], which are numerically more efficient than the original ones. The introduction of the separable form of the norm-conserving pseudopotentials was a major advance [48]. More recently also ultrasoft pseudopotentials including spin-orbit coupling have been introduced [49]. The HGH is a separable dual-space Gaussian [50] pseudopotential. This PP is generated on the basis of a fully relativistic all-electron calculation, i.e., by solving the two-component Dirac equation. This PP is given in both the local density approximation and the generalized gradient approximation. Just like a remark, it is well known that relativistic effects up to order α^2, where α is the fine-structure constant [51], can be included in electronic structure calculations by solving nonrelativistic Kohn-Sham equations with PPs tailored to reproduce the solution of fully relativistic atomic Dirac-like equations.

The total HGH pseudopotential is given by,

$$V(\mathbf{r}, \mathbf{r}') = V_{loc}(r)\delta(\mathbf{r} - \mathbf{r}') + \sum_l V_l(\mathbf{r}, \mathbf{r}') + \Delta V_l^{SO}(\mathbf{r}, \mathbf{r}')\mathbf{L} \cdot \mathbf{S}, \qquad (2.128)$$

where $V_{loc}(r)$ correspond to the local part of the pseudopotential, $V_l(\mathbf{r}, \mathbf{r}')$ is the nonlocal contribution, and $V_l^{SO}(\mathbf{r}, \mathbf{r}')$ is the relativistic, spin-orbit coupling, contribution to the PP. Each of these are now scalar relativistic quantities but with the same form as the non-relativistic case.

The full expression for the local part V_{loc} of the pseudopotential is given by,

$$V_{loc}(r) = \frac{-Z_{ion}}{r}\text{erf}\left(\frac{r}{\sqrt{2}r_{loc}}\right) + \exp\left[-\frac{1}{2}\left(\frac{r}{r_{loc}}\right)^2\right] \qquad (2.129)$$

$$\times \left[C_1 + C_2\left(\frac{r}{r_{loc}}\right)^2 + C_2\left(\frac{r}{r_{loc}}\right)^4 + C_2\left(\frac{r}{r_{loc}}\right)^6\right], \qquad (2.130)$$

where erf denotes the error function. Z_{ion} is the ionic charge of the atomic core, i.e., the total charge minus the charge of the valence electrons.

Now we write the full expression for the nonlocal contribution $V_l(\mathbf{r}, \mathbf{r}')$ to the pseudopotential which is a sum of separable terms,

$$V_l(\mathbf{r}, \mathbf{r}') = \sum_{i=1}^{3} \sum_{j=1}^{3} \sum_{m=-l}^{+l} Y_{l,m}(\hat{\mathbf{r}}) p_i^l(r) h_{i,j}^l p_j^l(r') Y_{l,m}^*(\hat{\mathbf{r}}'), \qquad (2.131)$$

where $Y_{l,m}$ are the spherical harmonics, and l the angular momentum quantum number. The projectors $p_i^l(r)$ satisfy the normalisation condition and in both real and Fourier space, the projectors have the form of a Gaussian multiplied by a polynomial, please take a look in [29] to see in detail these expressions. An special property of this PP is that it has an analytical form if expressed in reciprocal space. Due to this property the dual-space Gaussian pseudopotential is the optimal compromise between good convergence properties in real and Fourier space.

In the relativistic case the spin orbit coupling splits up all orbitals with l 0 into spin-up and spin-down orbitals with an overall angular momentum $j = l \pm 1/2$. So for each angular-momentum l 0, one spin-up orbital and one spin-down orbital with different wave functions and pseudopotentials exist.

Finally to express $\Delta V_l^{SO}(\mathbf{r}, \mathbf{r}')$ we just replace the $h_{i,j}^l$ in equation (2.131) by different parameters $k_{i,j}^l$, i.e.,

$$\Delta V_l^{SO}(\mathbf{r}, \mathbf{r}') = \sum_{i=1}^{3} \sum_{j=1}^{3} \sum_{m=-l}^{+l} Y_{l,m}(\hat{\mathbf{r}}) p_i^l(r) k_{i,j}^l p_j^l(r') Y_{l,m}^*(\hat{\mathbf{r}}'), \qquad (2.132)$$

We used this pseudopotential in our calculations, mainly because the simplicity of the PP but also because since the spin-orbit coupling term is separable, we were able to include or remove such term according to our convenience as will be explained in next chapters.

2.6 The ABINIT code

ABINIT is a package whose main program allows one to find the total energy, charge density and electronic structure of systems made of electrons and nuclei (molecules and periodic solids) within Density Functional Theory (DFT), using pseudopotentials and a plane wave basis. *ABINIT* also includes options

to optimise the geometry according to the DFT forces and stresses, or to perform molecular dynamics simulations using these forces, or to generate dynamical matrices, Born effective charges, and dielectric tensors. Excited states can be computed within the Time-Dependent Density Functional Theory (for molecules), or within Many-Body Perturbation Theory (the GW approximation). In addition to the main *ABINIT* code, different utility programs are provided.

Some of the available features are,

- Representation of wavefunctions : Plane Waves; Projector-Augmented Waves (the latter is not available for all capabilities).

- LDA, GGA, spin-DFT (many functional forms).

- Band structure, DOS, charge density, total energy.

- Many pseudopotential types : availability of Troullier-Martins and Hartwigsen-Goedecker-Hutter pseudopotentials for the full periodic table, interface with different pseudopotential codes, including FHI98PP, and N. Holzwarth PAW pseudo generator. Generation of alchemical pseudo-atoms.

- Finite systems as well as insulators and metals (smearings : Fermi, Gaussian, Gauss-Hermite, Marzari modifications).

- Automatic k-point sampling of the irreducible Brillouin zone.

- Symmetry analyser (includes a database of the 230 spatial groups, and a database of the 1191 Shubnikov magnetic groups).

- Forces, stresses, automatic optimisation of atomic positions and unit cell parameters (Broyden and Molecular dynamics with damping)

- Molecular dynamics (Verlet or Numerov), Nose thermostat, Langevin dynamics.

- Spin-orbit coupling compatible with spin-polarisation

- Responses to atomic displacements (even at non-zero wavevectors, without need of supercells !) and to homogeneous electric fields, within Density-Functional Perturbation Theory: dielectric tensor, Born effective charges, dynamical matrices at any wavevector, phonon frequencies, force constants phonon density of states, thermodynamic properties in the quasi-harmonic approximation.

- Responses to strain perturbations: elastic constants, piezoelectric coefficients.

- Non-linear responses thanks to the 2n+1 theorem of perturbation theory : at present, electro-optic coefficients, Raman cross-sections.

- Susceptibility matrix by sum over states excited states of atoms and molecules within Time Dependent-DFT or Delta SCF.

- Frequency-dependent conductivity in the RPA (Kubo-Greenwood).

- Exact exchange and RPA+ calculation of total energies (one k-point, post-LDA or post-GGA, not yet available for spin-polarized systems or spinor wavefunctions).

- GW calculation of excited states.

- MPI parallelisation of ground-state and response-function calculations over k-points, spins and bands, MPI parallelisation of FFT grid and planewave operations. coefficients,

As a final remark it is important to mention that the theory given in this chapters can not be implemented as it is in the *ABINIT* code. A perfect example about this issue is the computation of $\rho^{\alpha,\beta}(r) = \sum_n f_n \langle r|\Psi^\alpha\rangle\langle\Psi^\beta|r\rangle$. One would like to calculate this quantity as was defined in section 2.4, whereas $\rho^{\alpha,\beta}(r)$ is hermitian and in general can have complex elements. The problem is that in *ABINIT* the subroutine devoted to do this calculation transforms only real quantities. The *trick* is to use only real quantities as follow [42, 57],

$$\rho^{\alpha,\alpha}(r) = \sum_n f_n \langle r|\Psi^\alpha\rangle\langle\Psi^\alpha|r\rangle, \tag{2.133}$$

$$\rho^{\beta,\beta}(r) = \sum_n f_n \langle r|\Psi^\beta\rangle\langle\Psi^\beta|r\rangle, \tag{2.134}$$

$$n(r) + m_x(r) = \sum_n f_n (\Psi^\alpha + \Psi^\beta)^*_n (\Psi^\alpha + \Psi^\beta)_n, \tag{2.135}$$

$$n(r) + m_y(r) = \sum_n f_n (\Psi^\alpha - i\Psi^\beta)^*_n (\Psi^\alpha - i\Psi^\beta)_n, \tag{2.136}$$

and compute $(n(r), \mathbf{m}(r))$ with the help of the additional quantities,

$$n(r) = \rho^{\alpha,\alpha}(r) + \rho^{\beta,\beta}(r), \tag{2.137}$$

$$m_z(r) = \rho^{\alpha,\alpha}(r) - \rho^{\beta,\beta}(r). \tag{2.138}$$

It is an example that exemplify adaptation to the theory that are necessary in order to be implemented in the *ABINIT* code.

To close this chapter, I have to mention that the *ab initio* code that was used to develop my doctoral research was the *ABINIT* code.

Part II

Applications

Chapter 3

Bismuth Phonons

3.1 Phonon band structure and interatomic force constants for Bismuth: the crucial role of spin-orbit interaction

The dynamical properties and the interatomic force constants for Bismuth (Bi) are investigated from first principles with the use of density functional theory. In this context, Bi has two striking characteristics : it is a semimetal with a very small carrier density, and the spin-orbit (SO) coupling is particularly strong. To decouple these characteristics, we treat Bi as (i) non-metallic without SO interaction, (ii) metallic with, and (iii) without SO interaction. Phonon dispersion relations and interatomic force constants are reported and compared with available experimental data, and a very good agreement is obtained only when SO interaction is taken into account : removing this interaction causes a difference on the order of 10% in the phonon frequencies and interatomic force constants. Such a difference is also present in the Bi_2 molecule. We also determine which phonon bands are more affected directly by the SO interaction and which bands are indirectly affected, through changes in cell parameters. The dependence of the latter with respect to the SO coupling is also reported.

3.2 Introduction

The electronic configuration for bismuth is $[He]4f^{14}5d^{10}6s^26p^3$ but only the $6s^26p^3$ electrons can be considered as valence electrons, that because only s

and p levels will mix in the solid, while the other d-electron and core electron levels will remain practically unchanged. Considering only those five external electron configuration it was previously shown that the splitting of the p levels further split into two level due to spin-orbit effect [61]. The amplitude of the p-level splitting is approximately 1.5 eV. This coupling leads to the suppression of several specific degeneracies, which can be observed in the electronic band structure.

Crystalline Bismuth (Bi) is the most diamagnetic elemental solid [58] and presents also the highest Hall effect among such solids. Being a semimetal, with an extremely low carrier density (less than 2×10^{-5}) accompanied by high carrier mobility, it is in many respects an ideal material for probing quantum confinement phenomena [59]. At the same time, the Bi nucleus is quite heavy, with atomic number $Z = 83$. Because electrons may move at a speed close to light velocity in the interior of such an atom, a purely non-relativistic description of Bi does not suffice.

The lowest-order relativistic corrections are of two types : first, a spin-scalar modification of the kinetic and potential operator, and second, a vector coupling, between the spin and the electron momentum. Supposing that an electron moves in an electric field $\mathbf{E}$, one can crudely attribute this vector coupling to the fact that the moving electron "sees" an apparent magnetic field given by $\mathbf{E} \times (\mathbf{v}/c)$. Actually, it has the following analytical expression in international units [55] $(-(e\hbar/2mc)\, \sigma \cdot [\mathbf{E} \times (\mathbf{v}/c)])$, which can be expressed for a central field, by a total spin and orbital angular momentum interaction Hamiltonian [60], proportional to $\mathbf{L} \cdot \mathbf{S}$, termed spin-orbit (SO) interaction.

The importance of the latter on *electronic* properties has been thoroughly studied, for many different systems. In the case of crystalline Bi, it has been analyzed from first principles [61]. This work shows that the SO interaction split the external p atomic levels, by about 1.5 eV ($6p_{1/2}$ $6p_{3/2}$ splitting), an effect that can be seen in the electronic density of states of the periodic solid. Because for an s level the angular momentum is equal to zero, the two $6s$ bands are practically unaffected by the SO coupling.

The effect of the SO interaction on the total energy, as well as *geometrical* and *dynamical* properties of materials has been the subject of less attention. Scaling roughly as the fourth power of the atomic number Z, the energy changes are tiny in hydrogen atom, but becomes much more significant for the heavier elements [62]. One might mention the detailed study of the SO influence on the crystallographic parameters and bulk modulus of light actinides, in Refs. [63] and [64]. It was observed that the SO coupling has some importance (less than

2 percents usually for the lattice parameter, but up to 10 percents for the Neptunium lattice parameter as well as the bulk modulus) and brings systematically the predicted values in better agreement with the experiment. In the very recent studies of the phonon band structure of Thorium[65] and Bi[66, 67], the SO coupling was included in all the calculations, but these works do not discuss the specific impact of the SO interaction on the frequency spectrum. In the case of the Bismuth study, the effect of a largely increased density of carrier, obtained by femtosecond laser irradiation, is seen on the crystallographic parameters.

In the present study, we examine the phonon band structure of Bi, and find that the semimetallicity has little importance, but that the inclusion of SO is mandatory for an accurate description of the spectrum, reducing the discrepancy from up to fifteen percents down to a few percents in most of the Brillouin zone. We also analyze the IFCs and find that the SO interaction causes significant changes both in the longitudinal and transverse components, on the order of twenty five percent for some specific elements of the IFC matrix, compared to the same values without the SO interaction. Optical branches are more affected directly by that coupling than acoustic branches. The crystallographic parameters of Bi, on the contrary, are hardly affected (less than one percent) by both semimetallicity and SO coupling, in agreement with previous works [63, 64], but this modification triggers non-negligible modifications of the the frequencies for acoustic branches.

We rely on the Density Functional Theory (DFT), with a plane-wave basis set and norm-conserving pseudopotentials. Instead of using the fully relativistic Dirac equation to study the periodic solid, one can, in this framework, generate ionic pseudopotentials that combine scalar-relativistic and SO terms, and represent them by fully nonlocal pseudopotentials of separable form [46, 48]. The usual Kohn-Sham equations can then be solved in the total potential created by such ionic pseudopotentials.

In section 3.3, we describe our theoretical technique, and discuss the different cases that allow us to disentangle the modifications due to semimetallicity, due to the influence of SO coupling on the crystallographic parameters, and due to the direct influence of SO coupling on the total energy. In section 3.4.1, we report our study of the crystallographic parameters of Bi, crystallizing in the rhombohedral A7 structure. Three crystallographic parameters describe fully this structure : the lattice parameter (a_0), the rhombohedral angle (α), and one internal coordinate z. In section 3.4.2, we present the full phonon band structure, and compare it with experimental values along the trigonal direction. In section 3.4.3, we discuss the interatomic force constants in Bi and consider them with

respect to both the rhombohedral A7 structure of Bi and the SO coupling. We examine them also in the Bi_2 molecule including the change due to SO coupling.

3.3   Methodology

In order to calculate properties like phonon frequencies structure, and inter-atomic force constants for Bi, we used the *ABINIT* code [68–70]. This package performs density functional calculations of material properties using pseudopotentials and a plane-wave basis set. The exchange-correlation energy was computed using the local density approximation (LDA) in the Teter-Pade parametrization [50]. We used the Hartwigsen-Goedecker-Hutter (HGH) pseudopotential [29] which is a norm-conserving relativistic separable dual-space Gaussian pseudopotential and is generated on the basis of a fully relativistic all-electron calculation. Using this pseudopotential, we included SO interaction effects relevant for heavier elements like Bi. It is possible to reproduce only scalar relativistic effects by neglecting the terms for the SO contribution from HGH : this pseudopotential contains separately an average potential (that contains all scalar parts of the relativistic pseudopotential), and a vector part. The phonon frequencies and interatomic force constants have been computed in the framework of Density Functional Perturbation Theory (DFT), also implemented in *ABINIT* [32, 34] with and without the SO coupling.

We used a $12 \times 12 \times 12$ Monkhorst-Pack special point grid [71] to approximate the integrals on the wavevectors of the electronic wavefunction over the entire first Brillouin-zone. With respect to this parameter, our choice gives a convergence of 10^{-5} in lattice parameters (a_0), and 10^{-4} in rhombohedral angles (α). The electronic wavefunctions were expanded in plane waves up to a kinetic energy cutoff of 15 Hartree, resulting in errors of $\sim 1\%$, or less, in the phonon frequency values (ω). The dynamical matrix were computed on a mesh of $8 \times 8 \times 8$ wavevectors in the Brillouin zone, using a variational formulation of the density-functional perturbation theory [32, 34]. Finally, computational results were compared with experimental values published by J. L. Yarnell [72] and reported by D. B. Smith [73]. In Ref. [67], a very similar methodology was also applied to the study of the phonon band structure of Bi, whereas our samplings of the Brillouin zone for the dynamical matrices is finer, and we primarily focus here on the role of the SO coupling.

We studied seven different possibilities in order to disentangle the effects coming from the metallicity, and those related to spin-orbit coupling, coming

either directly from a modification of the total energy and its derivatives at fixed crystallographic parameters, or, indirectly, from the modification of the crystallographic parameters without change in the treatment (with or without SO) of the total energy. (a) In the first case, we considered Bi as non-metallic, and did not take into account the SO coupling when relaxing the crystallographic parameters and computing the phonon band structure. This is our only computation corresponding to a non-metallic case. As will be detailed briefly later, the metallic or non-metallic treatments give essentially identical results, for both lattice parameters and phonon band structures. (b) In a second case, we considered Bi as metallic, and again did not take into account the SO coupling when relaxing the crystallographic parameters and computing the phonon band structure. "Theoretical crystallographic parameters without SO coupling - Phonons without SO coupling" and abbreviate it TCWoSO-PhWoSO. (c) The same relaxed cell parameters (TcWoSO case) were used and the phonon spectra was calculated with full treatment of the SO coupling (TcWoSO-PhWSO). (d) Then, the relaxed geometrical cell parameters were obtained taking into account the SO contribution (TcWSO case). Using this cell parameter, we obtained the corresponding phonon frequencies considering the SO contribution (TcWSO-PhWSO). This is our best fully theoretical computation of the phonon band structure. (e) Using the same crystallographic parameters (TcWSO case), we also obtained the phonon spectra in the absence of the SO contribution (TcWSO-PhWoSO). (f) Experimental crystallographic parameters were also used (Ec), to start a computation of the phonon band structure with SO interaction (Ec-WSO) was considered. (g) Finally, we considered experimental crystallographic parameters without the SO contribution (Ec-WoSO).

The scheme used in the metallic case was the Gaussian smearing, corresponding to the 2-order Hermite polynomial of Ref. [74]. The broadening of occupation numbers was determined by a smearing energy of 0.001 Ha.

3.4 Results

3.4.1 Geometry optimization

As mentioned in the Introduction (see section 3.2), Bi has a rhombohedral A7 crystal structure, with two atoms per unit cell, and three independent parameters : the value of the rhombohedral angle α, the length of the rhombohedral unit cell primitive vectors a_0, and the position of the second atom (labeled as D in FIG. 3.1) along the trigonal axis determined by the ratio $z = \overline{BD}/\overline{BH}$. The

A7 crystal structure can be derived from a simple cubic geometry structure, with a Peierls instability causing the movement of the atoms and the final geometry: the atom labeled as D is located along the trigonal axis and is very close to the center of the cell ($z \sim 0.5$), but slightly displaced along the trigonal axis. Due to this displacement, there exist three nearest and three next nearest neighbors. In agreement with this picture, Bi might also be thought as being made of a (1 1 1) stacking of atomic bilayers, a characterization that has been confirmed by the analysis of the charge density, from first-principles studies [61]. The three nearest-neighbor atoms are to be found in the other (1 1 1) atomic plane belonging to the bilayer, with an angle between nearest-neighbor atoms that is equal to 94.84 degrees for the case without SO, and equal to 95.63 degrees for the case with SO.

We report crystallographic parameters in TABLE 3.1 for each of the cases described in Section 3.3. In addition, we report the corresponding values for the nearest atoms a_{NN} and the distance between the atoms labeled as $\overline{BD}$, and $\overline{DH}$ in FIG. 3.1.

The variations observed in the crystallographic parameters between the non-metallic and metallic cases are very small, less than 0.2%. When the SO coupling is turned on, the lattice parameter expands by about 0.9%, and the internal parameter z is decreased by about 0.6%, while the rhombohedral angle increase but is hardly affected. These parameters give a volume for the A7 rhombohedral unit cell equal to 67.10 Å^3, and 69.07 Å^3 for the metallic without and with SO interaction respectively. The corresponding experimental volume [67] is equal to 69.97Å. The theoretical discrepancy with respect to the experimental results (Ec) is reduced from $\sim$ 4.3 % without SO coupling (TcWoSO) to $\sim$ 1.3 % considering such interaction (TcWSO).

3.4.2 Phonon frequencies

In a A7-type lattice, there are two atoms per primitive unit cell and hence six phonon branches. These are divided into three acoustic and three optical phonon branches. Along the Γ-T direction, corresponding to the z axis, and preserving the trigonal symmetry, the phonon dispersion curves can be classified as E_g or A_{1g}, according to whether their displacements are perpendicular or parallel to the direction of the wave vector $\mathbf{q}$ respectively. For the acoustic (A) or optical (O) A_{1g} phonon modes, the atoms moves in the direction of the trigonal axis. For the other two acoustic or optical E_g phonon modes, the atoms move in the perpendicular plane with respect to this axis. In the related (z=0.5) cubic geom-
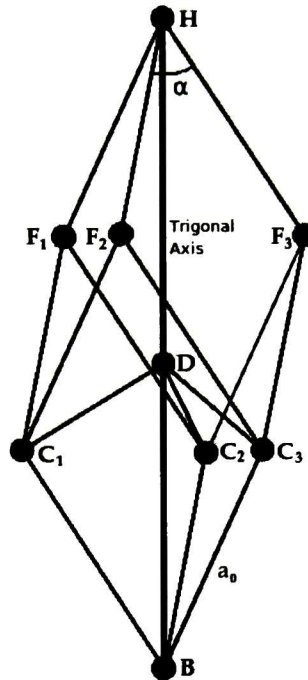
Figure 3.1: A7 rhombohedral unit cell for Bi.

etry, the A_{1g} and E_g phonon modes would be degenerate, but the degeneracy is lifted in the A7 geometry due to the Peierls distortion [75].

In TABLE 3.2, we report phonon frequencies along the Γ-T direction, from experiment (Ref. [72]), as well as for three different cases mentioned in section 3.3 (TcWSO-PhWSO ; Ec-PhWSO ; TcWoSO-PhWoSO). We do not report the values for the non-metallic case, as they do not differ from the metallic one by more than 0.6%. The different phonon bands are labelled as follow, Acoustic E_g phonon modes (A(E_g)), Acoustic A_{1g} phonon mode (A(A_{1g})), Optical E_g phonon modes (O(E_g)), and Optical A_{1g} phonon mode (O(A_{1g})).

When we compare our results with the experimental data [72] for the cases without SO coupling, the disagreement is on the order of 10% for many bands and points. By contrast, the agreement is excellent if we add the SO coupling to the metallic case. In FIGs. 3.2 and 3.3, we report the full phonon band structures for the metallic case, with and without the SO coupling. The phonon band struc-

Table 3.1: Crystallographic parameters for the unit cell of Bi.

	Non-metallic without SO	Metallic		Experiment values
		without SO	with SO	
a_0 (Å)	4.6496	4.6525	4.6944	4.7236
α (deg)	57.57	57.48	57.57	57.35
z	0.47102	0.47108	0.46819	0.46814
a_{NN} (Å)	3.0385	3.0383	3.0505	3.0624
$\overline{BD}$ (Å)	5.4610	5.4684	5.4805	5.52252
$\overline{DH}$ (Å)	6.1328	6.1396	6.2250	6.27421

ture graphics for the non-metallic case without SO interaction is very similar to FIG. 3.2. The major effect due to SO coupling is a softening of all the phonon frequencies, this softening being very pronounced in absolute value in the case of the $O(A_{1g})$ branch (0.32 THz at the T point), as well as relatively in the case of the $A(E_g)$ branch (about 15 % at the T point).

In Fig. 3.4, we analyze in more detail the interplay between the direct effect of the SO coupling on the phonon frequencies, at fixed crystallographic parameters, and the indirect effect of the SO coupling, through modification of the crystallographic parameters. The phonon band structures for dotted (black) and the dot-dash (green) lines correspond to the (TcWoSO-PhWoSO) and (TcWoSO-PhWSO) cases respectively ; they have been computed for the same crystallographic parameters. This result clearly show that the inclusion of the SO interaction strongly affect the optical bands, as mentioned in last paragraph. The direct influence of the SO interaction is less pronounced for the acoustic branches, and bigger for the X-K-Γ line than for the Γ-T line (nearly negligible for the latter).

The dashed (blue) line correspond to the Ec-WSO case and the solid (black) line to the TcWSO-WSO case. The role of the crystallographic parameters is quite large for the acoustic branches : the indirect effect of the SO coupling is comparable to the direct effect for the X-K-Γ, and clearly predominent for the Γ-T line. For optical branches, the indirect effect of the SO coupling is much smaller than the direct effect.

The SO effect on the phonon band structure calls of course for further analysis.

Table 3.2: Phonon frequencies (THz) along the Γ-T direction. Experimental values from Ref. [72]. Theoretical values (metallic treatment) corresponding to three cases : theoretical crystallographic parameters and phonon values with SO coupling (TcWSO-PhWSO); experimental crystallographic parameters and phonon values with SO coupling (Ec-PhWSO); theoretical crystallographic parameters and phonon values without SO coupling (TcWoSO-PhWoSO).

	$A(E_g)$	$A(A_{1g})$	$O(E_g)$	$O(A_{1g})$		$A(E_g)$	$A(A_{1g})$	$O(E_g)$	$O(A_{1g})$
	Experimental Values					Theoretical cell, case with SO coupling (TcWSO-PhWSO)			
Γ			2.22	3.02				1.96	2.92
0.1			2.26	3.00				2.12	2.96
0.2			2.40	3.05				2.32	3.05
0.3			2.56	3.13				2.53	3.13
0.4	0.56	0.98	2.72	3.19		0.61	0.97	2.66	3.19
0.5	0.69	1.21	2.84	3.24		0.77	1.18	2.81	3.23
0.6	0.83	1.40	2.99	3.26		0.90	1.37	2.88	3.25
0.7	0.96	1.56	2.99	3.27		1.01	1.53	2.94	3.26
0.8	1.06	1.65	2.04	3.26		1.09	1.66	2.97	3.25
0.9	1.12	1.76	3.05	3.23		1.14	1.73	2.99	3.23
T	1.16	1.79	3.03	3.24		1.15	1.76	2.99	3.23
	Experimental cell with SO coupling (Ec-PhWSO)					Theoretical cell, case without SO coupling (TcWoSO-PhWoSO)			
Γ			1.89	2.87				2.16	3.12
0.1			2.05	2.91				2.37	3.16
0.2			2.26	3.00				2.60	3.28
0.3			2.46	3.08				2.80	3.38
0.4	0.58	0.93	2.59	3.14		0.70	1.02	2.87	3.43
0.5	0.74	1.13	2.74	3.18		0.91	1.26	3.06	3.49
0.6	0.86	1.32	2.82	3.21		1.02	1.44	3.13	3.52
0.7	0.97	1.48	2.88	3.21		1.17	1.63	3.20	3.54
0.8	1.05	1.60	2.91	3.21		1.25	1.76	3.20	3.53
0.9	1.09	1.67	2.93	3.19		1.30	1.84	3.23	3.53
T	1.10	1.69	2.93	3.19		1.34	1.89	3.23	3.55
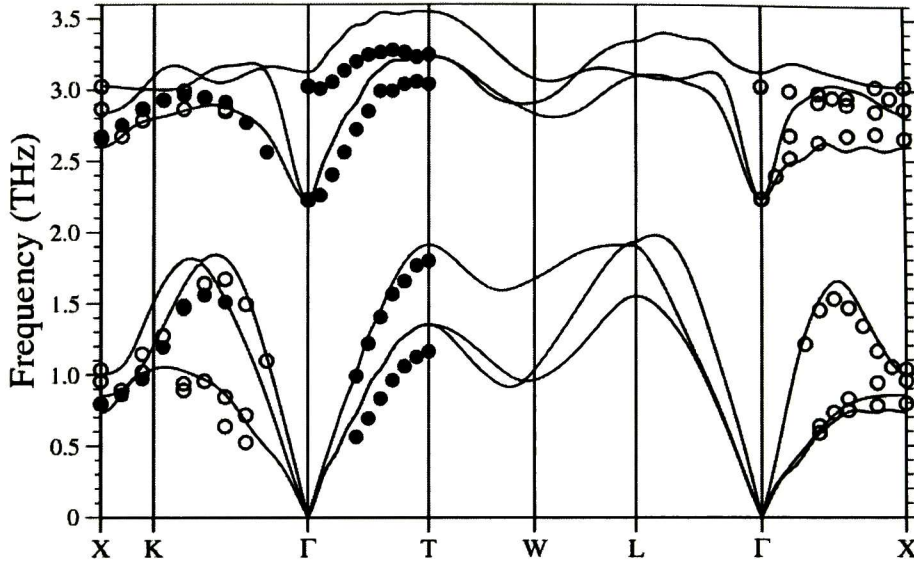
Figure 3.2: Phonon frequencies for Bi, metallic case, without SO interaction (TcWoSO-PhWoSO). Solid lines : theoretical results ; full dots : experimental data from Ref. [72] ; empty dots : experimental data from Ref. [73]. The lack of SO interaction is at the origin of most of the disagreement between theoretical and experimental values

3.4.3 Interatomic Force Constants

When one atom is displaced from its equilibrium position, it exerts a force on the other atoms. By reaction, a restoring force acts upon him. The proportionality coefficients between the displacement and the force between atoms are known as the interatomic force constants (IFCs). A Fourier transform of the IFCs, followed by proper inclusion of masses, leads to the dynamical matrix, whose eigenvalues are square of the phonon frequencies. Hence, the modification of the phonon band structure due to SO can be traced back to a change of IFCs.

Our analysis of the IFCs follows the one in Ref. [76, 77]. For each pair of atoms, the IFCs form a 3 by 3 matrix. Except for the interaction of the atom with itself, the 3 by 3 matrix can be analyzed by expressing it in the coordinate system in which the vector between the two atoms have been chosen as one of the axis (longitudinal direction), and the two other vectors leads to a diagonalization of the 2 by 2 remaining block (transverse directions). For the analysis of the on-site
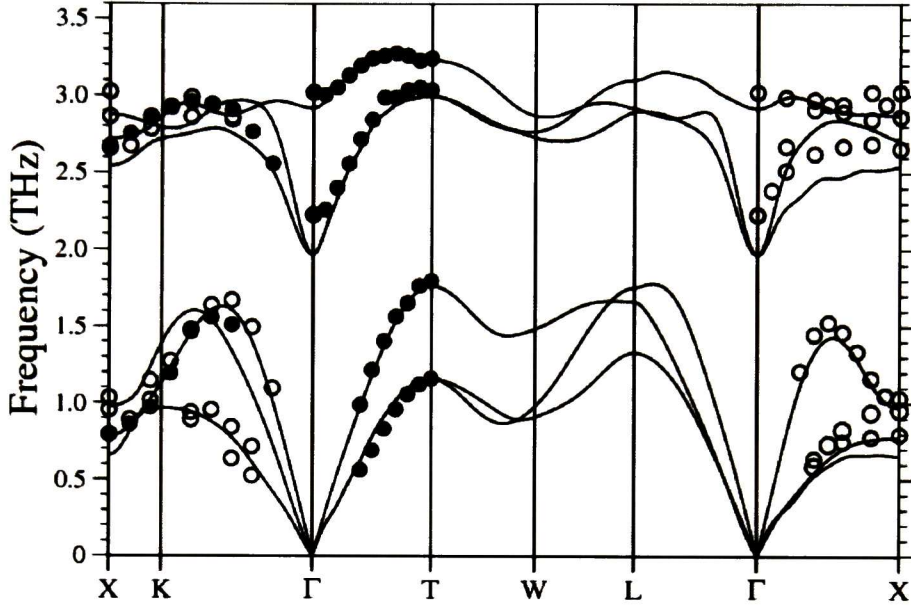
Figure 3.3: Phonon frequencies for Bi, metallic case, with SO interaction (TcWSO-PhWSO). Solid lines : theoretical results ; full dots : experimental data from Ref. [72] ; empty dots : experimental data from Ref. [73].

IFC, one can simply diagonalize the 3 by 3 matrix (that is symmetric).

The TABLE 3.3 shows our results for the longitudinal and transverse force constants, as well as the trace of the matrix (the sum of the longitudinal and transverse force constants). We do not report the longitudinal-transverse coupling values, although they are not negligible compared to transverse IFCs.

We consider the atom labeled as C_1 in FIG. 3.1 as the generic (referrer) atom. We then consider shells of more and more distant atoms, the interaction of atom C_1 with itself corresponding to shell 0. We distinguish whether the other atom lies inside the same bilayer as atom C_1 by the presence of an asterisk in TABLE 3.3.

The on-site IFCs, and the longitudinal IFCs between nearest-neighbors (shell 1 e.g. C_1-D) are one order of magnitude bigger than the other IFCs. The decrease with distance is quite marked, although the 9th shell IFCs (C_1-F_3) are particularly large. Actually, the atoms belonging to the 9th shell would have reduced coordinates (2 0 0) and equivalent if the structure were cubic. Beyond

57
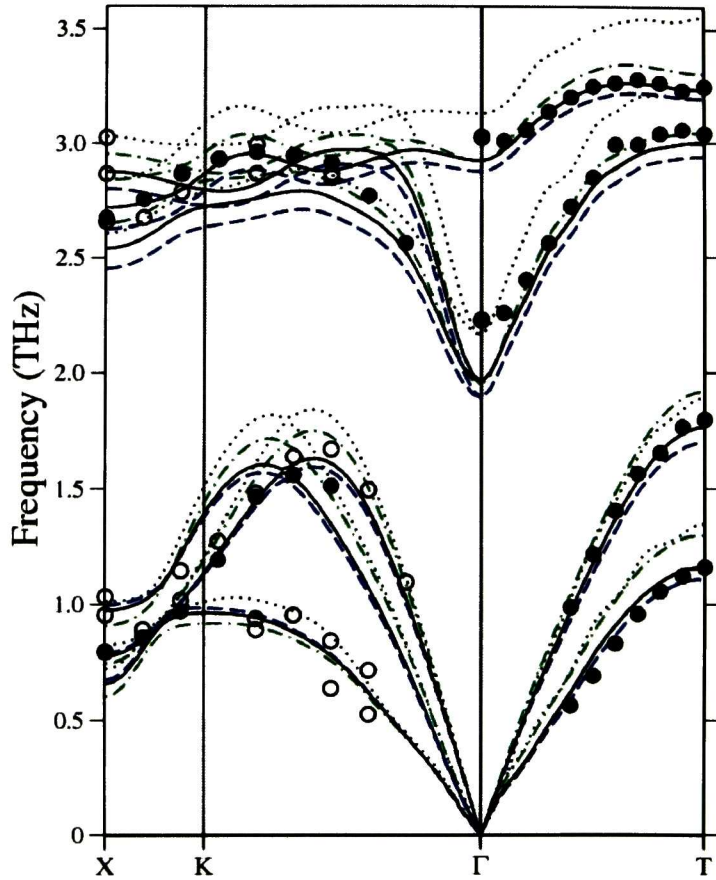
Figure 3.4: Phonon frequencies for Bi. Full dots : experimental data from Ref. [72] ; empty dots : experimental data from Ref. [73]. The lines correspond to theoretical results as follow. Dotted (black) line : theoretical cell parameters without SO coupling, phonons without SO coupling (TcWoSO-PhWoSO) ; dot-dashed (green) line : theoretical cell parameters without SO coupling, phonons with SO coupling (TcWoSO-PhWSO) ; solid (black) line : theoretical cell parameters with SO coupling, phonons with SO coupling (TcWSO-PhWSO) ; dash (blue) line : experimental cell parameter, phonons with SO interaction (Ec-PhWSO).

the ninth shell, the IFCs never exceed 1.5×10^{-3} Ha/Bohr^2, and go quickly to zero. Except for the longitudinal IFC of the first shell, the in-layer IFCs are not systematically bigger than the IFCs for pairs of atoms placed in different layers. Hence, with respect to its IFCs, Bi is *not* a quasi-two-dimensional material. Of course, the longitudinal first-shell IFCs, that are found only within the bilayers strongly influence the lattice dynamics.

We analyze now the effect of SO coupling. The biggest IFCs, i.e. the on-site IFCs and the first shell longitudinal IFCs, decrease both by about 15%. Among the other IFCs, some exhibit much bigger relative changes, and most of them change by more than 15%, although these noticeable changes only modulate the quite homogeneous softening brought by the biggest IFCs on the phonon band structure.

In order to shed some light on the modification of the on-site and shell 1 longitudinal IFCs, we also analyzed the Bi dimer. The technical details are quite similar to the crystalline case, except that we placed the system in a big cell. We found that the bond distance between a pair of Bi atoms is equal to 4.8607 Bohr for the case when the SO is not considered, while it is equal to 4.9166 Bohr when the SO coupling is taken into account. Going from the molecule to the solid decreases the nearest-neighbor distance significantly. The SO interaction causes a little increment in the bond length, in agreement with our previous result for solid Bi. The longitudinal IFC is equal to the on-site IFC for a dimer. In the case without SO, we obtain an on-site IFC value of 157.7×10^{-3} Ha/Bohr^2, while it drops to 130.5×10^{-3} Ha/Bohr^2 when the SO coupling is taken into account. Although the IFCs in the solid and the molecule are quite different, the effect of SO is qualitatively the same again.

Both the lengthening of the bond length increase and weakening of the IFCs can be rationalized, in a very qualitative way, by an analysis of the electronic structure of the molecule. Indeed, in the case without SO, the HOMO corresponds to twofold degenerate bonding π states, the LUMO corresponds to antibonding π^* states also twofold degenerate, separated by 2.2 eV only. Turning on the SO coupling leads to a mixing of bonding and antibonding orbitals, weakening the bond and increasing the bond length, on one hand. On the other hand, it diminishes the energy gap between the HOMO and the LUMO to a value of 1.3 eV, an effect that weakens the IFCs.

3.5 Conclusions

Our results reveals the role of SO coupling on the phonon band structure and interatomic force constants of Bi, whose treatment allows to get a very nice agreement with experiment. The SO interaction soften the phonon frequencies by about 10% for many bands and points when compared to experimental values, and it has a much smaller effect on the crystallographic parameters. For optical bands, the modifications are dominated by the direct SO interaction (crystallographic parameters play only a minor role), while the effect on the acoustic bands is largely mediated by the cell parameters also. A large fraction of the changes can be attributed to the modification of longitudinal force constants (and the accompanying on-site interatomic force constant), also present in the simple Bi diatomic molecule.

Table 3.3: Longitudinal ($\|$), and transverse ($\perp$) interatomic force constants (in units of 10^{-3} Ha/Bohr^2), for different shells of atoms. The distances are given in atomic "Bohr" units. We indicate, in parenthesis, the number of the shell if the structure were cubic. Several shells in the rhombohedral structure combine into one shell of the cubic structure. The asterisk indicate shells of atoms that are in the same bilayer as the referrer atom (see text).

Shell	Distance	$\|$	$\perp$	$\perp$	Trace
Without SO (TcWoSO-PhWoSO)					
0*(0)	0.0000	47.50	48.59	48.21	144.31
1*(1)	5.7417	-32.48	-2.77	-2.65	-37.90
2 (1)	6.4993	-2.72	1.07	0.08	-0.83
3*(2)	8.4562	-2.69	1.44	0.87	-0.39
4 (2)	8.7921	-1.19	0.00	1.13	-0.06
5*(3)	10.221	0.05	-0.09	0.12	0.07
6 (3)	10.333	0.14	-0.05	-0.05	0.05
7 (3)	10.665	-0.08	0.14	0.02	0.08
8 (3)	11.602	-0.07	-0.08	-0.08	-0.22
9 (4)	12.198	-4.24	-0.57	-0.71	-5.52
With SO (TcWSO-PhWSO)					
0*(0)	0.0000	41.67	42.46	42.21	126.34
1*(1)	5.7646	-29.13	-2.27	-1.89	-33.28
2 (1)	6.6033	-2.37	0.78	0.75	-0.84
3*(2)	8.5436	-2.68	1.83	0.15	-0.70
4 (2)	8.8712	-1.20	0.02	0.85	-0.33
5*(3)	10.306	0.04	-0.1	0.19	0.14
6 (3)	10.356	0.08	-0.16	-0.16	-0.25
7 (3)	10.798	0.00	0.10	0.01	0.11
8 (3)	11.763	-0.10	-0.13	-0.13	-0.36
9 (4)	12.316	-3.03	-0.44	-0.72	-4.19

Chapter 4

Thermodynamical properties for Bismuth

4.1 Effect of the Spin-Orbit Interaction on the Thermodynamic Properties of Crystals: Specific Heat of Bismuth

We discuss measurements and ab initio calculations of the specific heat for crystalline bismuth, strictly speaking, a semimetal but in the temperature region accessible to us ($T > 2$K) acting as a semiconductor. We extend experimental data available in the literature and notice that the ab initio calculations without spin-orbit interaction exhibit a maximum at ~ 8K, about 20% lower than the measured one. Inclusion of spin-orbit interaction decreases the discrepancy markedly: the maximum of $C(T)$ is now only 7% larger than the measured one. Exact agreement is obtained if the strength of the spin-orbit Hamiltonian is reduced by a factor of ~ 0.9. We also discuss the dependence of the lattice parameter and the cohesive energy on spin-orbit interaction.

4.2 Introduction

In the past few years, a number of investigations on the dependence of the specific heat of semiconductors and insulators on temperature and isotopic masses have been carried out. These works involved careful low temperature experiments (for elemental crystals, see Refs. [78, 79], for binaries, see Refs. [80]

and references therein) and elaborate *ab initio* calculations based on electronic band structures computed in the framework of the local density approximation (LDA). Recent work involving binary lead chalcogenides with different isotopic compositions [PbS (Ref. [81]), PbSe (Ref. [82])] yields a low temperature maximum in the quantity $C(T)/T^3$ (at $\sim 12K$) [81, 82] about 25% lower than the measured one. Correspondingly, the calculated phonon dispersion relations are on the average 10% higher than those determined with inelastic neutron scattering (INS) [83]. The higher phonon frequencies qualitatively explain the lower specific heats obtained from the calculations.

When trying to ascertain whether the *harder* phonon frequencies (and lower specific heats) calculated for PbS and PbSe were due to the lack of spin-orbit (SO) coupling in the *ab initio* electronic structure, some difficulties arose. These involved not only the extended computational time but also divergences in the dispersion relations of the optical phonons for $\mathbf{q} \rightarrow 0$. The latter may be related to the strongly ionic, nearly ferroelectric character of these compounds.

To our knowledge the computation of the $\mathbf{q} \rightarrow 0$ divergences when the spin-orbit coupling is present has not yet been implemented in existing first-principles codes. By contrast, for metals, there is no such divergence, which makes possible the direct computation of phonon band structure and thermodynamical properties based on density-functional perturbation theory (Ref. [5, 68, 86]), including spin-orbit, as implemented in the *ABINIT* software [70]. Thus, we performed measurements and calculations for crystalline bismuth, which is free of the ionic divergences present in the lead chalcogenides.

With this work we demonstrate that inclusion of SO coupling, in fact, considerably reduces the discrepancies between experimental heat capacity data and **ab initio** results. In addition, we also discuss the dependence of the rhombohedral lattice parameter a_0 and the cohesive energy E_c on the magnitude of the SO coupling. Bismuth is a semimetal closely related to the lead chalcogenides: it has 10 valence electrons per primitive cell and a rhombohedral structure which can be derived from that of PbS by making both atoms equal and applying a Peierls-like distortion to the PbS cube, involving an elongation of one of its [111] axes [87]. The distortion converts the simple cubic structure of bismuth, with one atom per primitive cell, into a rhombohedral one with two atoms per primitive cell (two sublattices). This structure is characterized by three parameters: the bond length a_0, the rhombohedral angle, and a shift between the two sublattices [67, 88]. These parameters were determined by energy minimization using the *ABINIT* code. The results obtained for these parameters in Refs. [67, 88] with and without SO coupling differ by less than 1%.

4.3   ab initio calculations

The phonon dispersion relations were calculated with *ABINIT* in Ref. [67] with
SO coupling whereas in Ref. [88] calculations with and without SO coupling
were performed. With SO coupling, excellent agreement with experimental re-
sults (Ref. [72]) was obtained whereas without it, discrepancies of the order of
10% were found, the calculated bands lying higher in frequency than the mea-
sured ones. Similar results were found for PbS (Ref. [81]) and PbSe (Ref. [82])
without SO coupling. In view of these results, we proceeded to calculate the spe-
cific heat $C(T)$ of bismuth. In order to complete the available experimental data
(carried out on polycrystalline samples) [89–93] we also performed measure-
ments on high purity (99.9999%, Preussag Pure Metals) single crystals. Recent
data collected by various earlier authors and our own data (our experimental
technique is described in Refs. [78–81]) are compiled in Fig. 4.1, together with
the results of our ab initio calculations performed with and without spin-orbit
coupling.

4.4   Results and discussion

The hitherto available experimental points were measured on polycrystalline
samples. They are rather widely spaced in temperature, with the exception of
Keesoms below 4 K (Ref. [90, 94]). We have therefore performed measure-
ments of $C_p(T)$ on single crystals for T between 1.8 and 100 K with the mea-
suring temperatures spaced by $\sim$0.1 K up to 50 K and 0.5 K steps above 50
K. The maximum of $C(T)/T^3$ takes place at 7.5 K. According to Ref. [82] it
should be found at $\sim T_{TA}/6$, where $T_{TA} \sim 42$ K is an Einstein oscillator fre-
quency which can be read off the phonon density of states [67]. The temperature
of the maximum in Fig. 4.1 is found to be 7.5 K, fairly close to $T_{TA}/6 = 7K$.

Although the typical carrier concentrations of the PbS samples are between
10^{18} and 10^{19} cm^3 [81], no evidence of a free carrier contribution to the specific
heat was found, except possibly below 2 K [90]. Thus, the measured specific
heat represents the contribution of the lattice vibrations vs temperature, obtained
at constant pressure C_p . Most lattice dynamical calculations, such as those of
Elcombe, represent the specific heat measured at constant volume C_v [83]. The
difference between C_p and C_v is given by [98],

$$C_p(T) - C_v(T) = \alpha_v^2(T)BV_{mol}T, \tag{4.1}$$

65
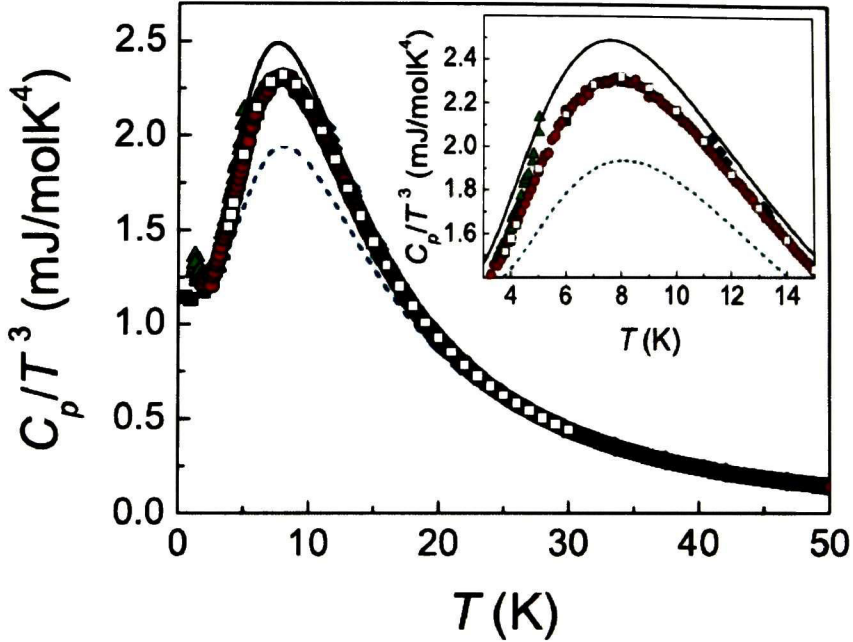
Figure 4.1: Heat capacity of a Bi single crystal, purity 99.9999%. (Red filled) circles as measured in this work compared with literature data obtained on poly-crystalline samples. (Green) ▲ (Ref. [90]); (blue) ♦ (Ref. [90]); □ (Ref. [92]); (black) ■ (Ref. [93]). (Black) solid line : *ABINIT* results with spin-orbit coupling included; (blue) dashed line: *ABINIT* calculation without spin-orbit coupling.

where α_v is the temperature dependent thermal expansion coefficient, B the isothermal bulk modulus using the notation of Ref. [84], and V_{mol} the molar volume. According to Eq. (4.1), the difference $C_p - C_v$ increases with increasing T. Replacing standard values of $\alpha_v(T)$, B, and V_{mol} found in the literature [85], we obtain from Eq. (4.1) the difference $C_p - C_v = 0.18$ J/mol K at the highest temperature used in our measurements (~ 280 K). This difference is smaller than typical error bars in our measurements and will be neglected here. We shall therefore denote the specific heat, either theoretical or experimental, by C_p [81].

Our measurements place the maximum value of C/T^3 at 2.32 ± 0.03 mJ/molK^4.

The value calculated without SO splitting lies at 1.940 mJ/mol K^4 whereas with SO coupling one finds 2.500 mJ/mol K^4 . Hence, the results of the calculation without SO coupling lie 20% below the experimental data; those with SO coupling lie only 7% above. Not only is the difference between measured and calculated values of C/T^3 3 times smaller when SO interaction is taken into account, but the agreement with SO coupling above 12 K lies within the experimental error, whereas without SO coupling a considerable difference is found.

This improvement illustrates the importance of SO interaction for the calculations of thermodynamic properties starting from ab initio electronic band structures for systems containing heavy atoms and confirms our conjecture that similar discrepancies between calculated and measured values of C/T^3 found for PbS and PbSe [81, 82] must be due to the lack of SO coupling in the electronic structure calculations. These results suggest performing calculations and measurements for antimony (also a semimetal with the same crystal structure as Bi) which has a considerably smaller atomic SO coupling than bismuth (0.84 versus 1.7 eV).

The results for Sb are shown in Chapter 5, but here we have pursued yet another avenue: we have multiplied the spin-orbit coupling Hamiltonian by a factor $0 < \lambda < 1$ and repeated the full *ab initio* calculations of $C(T)$ for several values of λ. The results obtained for bismuth are shown in Fig. 4.2.

This figure reveals the strongly supralinear dependence of the SO effect on C/T^3 which can be fitted with the expression

$$C/T^3 = c_0[1 + c_2\lambda^2(1 + c_4\lambda^2)] \tag{4.2}$$

with $c_0 = 1.942(2)$ mJ/mol K^4 , $c_2 = 0.116(7)$, and $c_4 = 1.46(13)$.

The fit is displayed in Fig 4.3(a). For $\lambda = 1$ the fourth order term surpasses the quadratic term. Exact agreement between the measured and the calculated values of C/T^3 is obtained if one reduces the SOC coupling by a factor $\lambda = 0.9$.

It is expected that other mechanical and thermodynamic properties of Bi should depend on the SO coupling as well, i.e., on the value of λ. The simplest of them is probably the rhombohedral lattice parameter a_0 . It is shown in Fig. 4.3(b) calculated for the same values of λ as $C(T)$ and fitted with and expression similar to Eq. 4.2 with $a_0(\lambda = 0) \equiv c_0 = 4.6529(7)$Å, $a_2 = 0.0069(9)$, and $a_4 = 0.29(16)$. The values of the fit parameters c_i indicate that there is no simple relationship between the effect of SO splitting on $C(T)$ and the lattice parameter $a_0(\lambda)$. The effect of spin-orbit interaction on $C(T)$, as described by c_2 and c_4 , is much larger than that on the lattice parameter $a_0(\lambda)$. For $\lambda = 1$, however, the calculated value for a_0 (4.694Å) is also much closer to the experimental one
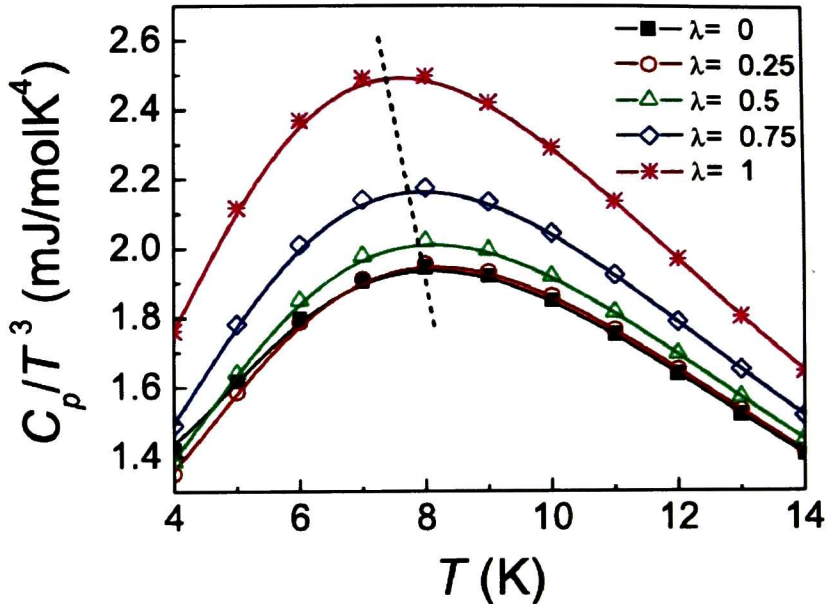
Figure 4.2: Calculated heat capacities of Bi with varying magnitude of the SO coupling as indicated in the inset. Note that the maximum shifts to lower temperatures (inclined dashed line) with increasing SO coupling, as it corresponds to decreasing phonon frequencies (see text).

(4.720Å) than that obtained for $\lambda = 0$ (4.652Å).

We have also calculated the cohesive energy E_c for several values of λ. E_c was obtained as the difference between the calculated total energy for the free atom and that for the solid, both calculated with the LDA approximation for exchange and correlation using *ABINIT* and spinorial, spin-polarized wave functions. This procedure leads to the λ dependence of E_c shown in Fig. 4.3(c). $E_c(\lambda)$ can also be fitted with Eq. (4.2), leading to the parameters $c_0 = 3.236$ eV/atom, $c_2 = -0.161(4)$, and $c_4 = 0.045(26)$. Hence, like for the other thermodynamic properties investigated, no linear term in λ appears in E_c. The lack of linear terms in λ in the thermodynamic properties contrasts with the results of the calculations for individual one-electron states [61]. This leads to the conclusion that upon integration of all one-electron states the linear terms cancel and only terms of second or higher order in λ remain.

Note that the inclusion of spin-orbit coupling considerably improves the agreement of calculated and measured of E_c. The calculated value $E_c(\lambda = 1) = 2.76$ eV is remarkably close to the measured one ($E_c = 2.16$ eV/atom (Ref. [6]), especially when one considers that it is obtained as the difference of two large energies, of the order of 150 eV/atom.

4.5 Conclusions

In conclusion, we have investigated the effect of SO interaction on three thermodynamic properties, $C(T)$, a_0 , and E_c , of a solid consisting of the heavy element bismuth. Such effects, apparently rather substantial for a first principles calculation of the physical properties, have not received much consideration in the literature so far. For a discussion of other similar phenomena, see Refs. [95, 96].

The fit with Eq. 4.2 implicitly implies the absence of cubic terms in λ. In order to check this assumption, we have calculated the quantities in Fig. 4.3 for negative values of λ and found, e.g., that $a_0(\lambda = +1)$ differs slightly from $a_0(\lambda = -1)$. A fit with the equation $a_0(\lambda) = a_0(0)[1 + c_2\lambda^2(1 + c_3\lambda)]$ yields $a_0(0) = 4.6528(5)$ Å $c_2 = 0.0064(2)$, and $c_3 = 0.41(2)$ indicating that cubic term play an important role.
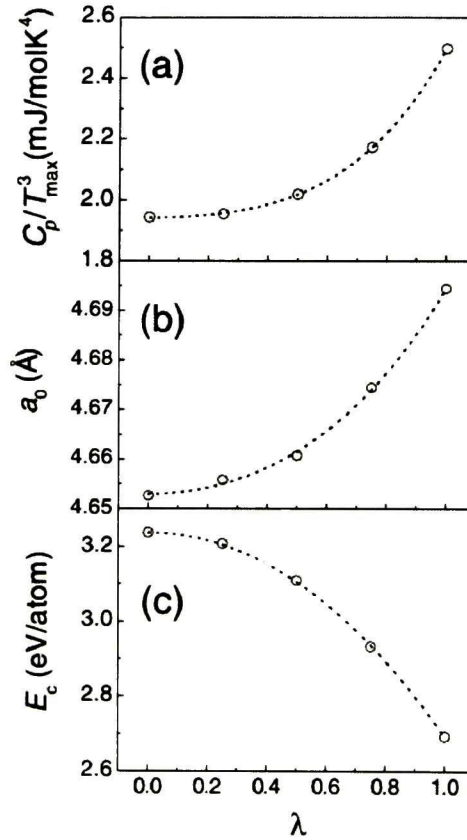
Figure 4.3: (a) Maxima of the quantity $C_p(T_{max})/T_{max}$ vs spin-orbit coupling parameter λ. (b) Energy minimized lattice parameter a_0 vs spin-orbit coupling parameter λ. (c) Cohesive energy of bismuth vs λ, calculated as discussed in the text. The circles ($\bigcirc$) represent our calculations, the dashed lines fits with Eq. (4.2) which lead to the parameters given in the text.

Chapter 5

Thermodynamical properties for Antimony

5.1 Specific heat of Sb: Isotopic and spin-orbit effects from measurements and ab initio calculations

We report measurements of the specific heat C of antimony crystals in the 2 - 50 K temperature range for several isotopic compositions and *ab initio* calculations of the specific heat as a function of temperature. The contribution of spin-orbit interaction and the dependence of C on isotopic mass are discussed and compared with previous observations reported for semiconductors and group VA semimetals. We also discuss the effect of spin-orbit interaction on the trigonal lattice parameter and the cohesive energy.

5.2 Introduction

In the last years, a number of publications have reported the temperature dependence of the specific heat C in monatomic [78, 79, 97] and binary [80, 81, 98] semiconductors as a function of the isotopic mass of its constituent atoms. Some general trends were observed in all investigated materials, namely, (i) a peak appears at low temperature T in the plot of C/T^3 vs T, (ii) this peak is higher for larger isotopic masses M, and (iii) in monatomic crystals, there is a unique relation between the temperature dependence of $d\ln(C/T^3)/d\ln M$ and that of

71

$d\ln(C/T^3)/d\ln T$. This relation carries over to binary semiconductors if one considers the sum of the logarithmic derivatives with respect to the isotopic masses. These trends were reproduced by first-principles calculations based on the linear response method and density functional perturbation theory. Contrary to this, little information is available on the thermodynamic properties of semimetals, in particular, the specific heat, where both electronic and lattice degrees of freedom play a role. With the exception of phosphorus, the group of the VA elements exhibit the A7 rhombohedral structure space group $R\bar{3}m$, No. 166 in the International Crystallographic Tables . This structure is generated by applying a deformation along the threefold axis to an fcc lattice plus a relative displacement of atoms, which results into a primitive cell with two atoms [99]. Among these elements, antimony is known for the strongly anharmonic behavior of the crystal lattice, as revealed by the Raman-Brillouin scattering, in particular, under pressure [100, 101]. The anharmonicity, together with the semimetallic character of their electronic structure and, for heavier elements, the increasing importance of spin-orbit interaction, has hindered so far an accurate investigation of their thermodynamic and lattice dynamical properties by means of *ab initio* calculations. For example, only very recently, spin-orbit interaction has been taken into account for calculations of these properties in bismuth [67, 88, 102]. From the experimental point of view, there are only a few works going back to the 1960s, dealing with the specific heat of arsenic [103–105], antimony [106–108], and bismuth [109, 110]. Due to the limitations of the experimental equipment, the reported data show considerable scattering in the 5 - 20 K temperature region. It is precisely in this temperature range where the most interesting effects occur, i.e., the described trends seen for semiconductors and the deviation from the Debye behavior, as well as the presence of both electronic and lattice contributions.

In this chapter, we report specific heat measurements of antimony crystals in the 2 - 50 K temperature range both for natural samples as well as isotopically enriched ^{121}Sb and ^{123}Sb. The experimental data are compared with *ab initio* simulations of the lattice dynamics and the specific heat. These simulations were performed with a relativistic pseudopotential Hamiltonian that includes the spin-orbit interaction. The effect of spin-orbit interaction is expected to be important although not as large as recently reported for bismuth [102].

Concerning the dependence on isotope mass, we found analogous behavior as that for monatomic semiconductors. Additionally, we have calculated the effect of spin-orbit interaction on the trigonal lattice parameter and the cohesive energy. Like in the case of bismuth [102], we found the effects of spin-orbit

interaction to be approximately quadratic on the spin-orbit coupling parameter, a linear term being absent.

5.3 Experimental Method

Natural samples of antimony were obtained from the Preussag Pure Metals (Langelsheim, Germany). They consisted of small single crystals of a purity of 99.9999 %. Isotopically enriched ^{121}Sb and ^{123}Sb with 99% isotope abundance in either case were purchased from the Oak Ridge National Laboratory. According to their assay, the chemical purity of both enriched isotopes was better than 5×10^{-4}. They appeared to be, upon microscope observation, single crystals of about 2 mm^3 size. Pieces of the three isotope modifications, weighing about 30 mg, were used as purchased for the specific heat measurements, without any additional treatment. For details about the calorimeter and the experimental procedure, see Refs. [78, 79, 98] as well as Appendix C. The measurements were performed under vacuum, i.e., at constant pressure. We do not distinguish here between the specific heat obtained at constant volume or constant zero pressure since, in the temperature region under consideration, they coincide within error [81, 98] as explained below.

Most lattice dynamical calculations, such as those of Elcombe, represent the specific heat measured at constant volume C_v [83]. The difference between C_p and C_v is given by [98],

$$C_p(T) - C_v(T) = \alpha_v^2(T) B V_{mol} T, \qquad (5.1)$$

where α_v is the temperature dependent thermal expansion coefficient, B the isothermal bulk modulus using the notation of Ref. [84], and V_{mol} the molar volume. According to Eq. (5.1), the difference $C_p - C_v$ increases with increasing T. Replacing standard values of $\alpha_v(T)$, B, and V_{mol} found in the literature [85], we obtain from Eq. 5.1 the difference $C_p - C_v = 0.18$ J/mol K at the highest temperature used in our measurements (~ 280 K). This difference is smaller than typical error bars in our measurements and will be neglected here. We shall therefore denote the specific heat, either theoretical or experimental, by C_p [81].

5.4 *ab inition* Calculations

First-principles methods have proved to be essential to identify the phonon modes responsible for the temperature dependence of the specific heat in semiconductors. In this work, we report *ab initio* calculations of the specific heat of antimony and the lattice dynamics obtained with the *ABINIT* software package [68, 70, 111].

The electronic structure of antimony in the $R\bar{3}m$ phase was calculated using the Hartwigsen-Goedecker-Hutter pseudopotentials which are expressed as norm-conserving separable dual space Gaussians and generated on the basis of a fully relativistic all-electron calculation [29]. To this aim, a grid of $12 \times 12 \times 12$ **k**-points in the Brillouin zone was used for the integration required for the determination of the local charge density. The local density approximation to the exchange and correlation energy was employed [50].

The dynamical matrices corresponding to a grid of $12 \times 12 \times 12$**q** points were calculated within the framework of density functional perturbation theory and the linear response method. These matrices were then interpolated to obtain, by integration, the lattice contribution to the specific heat at constant volume [34, 68, 111]. Details of the procedure and equations to calculate this contribution have been reported elsewhere[80].

The implementation of the spin-orbit term in *ABINIT* follows the same lines as in Ref. [48], where the spin-orbit term in the Hamiltonian is applied only into the Kleinmann-Bylander type of nonlocal operator. For the electronic calculations, the spin-orbit Hamiltonian was multiplied by a parameter λ. Thus, $\lambda = 0$ corresponded to neglecting the spin-orbit coupling, whereas for $\lambda = +1$, the full spin-orbit coupling was applied. We also performed calculations for $\lambda = 0.5$ and $\lambda = -1$, so as to confirm the quadratic dependence of thermodynamic properties on λ proposed in Ref. [102].

5.5 Discussion

Figure 5.1 displays the temperature dependence of C/T^3 measured for natural antimony (open squares) together with data previously reported in Ref. [106] (open circles) . Our measurements provide a much clearer description of the behavior at temperatures lower than 15 K, whereas at higher temperatures, both data sets are basically indistinguishable.

In a semimetal, the low temperature limit of the specific heat can be described by the equation,
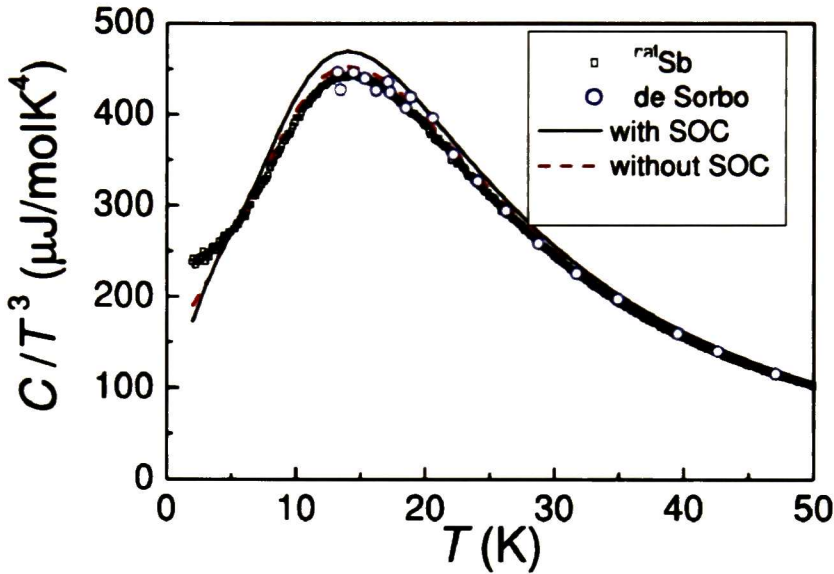
Figure 5.1: Temperature dependence of the specific heat of natural antimony. The experimental data (open squares) are compared with data from the literature Ref. [106] (solid circles) and with *ab initio* calculations with (black, solid) and without (red, dashed) spin-orbit interactions.

$$C = \gamma T + \beta T^3 + \alpha T^2, \tag{5.2}$$

where the linear term represents the electronic contribution, the cubic term corresponds to the Debye behavior of the crystal lattice, and the T^2 term describes the interaction of the nuclear quadrupole moment with the electric field gradient of the electrons and the lattice. The latter term is negligible within our temperature range, but it may become appreciable for $T < 1$ K. The upward bending at low temperatures (cf. Fig. 5.1) is due to the electronic contribution (γ) to the specific heat [107]. A fit of the low temperature heat capacities with Eq. (5.2) gives $\gamma = 0.13(4)$ mJ mol^{-1} K^{-2} and $\beta = 0.234(2)$ mJ mol^{-1} K^{-4} ($\alpha = 0$). These values are nearly independent of the isotope composition and in good agreement with those reported in Refs. [104] and [107].

The peak in Fig. 5.1, located at 14 K, evidences the deviation from the Debye behavior that is known to occur at low temperatures. Within the Einstein

75

model, this peak should correspond to a phonon frequency of 7 meV [81], which coincides with the first maximum of the calculated phonon density of states, i.e., it corresponds to transverse acoustic modes [112].

Figure 5.1 also displays the calculated temperature dependence of the specific heat with (black, solid) and without (red, dashed) the spin-orbit interaction. Both calculations reproduce well the temperature dependence and the peak position in the experimental data. The spin-orbit interaction produces an enhancement of the peak of C/T^3 by $\sim 4\%$. Very recently, the contribution of spin-orbit interaction to the specific heat of bismuth was reported to be quadratic in at low values of λ [102]. For $0.5 < \lambda < 1$, a cubic term becomes important, but no linear term in λ is observed. Considering that the spin-orbit splitting of bismuth (1.7 eV) is 2.42 times that of antimony (0.7 eV) [113], if we take the value for $\lambda = 1 / 2.42 = 0.41$ in Eq. (5.2) of Ref. [102], we expect an increase of 2.4% for the peak of C/T^3 for antimony, in qualitative agreement with our direct calculations. The difference between 2.4% and 4% might be related to the role of cubic terms in λ, neglected in Eq. (1) of Ref. [102]. Both in bismuth [102] and antimony, there is a 5% discrepancy between the calculations (including spin-orbit interaction) and experimental results. This discrepancy might be related to the intrinsic inaccuracy of local density approximation phonon dispersions, as compared to the experimental values.

Figure 5.2 displays the dependence of the peak of C/T^3 on isotope mass. For the sake of comparison, the linear temperature term has been subtracted from the experimental data, since it is not taken into account in the calculations. The curves of Fig. 5.2 show an increase of the peak with increasing isotope mass, both for the experimental and calculated data. This trend, already reported for semiconductors in previous works,[78, 80, 81, 98] seems also to be obeyed by semimetals. The isotope shift of the peak between ^{121}Sb and ^{123}Sb amounts to 12 μJ mol^{-1} K^{-4} and agrees reasonably well with the experimental shift, 14.2 μJ mol^{-1} K^{-4}. The calculated curve corresponding to antimony with natural isotope composition is slightly closer to that of ^{121}Sb due to the closer masses. In the case of experimental data, we found that this rather subtle effect depends somewhat on the sample details.

Figure 5.3 displays full circles the logarithmic derivative of C/T^3 with respect to the isotope mass corresponding to the experimental data obtained after subtraction of the electronic contribution [γ term in Eq. 5.2]. This derivative has been reported to be linked to the logarithmic derivative with respect to temperature in diamond, silicon, and germanium by [97],
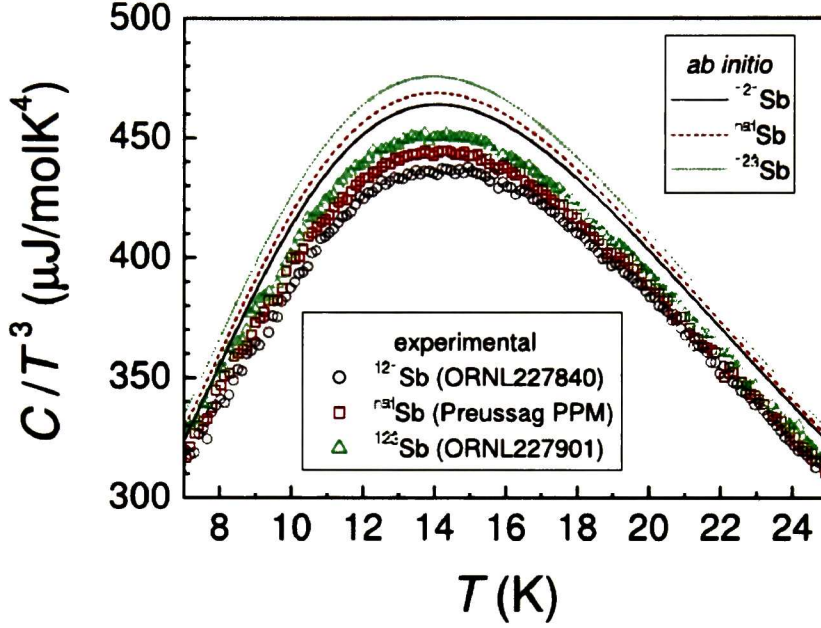
Figure 5.2: Same as Fig. 5.1 for different isotope compositions. The calculations were performed in all cases including spin-orbit interactions ($\lambda = +1$).

$$\frac{d\ln(C/T^3)}{d\ln M} = \frac{1}{2}\left[3 + \frac{d\ln(C/T^3)}{d\ln T}\right]. \tag{5.3}$$

We show in Fig. 5.3 the left- and right-hand sides (rhs) of Eq. (5.3) obtained from the experimental data with full (red) and open (black) circles, respectively, and the rhs of Eq. (5.3) calculated from the *ab initio* data for $\lambda = +1$ solid line. The agreement between both experimental data sets, as well as the agreement with the *ab initio* data, is excellent. The good agreement between both sets allows us to verify the validity of this equation for semimetals. The peak at 10 K is followed by two different slopes at higher temperatures, the crossover point being at ~ 25K. The associated phonon frequency is 11.5 meV, calculated again by multiplying the crossover temperature by a factor of 6 [81]. This frequency corresponds to the threshold between acoustic and optic phonons, as shown in the phonon dispersion relations obtained by inelastic neutron scattering experiments [112] and confirmed by our calculations [114]. Hence, we attribute the
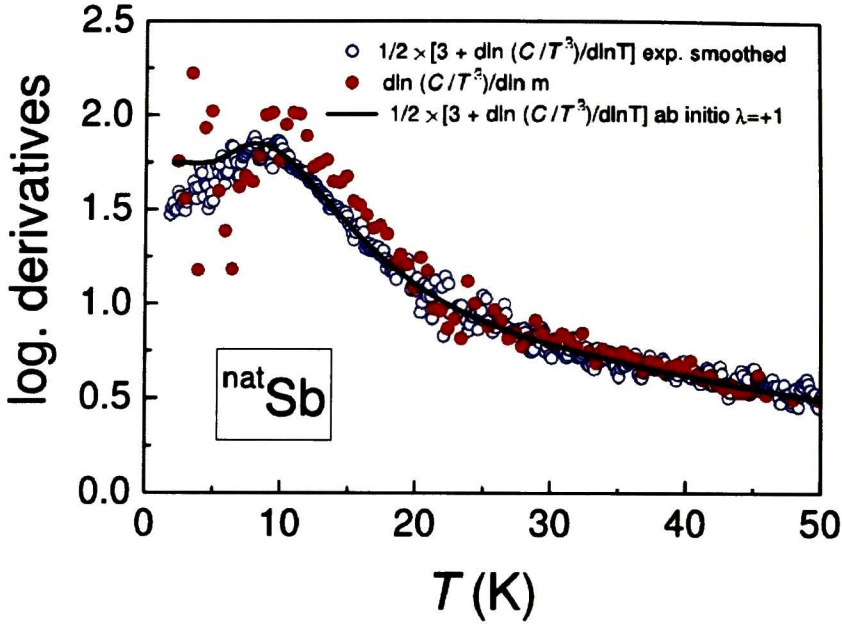
Figure 5.3: Logarithmic derivative with respect to the isotope mass, $d\ln(C/T^3)/d\ln M$ (solid red circles) and rhs of Eq. (5.3) (open black circles), corresponding to the experimental data. The solid line displays the rhs of Eq. (5.3) obtained from the calculations.

change in slope to the activation of optic phonons at higher temperatures.

In recent works on bismuth [67, 102], a significant contribution of spin-orbit interaction to vibrational properties such as phonon dispersion relations and specific heat has been found. The relevance of these effects can be evaluated by performing *ab initio* simulations of the properties of interest as a function of the magnitude of the spin-orbit interaction, governed by the coupling parameter λ. Figure 5.4 displays the change in the trigonal lattice constant a_0 and the cohesive energy E_{coh} as a function of λ. The calculated data show a quasiparabolic dependence on λ, with a small but nevertheless significant contribution of a cubic term. The experimental value of $E_{coh} = 2.7$ eV compares well with the calculated value for $\lambda = +1$, i.e., 3.37 eV. A similar agreement was reported in Ref. [102] for bismuth. The expansion of the spin-orbit Hamiltonian in λ using perturbation theory contains only quadratic and higher order terms in λ, since linear

78

terms in λ would imply a splitting between z components of the spin upon the spin-orbit interaction, a splitting that can only happen in the presence of a magnetic field. Therefore, no linear term in the dependence of both a_0 and E_{coh} on λ is expected. Note that the square root of the ratio of the coefficients corresponding to the quadratic term in λ for the fits of a_0 of bismuth [102] and antimony, which amounts to 2.75, is rather similar to that of the spin-orbit splittings, i.e., 1.7 / 0.7 = 2.42 [113]. The difference between 2.75 and 2.42 may be due to the fact that the corresponding energy denominators are smaller in Bi than in Sb. A similar comparison can be affected for the cubic root of the ratio of the cubic terms which for a_0 turns out to be 2.8, close to the ratio of spin-orbit splittings. This relation, which also holds for the dependence of the peak C/T^3 on λ, implies a simple scaling of the effects of spin-orbit interaction on the vibrational properties.

Figure 5.5 displays the change of the specific heat with λ as a function of temperature. Two main effects are observed, namely, a larger value of the peak C/T^3 with increasing strength of the spin-orbit interaction and a crossing of the curves corresponding to $\lambda = +1$ and $\lambda = -1$. The observed crossing suggests a change in the slope of the phonon dispersion corresponding to low frequency acoustic modes, since a shift of the peak to lower temperatures is caused by an increase of the lowest phonon frequencies. The phonon dispersion data reported for bismuth in Table 5.6 of Ref. [88] manifest a change of slope of transverse acoustic $[A(E_g)]$ modes along the $\Gamma - T$ direction between $\lambda = 0$ and $\lambda = 1$, i.e., an indication of a crossing of the dispersion relations also for bismuth (unfortunately, no calculations for $\lambda = -1$ were reported in Ref. [88]. Table 5.6 displays the acoustic phonon frequencies of antimony along the $\Gamma - T$ direction calculated for $\lambda = 0$, 1, and -1. A higher sound speed is observed in the case of $A(E_g)$ modes for $\lambda = 1$ and -1, as compared to that obtained without spin-orbit interaction. On the contrary, the same phonon branch shows higher frequencies for $\lambda = 0$ close to the zone boundary, thus evidencing a crossing of the $A(E_g)$ bands similar to that just mentoned for Bi. Table 5.6 also displays a crossing of the $\lambda = +1$ and the $\lambda = -1$ bands.

5.6 Conclusions

In conclusion, we have reported measurements of the dependence of the specific heat of antimony on the isotope mass as a function temperature. The experimental data have been analyzed with the aid of first-principles calculations of

the lattice dynamics and its contribution to the specific heat. The specific heat of antimony shows a similar behavior with changing isotope mass as observed in semiconductors, namely, a peak of C/T^3 vs T whose strength increases with the isotope mass, and a relation between the logarithmic derivatives with respect to isotope mass and temperature. Moreover, the *ab initio* calculations allowed us to evaluate the contribution of the spin-orbit interaction to the specific heat, the lattice parameter, and the cohesive energy. These three physical quantities depend nearly quadratically on the spin-orbit coupling parameter λ, with a minor contribution of a cubic term. The quadratic dependence is proportional to the square root of the spin-orbit splitting, as evidenced in the comparison of results for bismuth and antimony.
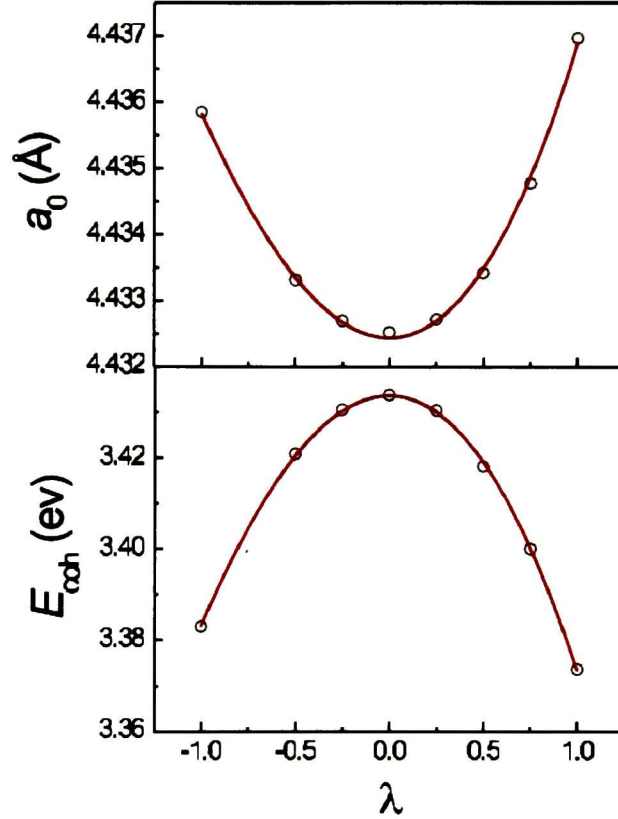
Figure 5.4: Dependence of the lattice parameter a_0 and the cohesive energy E_{coh} on the strength of the spin-orbit interaction. The solid line displays a fit with a polynomial of third order, $y(\lambda) = y_0(0)[1+c_2\lambda^2(1+c_3\lambda)]$ $(y = a_0, E_{coh})$, with $a_0 = 4.43244(4)$, $c_2 = 0.00089(2)$, and $c_3 = 0.136(13)$ and $E_0 = 3.4337(3)$ Å, $c_2 = 0.0162(2)$, and $c_3 = 0.088(7)$ for the lattice parameter a_0 and the cohesive energy E_{coh}, respectively (see Discussion in the text).
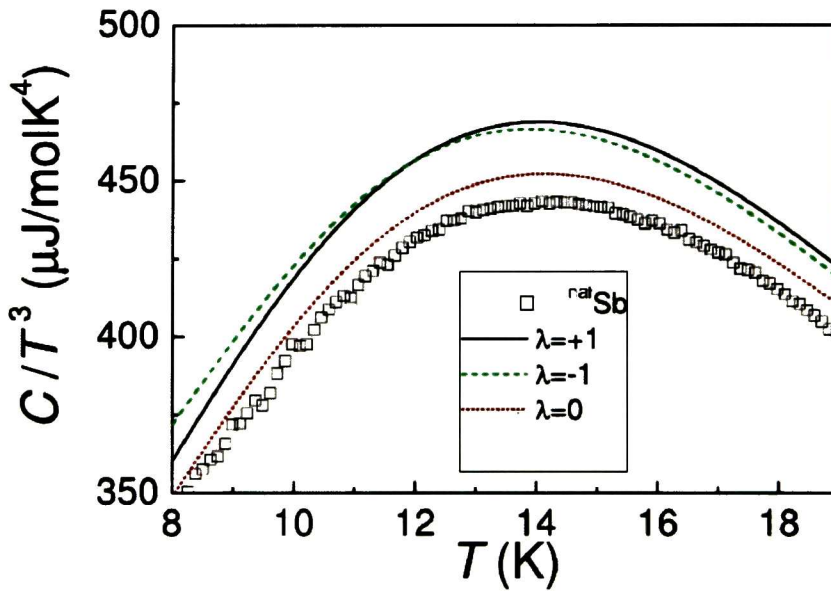
Figure 5.5: Dependence of the peak C/T^3 on the strength of the spin-orbit interaction. The symbols display our experimental data for the natural isotope composition, whereas the curves display the results of the calculations for $\lambda = +1$ (black, solid), $\lambda = 0$ (red, dotted) , and $\lambda = -1$ (green, dashed).

	Expt.		$\lambda = 0$		$\lambda = +1$		$\lambda = -1$	
	$A(E_g)$	$A(A_{1g})$	$A(E_g)$	$A(A_{1g})$	$A(E_g)$	$A(A_{1g})$	$A(E_g)$	$A(A_{1g})$
Γ			0.00	0.00	0.00	0.00	0.00	0.00
0.1	1.2		1.31	1.67	1.33	1.61	1.32	1.64
0.2	2.7		2.61	3.16	2.55	3.13	2.59	3.20
0.3	4.0		3.73	4.55	3.65	4.48	3.69	4.53
0.4	4.8	5.4	4.72	5.94	4.63	5.85	4.68	5.91
0.5	5.6	6.6	5.67	7.23	5.51	7.07	5.58	7.13
0.6	6.5	7.7	6.47	8.36	6.33	8.22	6.41	8.31
0.7	7.0	8.4	7.21	9.37	7.04	9.23	7.13	9.30
0.8	7.4	9.1	7.70	10.09	7.52	9.94	7.65	10.07
0.9	7.7	9.5	8.04	10.62	7.84	10.45	7.97	10.57
T	7.8	9.6	8.26	10.76	8.04	10.62	8.17	10.74

Figure 5.6: Phonon frequencies (meV) along the $\Gamma - T$ direction, calculated for Sb, corresponding to transverse $A(E_g)$ and longitudinal $A(A_{1g})$ acoustic modes. Experimental values from Ref. [112].

Chapter 6

Palladium dimer

6.1 Understanding magnetic properties on small palladium clusters

We did calculate the total energy with respect to variations in the distance between two palladium atoms from first principles with the use of density functional theory. We found two different curves for the total energy when the two atoms approach or retire to each other. The curve with the higher energy, around 2.44 Å, correspond to the *singlet state* and is reached when the two atoms are far from the internuclear distances and are moved closer. Starting with atoms at a short distance, we proceed to increase the separation between them and we follow the curve with the real minima which correspond to the *triplet state*. Because the difference between the singlet and the triplet state is the magnetization **m** of the system, with $m = 0\mu$ and $m = 2\mu$ respectively, we fixed the distance between the Pd_2 atoms and did calculate the total energy vs changes in the magnetization. At 2.7 Å, there exist only one curve that joins the point with higher energy and the one with the lowest energy with respect to changes in the magnetization. Whereas, at shorter distances, e.g., ~ 2.4 Å, there exist several curves to pass from one energy to the other, that mainly due to the overlap between different electronic orbitals. A detailed study about this behavior is presented in this chapter.

6.2 Introduction

Determining the electronic structure of small metal clusters is of interest in many scientific domains ranging from catalysis to new technologies. It remains nevertheless a challenge for scientist to obtain correctly the electronic structure of small transition metals clusters, even dimers. Palladium is one of such interesting chemical species for which even the dimer brings many questions. From the strict point of view of symmetry, the $4d^{10}$ closed shell configuration should not lead to a stable dimer. This Pd_2 molecule does however exist as the proximity of the $4d^9 5s^1$ configuration allows, through the mixing of both atomic configuration, stabilizing the system. This molecule has already been subject to some theoretical studies using a relativistic core potential (RCP). An extensive MRS-DCI ab initio study by Balasubramanian [115] identifies some 41 low energy lying electronic states for Pd_2. A local spin density (LDFT) computation by Songbook Lee and co-workers [116] identifies two triplet ground states while Taketoshi Nakao and collaborators [117] have treated the dimer at a nonlocal level using the Becke Perdue functional and obtain also a triplet ground state.

The purpose of our research is to obtain relevant information on small palladium clusters such as geometries, binding energies, electronic properties and so on. Pd_2 being the first of them, we have checked our approach on such a system using a usual atomic orbital basis set associated to the LANDZ core potential and the hybrid B3LYP density functional, which are known to behave fairly well for molecular species.

6.3 The problem

Obtaining the energy at a given geometry relies on an initial guess of the density, which in turn needs a guess at an initial Kohn Sham Orbital set. Currently, the orbitals are obtained from low cost semi-empirical methods or from a previously obtained density of some closely related geometry. The lowest energy orbitals are selected to build the density. This may lead to some unexpected results, as this trial set will induce a well-defined symmetry into the density, which might differ from the actual symmetry of the system and lead to a state lying above the fundamental state. Such problem will appear when the KS orbitals are lying close together, due to the proximity of various electron configurations, or when orbitals cross each other near definite geometries. This phenomenon is observed in Pd_2 and the curve described starting from large internuclear distances is different from the one obtained starting from short distances. It is the case either

for the triplet or for the singlet state. The density build upon the "n" first KS orbitals does not correspond to the lowest energy and the self-consistent process does not select the best set. The multiplicity will be conserved and symmetry maintained. Even when a reordering appears, as it is the case on the triplet curve coming from short distances (close to 2.9, 2.95 Å), the newly obtained orbitals are not yet the best. One will expect that this phenomenon be related to the quality of the used basis set. Indeed, for large basis sets, the flexibility introduced in the density representation should be very efficient and the orbital optimisation process should always have access to the optimal representation of the density, while for a smaller the basis set, some rigid constrain will be introduced by a lack of functions at disposal of the optimisation [122, 123]. This behavior is presented in Fig. 6.1 where the curves obtained starting from both sides of the distances are shown for the triplet as well as for the singlet using an atomic basis set approach [124].

To solve such an uncertainty, the only way out is a check at the obtained energy stability using an algorithm such as provided in the Gaussian package. Nevertheless a systematic check, guaranteeing the minimal energy, is usually unaffordable in most molecular systems. A very dense functional representation of the density is obtained in the plane wave approach of solid-state physics. It is the object of this paper to confront the atomic basis set approach, subject to the above presented limitations to the plane wave approach and to try to get a better insight in the nature of this problem by analysing both results. In addition to the previously works that have been reported in the literature about Pd properties and dimer in general [118–121].

Following the plane wave approach we used the ABINIT code [68–70] which is a package that performs density functional calculations of material properties using pseudopotentials and a plane-wave basis set. The exchange-correlation energy was computed using the local density approximation (LDA) in the Teter-Pade parametrization [50] and the pseudopotential used was the Hartwigsen-Goedecker-Hutter (HGH) pseudopotential [29] which is a norm-conserving relativistic separable dual-space Gaussian pseudopotential and is generated on the basis of a fully relativistic all-electron calculation. Using this pseudopotential it is also possible to reproduce only scalar relativistic effects by neglecting the terms for the SO contribution from HGH : this pseudopotential contains separately an average potential (that contains all scalar parts of the relativistic pseudopotential), and a vector part.
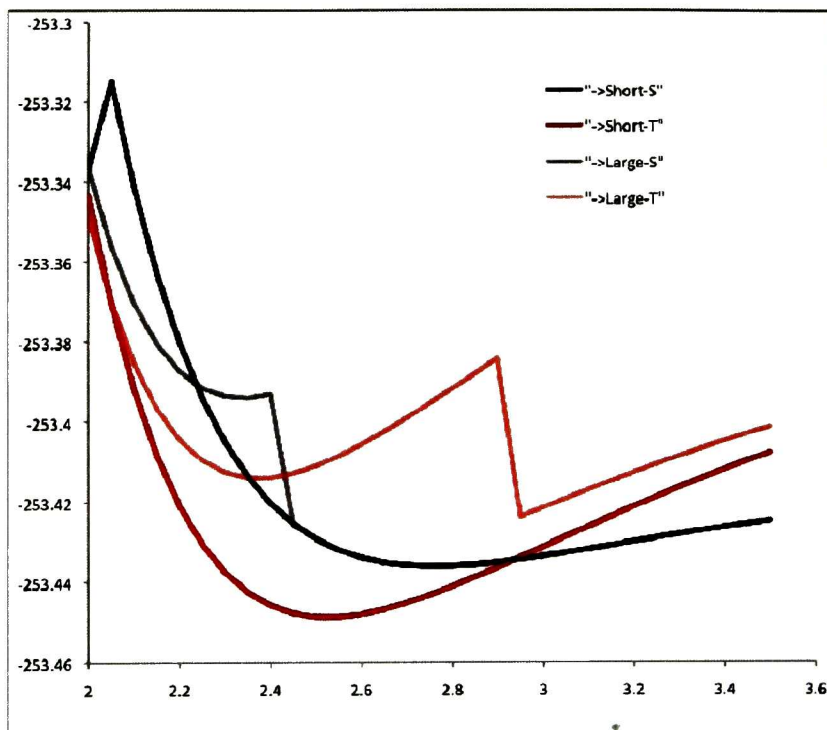
Figure 6.1: Total energy vs. bond length considering different kind of approximations

6.4 Results

Using plane waves as a basis set as implemented in the ABINIT code we considered different approximations in calculating the total energy of the dimer. These are the non-spin-polarized, spin-polarized, non-spin-polarized including spin-orbit interaction, and the full density matrix (spinorial, spin-polarized wave functions) including spin-orbit interaction (see Fig. 6.2). The latest will be studied in detail in Chapter 7. In the specific spin-polarized case we found a similar kind of results as the obtained using the atomic basis set approach (see Fig. 6.1 and Fig. 6.3 for compari).

Starting from here we shall be focused in the spin-polarized case approximation. The lowest energy (green line) curve is obtained from calculations starting
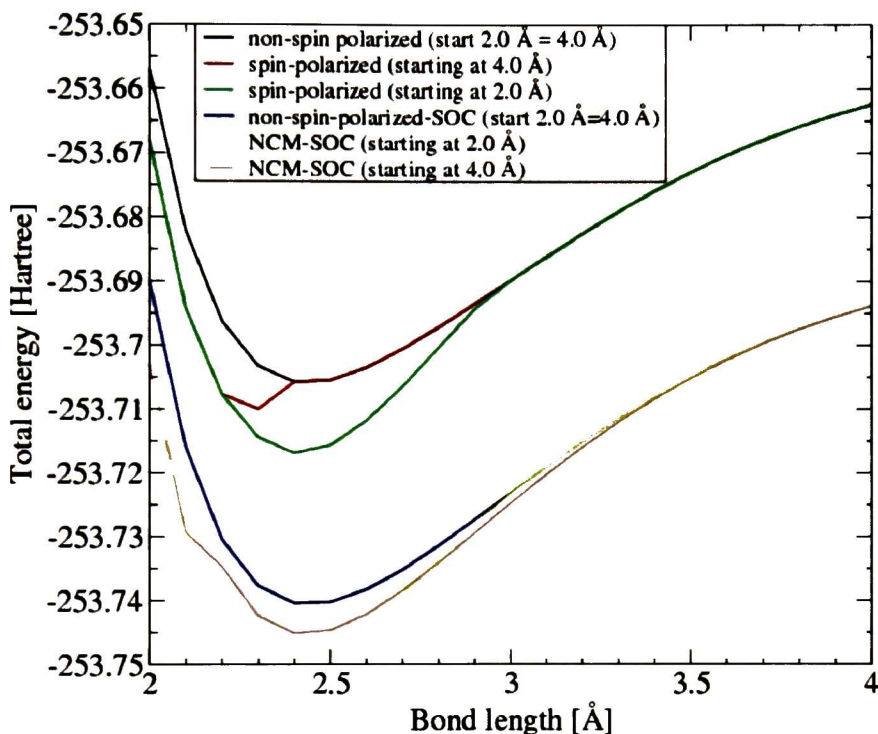
Figure 6.2: Total energy vs. bond length considering different kind of approximations

at short distances (2 Å). This curve has magnetization equal to two, in Bohr magneton units, that correspond to the triplet state, however, this magnetization value is kept only until the curve joins the others at around 2.9 Å. On the contrary, the red dotted line has magnetization equal to zero (singlet state) and it is obtained from a calculation when the atoms are at 4.0 Å. In this case the magnetization becomes two when the curve jumps down and joins the green dotted line around 2.2 Å. That means that the triplet state has the lowest energy at short distances, but around 3.0 Å the curve with the lowest energy correspond to the singlet state. This effect is showed in Fig. 6.2 (b) where the energy vs. bond length is plotted for the specific singlet and triplet cases.

Considering the previous result it is quit clear that the magnitude of the magnetization is the only variable that should be changed in order to jump from the

singlet to the triplet curve and *vice versa*. To ensure that this consideration is true, we fixed the distance between Pd atoms and changed the magnetization value from zero (singlet state) to two (triplet state) and *vice versa*. When the two Pd atoms are a bit far to each other, around 2.7 Å and 2.6 Å there exist only one well defined energy value in the singlet and the triplet state, hence the curve that joins these two points is unique. At shorter distances the electronic orbitals for each atoms start to overlap. At this point more than one value for the total energy, in the singlet state, appears and consequently there exist more than one curve joining these two points. In Fig. 6.3 each curve has an specific and a well defined electronic configuration an also an specific occupation numbers for each electronic orbital.
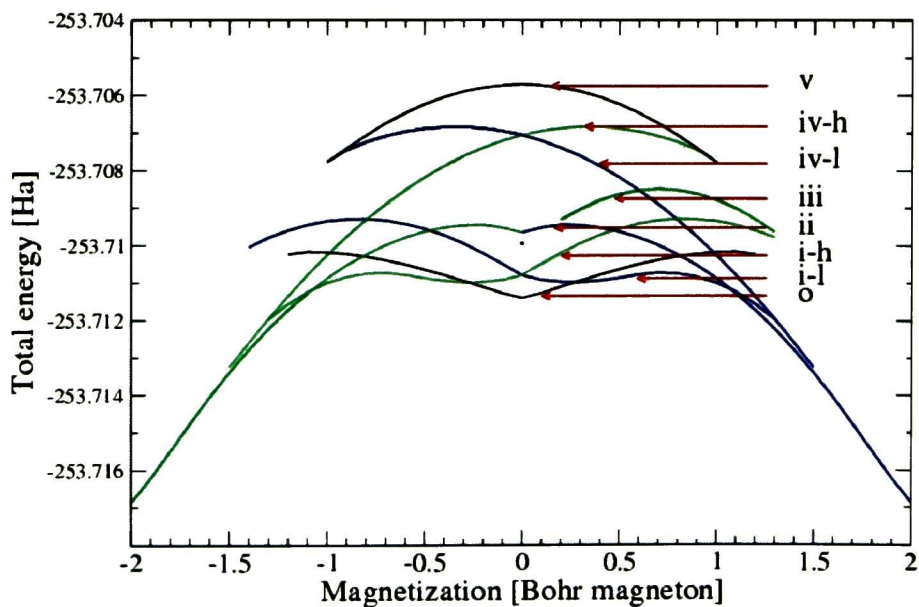

Figure 6.3: Total energy vs. magnetization. The distance between Pd atoms is fixed at 2.4Å

At 2.4 Å we found that the triplet state has a well defined electronic state that gives a unique energy value. On the other hand, in the singlet state there exist many states, with different energy each of them, near to each other. Something interesting is that the triplet and the lowest singlet state have a spin restricted configuration, i.e., although there are partially filled levels in the iterative process, the ground state is one of integral occupation numbers [125]

Trying to get and follow an specific curve showed in Fig. 6.3 is not the only problem using LDA and standard DFT method, but also trying to relax the structure for fractional occupation numbers and orbital coefficients because it causes slow convergence during the final stage when orbitals are fairly close to each other and to the Fermi energy.

We analysed in detail all the curves showed in Fig. 6.3. Each curve is defined in term of its electronic configuration and the orbital occupation number. It is possible to plot the relative energies of the atomic orbitals as a function of the magnetization. With that information it is also possible to know how the electronic structure and the atomic orbitals occupation number is evolving with respect to variation in the magnetization. The lowest energy correspond to the triplet state in which the spin up electronic configuration, from the higher to the lower energy, is given by $\pi^*(4d_{xz,yz})^1 \ \sigma(5s)^1 \ \delta^*(4d_{x^2-y^2,xy})^1 \ \sigma^*(4d_{z^2})^1$, and the spin down electronic configuration is $\sigma^*(4d_{z^2})^1 \ \sigma(5s)^1 \ \pi^*(4d_{xz,yz})^1 \ \delta^*(4d_{x^2-y^2,xy})^1$.

The Figures, from 6.4 to 6.11, are self explained. Each of these curves show in detail the electronic configuration and the occupation number for each of these states. At the top, these figures show the magnitude of the eigenvalues for the spin-up (left hand) and for the spin-down (right hand) configuration. At the bottom, the occupation numbers for each of the eigenstates are shown. For simplicity, we show only the occupation of the eigenvalues that have fractional occupation.

6.5 Conclusions

We did a detailed analysis of the electronic structure and population for palladium dimer considering the spin-polarized approximation and we find that the singlet state is composed for many different energy levels. The triplet state on the contrary, which correspond to the real ground state, has a unique and well defined energy value. The ground state is a triplet formed for the spin-up configuration $\pi^*(4d_{xz,yz})^1 \ \sigma(5s)^1 \ \delta^*(4d_{x^2-y^2,xy})^1 \ \sigma^*(4d_{z^2})^1$, and the spin-down con-

figuration $\sigma^*(4d_{z^2})^1 \; \sigma(5s)^1 \; \pi^*(4d_{xz,yz})^1 \; \delta^*(4d_{x^2-y^2,xy})^1$. This are ordered from higher to lower energy and Fig. (6.8) shows the way in which each bonding or antibonding is evolving from magnetization equal to zero to magnetization equal to two. Taking a look in detail in this figure, it is easy to notice that $\sigma^*(4d_{z^2})^1$ is the reponsible for this kind of behavior. Specially analysing the occupation for the spin-down configuration (see Fig. 6.8d), it is easy to realize that it pass from an empty to a completely full occupied state and that the $\sigma(5s)^1$ is completely empty along.

Also interesting is that the singlet state with lowest energy has a spin restricted configuration similar to the triplet state, but with an strong polarization in the charge distribution, i.e., for the spin-up configuration the energy levels ordered from highest to lowest energy are $\sigma^*(4d_{z^2})^1$ with only one atoms having this charge distribution, lets say the left atom, $\pi^*(4d_{xz,yz})^1$ double degenerated, $\delta^*(4d_{x^2-y^2,xy})^1$, double degenerated but this time and again only one atom with this configuration, but now lets say the right atom with a bit more amount of charge $\sigma^*(4d_{z^2})^1$

Figure 6.4: Atomic orbitals (Figures (6.4a) and (6.4b)) and occupation number (Figures (6.4c) and (6.4d)) to the curve with the highest energy in Figure 6.3. Figures (6.4a) and (6.4c) correspond to the spin-up case. Figures (6.4b) and (6.4d) correspond to the spin-down case.

(a)

(b)

(c)

(d)

Figure 6.5: Atomic orbitals (Figures (6.5a) and (6.5b)) and occupation number (Figures (6.5c) and (6.5d)) to the curve with labeled as (iv-h) in Figure 6.3. Figures (6.5a) and (6.5c) correspond to the spin-up case. Figures (6.5b) and (6.5d) correspond to the spin-down case.

(a)

(b)

(c)

(d)

Figure 6.6: Atomic orbitals (Figures (6.6a) and (6.6b)) and occupation number (Figures (6.6c) and (6.6d)) to the curve with labeled as (iv-l) in Figure 6.3. Figures (6.6a) and (6.6c) correspond to the spin-up case. Figures (6.6b) and (6.6d) correspond to the spin-down case.
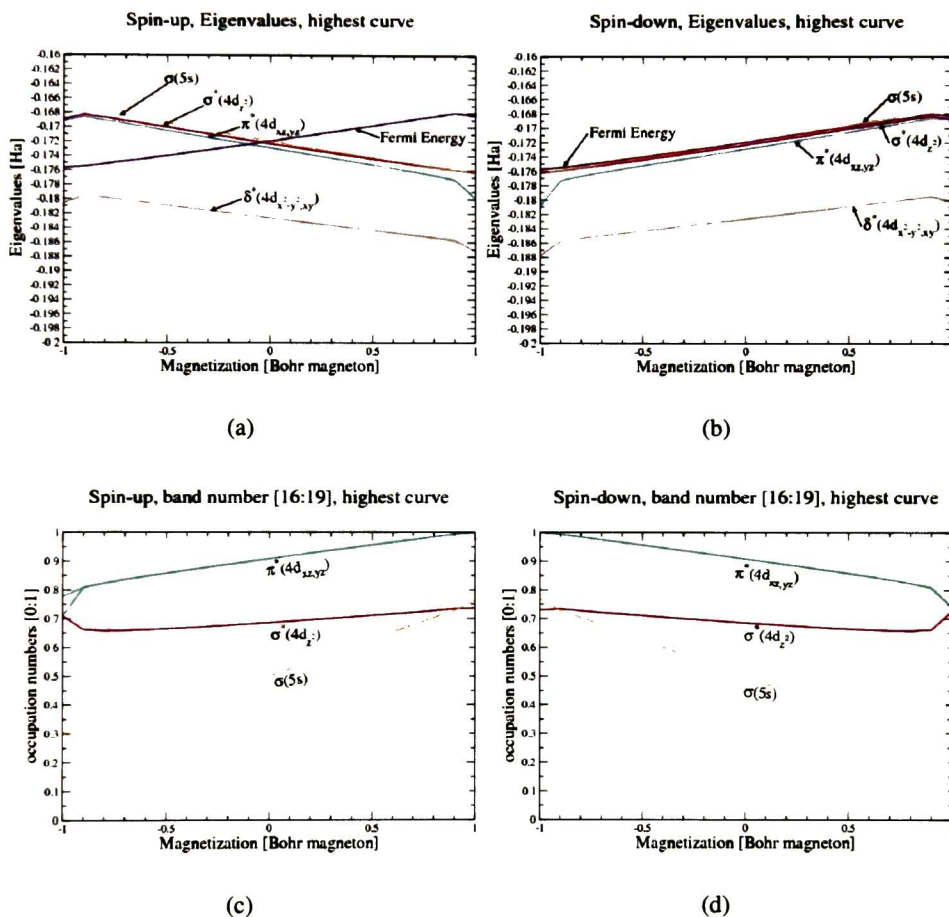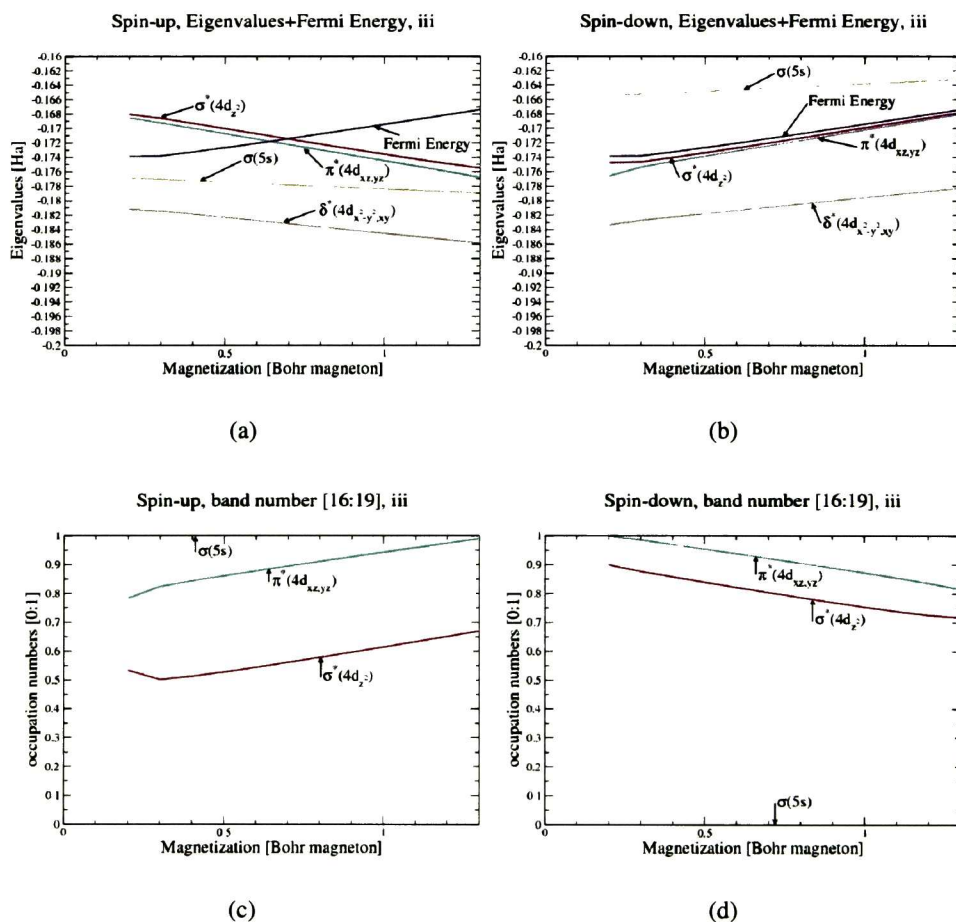
Figure 6.7: Atomic orbitals (Figures (6.7a) and (6.7b)) and occupation number (Figures (6.7c) and (6.7d)) to the curve with labeled as (iii) in Figure 6.3. Figures (6.7a) and (6.7c) correspond to the spin-up case. Figures (6.7b) and (6.7d) correspond to the spin-down case.
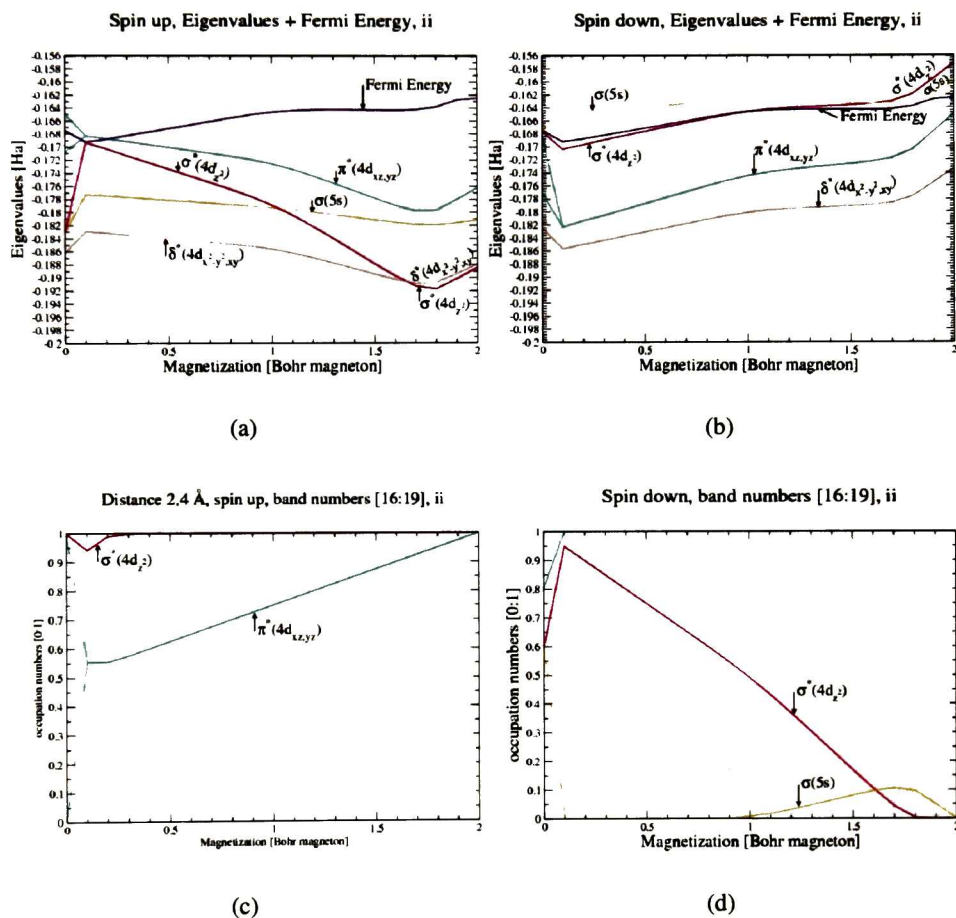
Figure 6.8: Atomic orbitals (Figures (6.8a) and (6.8b)) and occupation number (Figures (6.8c) and (6.8d)) to the curve with labeled as (ii) in Figure 6.3. Figures (6.8a) and (6.8c) correspond to the spin-up case. Figures (6.8b) and (6.8d) correspond to the spin-down case.
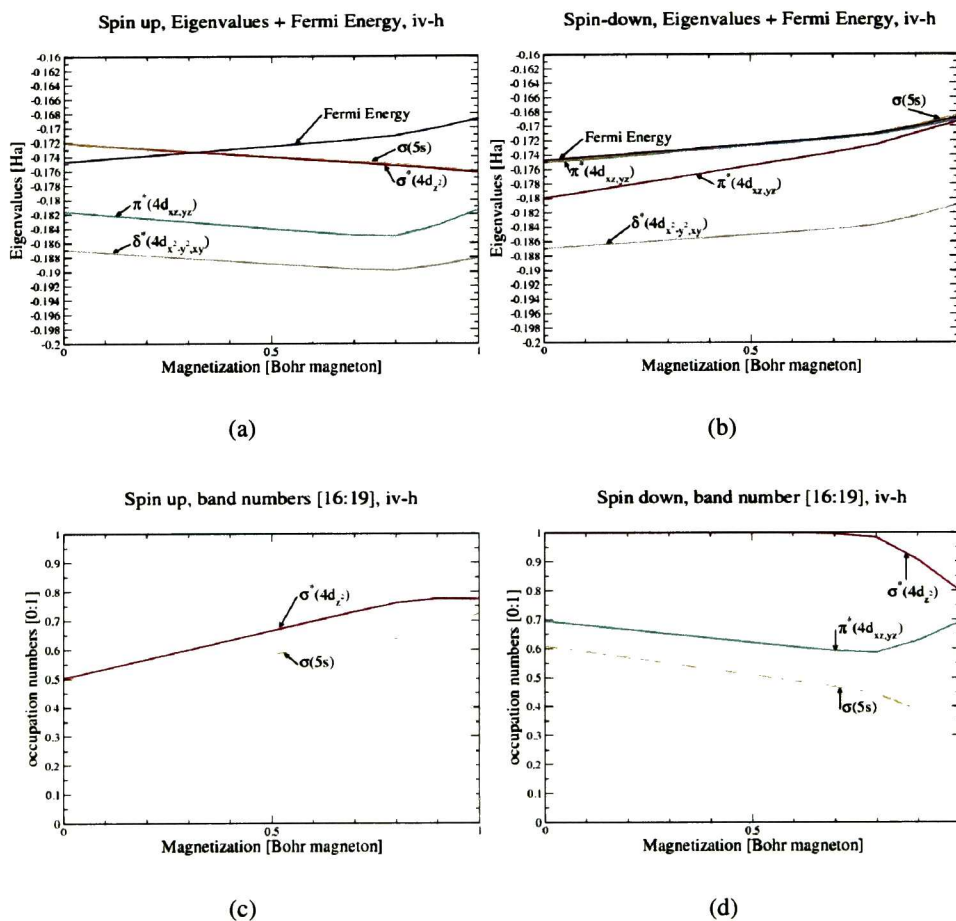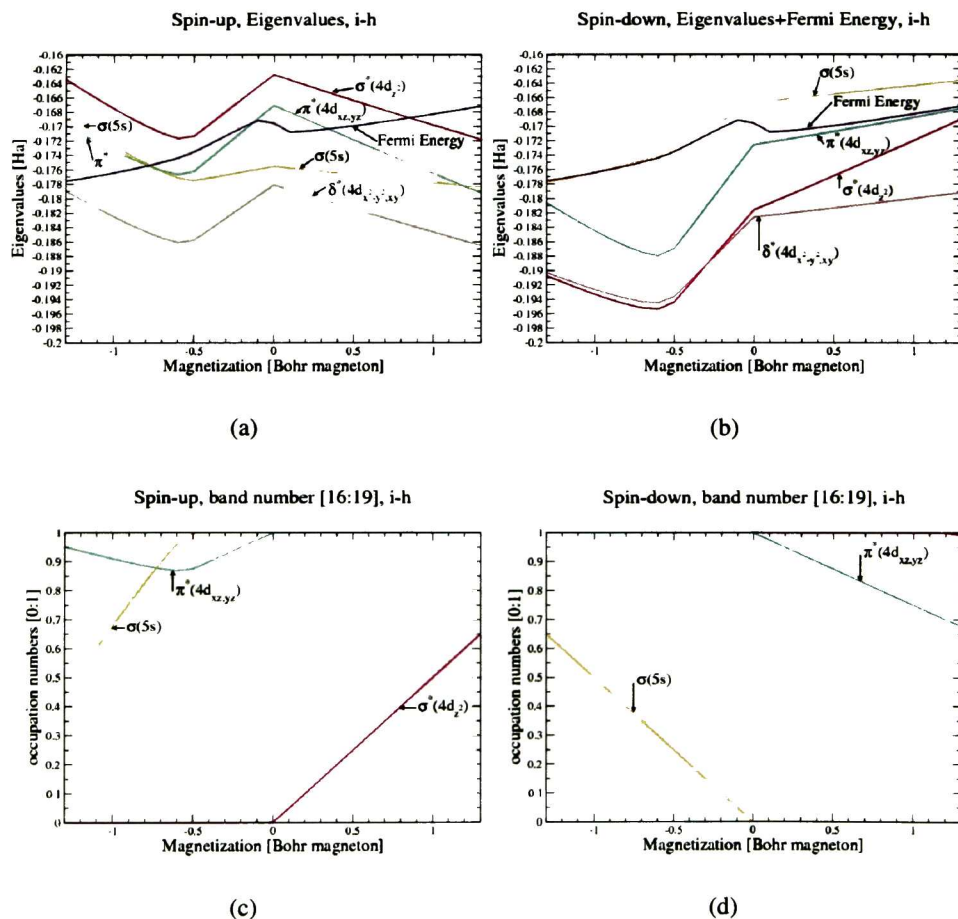
Figure 6.9: Atomic orbitals (Figures (6.9a) and (6.9b)) and occupation number (Figures (6.9c) and (6.9d)) to the curve with labeled as (i-h) in Figure 6.3. Figures (6.9a) and (6.9c) correspond to the spin-up case. Figures (6.9b) and (6.9d) correspond to the spin-down case.

Figure 6.10: Atomic orbitals (Figures (6.10a) and (6.10b)) and occupation number (Figures (6.10c) and (6.10d)) to the curve with labeled as (i-1) in Figure 6.3. Figures (6.10a) and (6.10c) correspond to the spin-up case. Figures (6.10b) and (6.10d) correspond to the spin-down case.
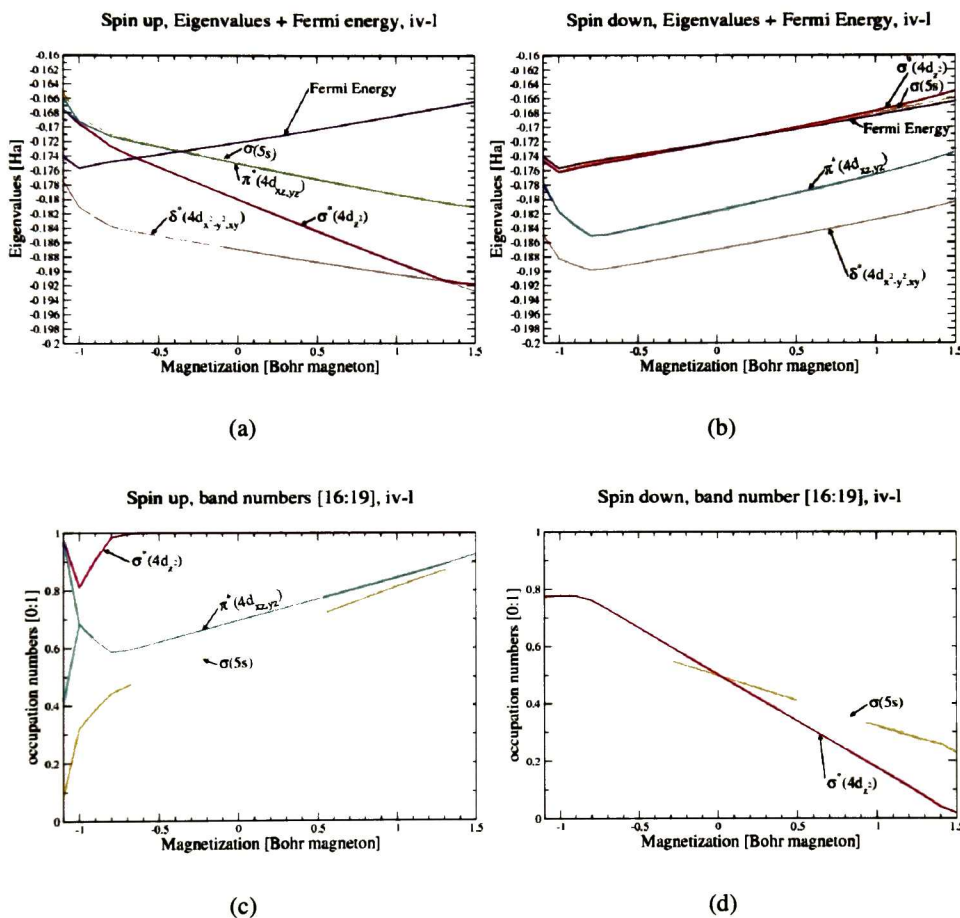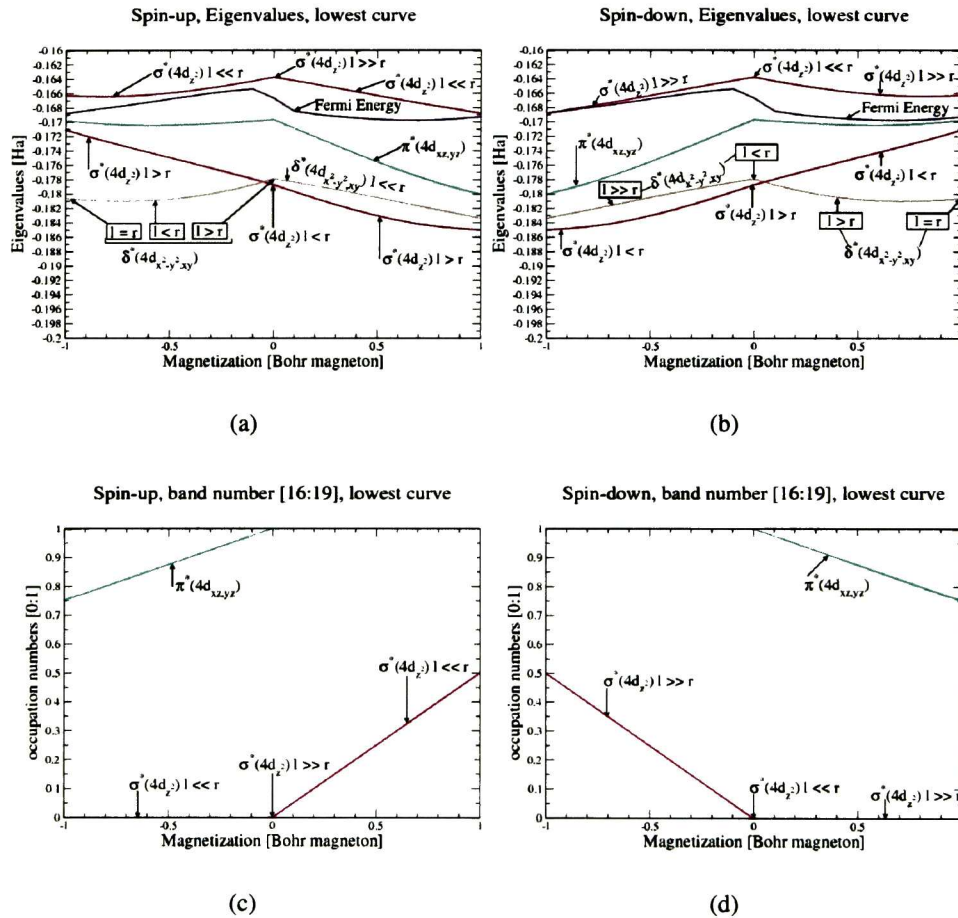
Figure 6.11: Atomic orbitals (Figures (6.11a) and (6.11b)) and occupation number (Figures (6.11c) and (6.11d)) to the curve with the lowest energy, labeled as 0 in Figure 6.3. Figures (6.11a) and (6.11c) correspond to the spin-up case. Figures (6.11b) and (6.11d) correspond to the spin-down case.
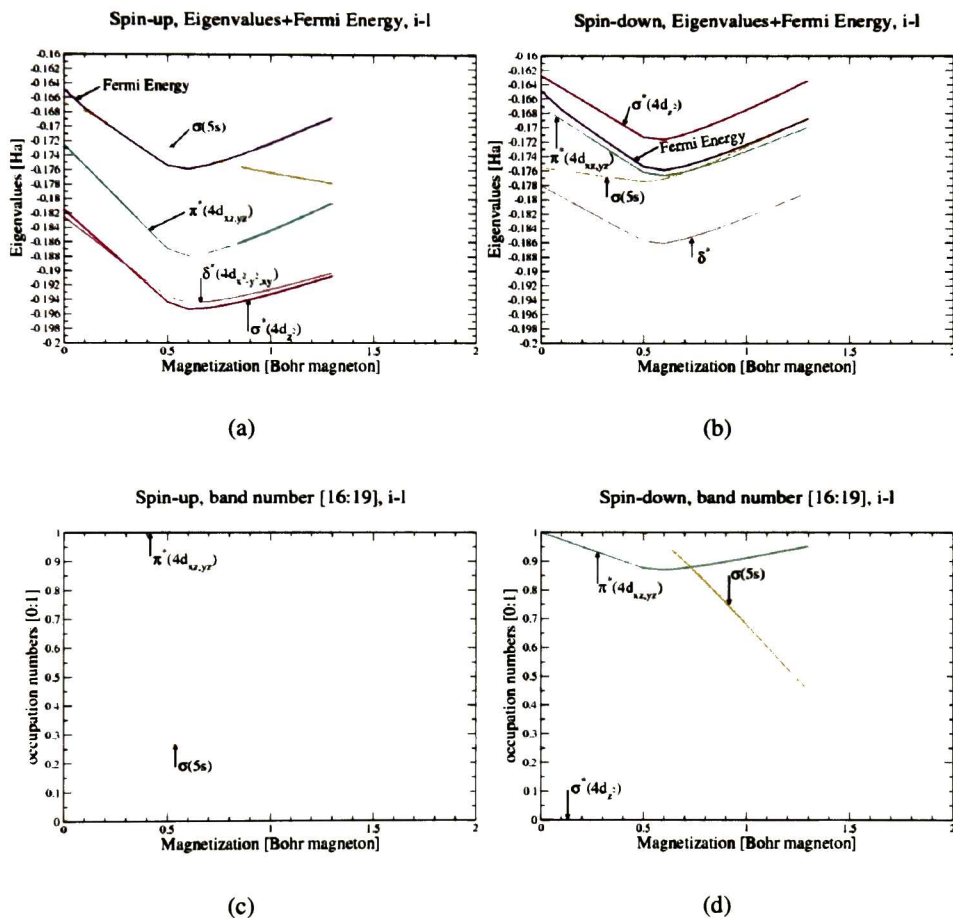
Chapter 7

Non collinear calculations including spin-orbit interaction

7.1 Non collinear calculations including spin-orbit interaction

In this chapter we consider the noncollinear magnetic and the spin-orbit coupling approximations, both of them at the same time in the calculi. First, we have started with the most simple case, the non-spin-polarized approximation, and we continue improving the calculi with new approximations, like the spin-polarized one. Finally, we compare the results of the previous mentioned approximations with the results we get considering the noncollinearity and the spin-orbit coupling at the same time. In the first section of this chapter we analyze the electronic structure of bismuth and palladium atom. In the second section are discusses the electronic properties of the bismuth and palladium dimers. Finally, in the third section we present a tight-binding like theoretical study.

7.2 Bi and Pd atom, isolated in a big box

In order to calculate electronic properties for bismuth and palladium, we used the ABINIT code [68–70]. As we mentioned en previous chapters, this package performs density functional calculations of material properties using pseudopotentials and a plane-wave basis set. The exchange-correlation energy is computed using the local density approximation (LDA) in the Teter-Pade parametrization [50]. We used the Hartwigsen-Goedecker-Hutter (HGH) pseudopotential

[29] which is a norm-conserving relativistic separable dual-space Gaussian pseudopotential and is generated on the basis of a fully relativistic all-electron calculation. Using this pseudopotential, we included SO interaction effects relevant for heavier elements like Bi. It is possible to reproduce only scalar relativistic effects by neglecting the terms for the SO contribution from HGH : this pseudopotential contains separately an average potential (that contains all scalar parts of the relativistic pseudopotential), and a vector part.

Since we are working with an isolated bismuth and palladium atom there is no dispersion in the band structure and we just need 1 k point grid to approximate the integrals on the wavevectors of the electronic wavefunction.

We used a metallic occupation level that correspond to the the Gaussian smearing, corresponding to the 2-order Hermite polynomial of Ref. [74]. The broadening of occupation numbers was determined by a smearing energy of 0.01 Ha.

Bismuth nucleus is quite heavy, with atomic number $Z = 83$. Palladium cluster is magnetic, with atomic number $Z = 46$. In bismuth, only the $6s^2 6p^3$ electrons can be considered as valence electrons, that because only s and p levels will mix in the solid, while the other d-electron and core electron levels will remain practically unchanged. For palladium, the electronic configuration is $[Kr]4d^{10}5s^0$, for that reason we consider ten valence electrons for this atom.

First in the most simple approximation, i.e., considering the wavefunction as an scalar, the spin-unpolarized approximation and considering no spin-magnetization. For bismuth we obtain that the s level is double occupied and the p level single occupied. Because we are no considering relativistic effects, we did not get any splitting in the p level. For that reason we only mention that the differences in energies between the $6s^2$ and the $6p^3$ levels is about 9.9 eV. Followin a similar study, the differences in energies between the $4d^{10}$ and the $4p^6$ is about 47 eV, which is really big.

Finally, considering the most general case, i.e., the noncollinearity and the spin-orbit interaction, we obtain that on bismuth, the spin-orbit interaction split the external p atomic levels by about 1.42 eV ($6p^{1/2} - 6p^{3/2}$ splitting), an effect that can be seen in the electronic density of states of the periodic solid. On palladium, the spin-orbit interaction split the external d atomic levels by about 0.44 eV ($4d^{5/2} - 4d^{3/2}$).

7.3 Bi2 and Pd2 isolated in a big box

we also analyzed the bismuth dimer and palladium dimer. The technical details are quite similar to the crystalline case, except that we placed the system in a big cell. We found that the bond distance between a pair of Bi atoms is equal to 4.8607 Bohr for the case when the SO is not considered, while it is equal to 4.9166 Bohr when the SO coupling is taken into account. Going from the molecule to the solid decreases the nearest-neighbor distance significantly. The SO interaction causes a little increment in the bond length, in agreement with our previous result for solid Bi. The longitudinal IFC is equal to the on-site IFC for a dimer. In the case without SO, we obtain an on-site IFC value of 157.7×10^{-3} Ha/Bohr^2, while it drops to 130.5×10^{-3} Ha/Bohr^2 when the SO coupling is taken into account. Although the IFCs in the solid and the molecule are quite different, the effect of SO is qualitatively the same again.

Both the lengthening of the bond length increase and weakening of the IFCs can be rationalized, in a very qualitative way, by an analysis of the electronic structure of the molecule. Indeed, in the case without SO, the HOMO corresponds to twofold degenerate bonding π states, the LUMO corresponds to antibonding π^* states also twofold degenerate, separated by 2.2 eV only. Turning on the SO coupling leads to a mixing of bonding and antibonding orbitals, weakening the bond and increasing the bond length, on one hand. On the other hand, it diminishes the energy gap between the HOMO and the LUMO to a value of 1.3 eV, an effect that weakens the IFCs.

In addition to the details previously mentioned. We also calculate the total energy of the bismuth dimer as a function of the distance. A similar study was done in chapter 6, the big difference with that results is that in chapter 6 we only consider the spin-polarized approximation, and here, the noncollinearity and the relativistic effect is considered. Because bismuth is not magnetic we did not find differences in the magnitude of the total energy neither starting our calculations at short distances between bismuth atoms nor starting the calculations at larger distances. At distances larger than 3 Å, there exist two curves that have different energies. This difference is due to the initial magnetic configuration that we impose to the system and not to a magnetic effect.

For palladium we also did the same kind of calculation. Again we found an hysteresis effect. This curves was obtained starting the calculation at 4 Å between palladium atoms. Imposing to the system different initial magnetic configurations we follow curves with different energies. That shows again the hysteresis effect, and in general, the magnetic properties in palladium dimer.
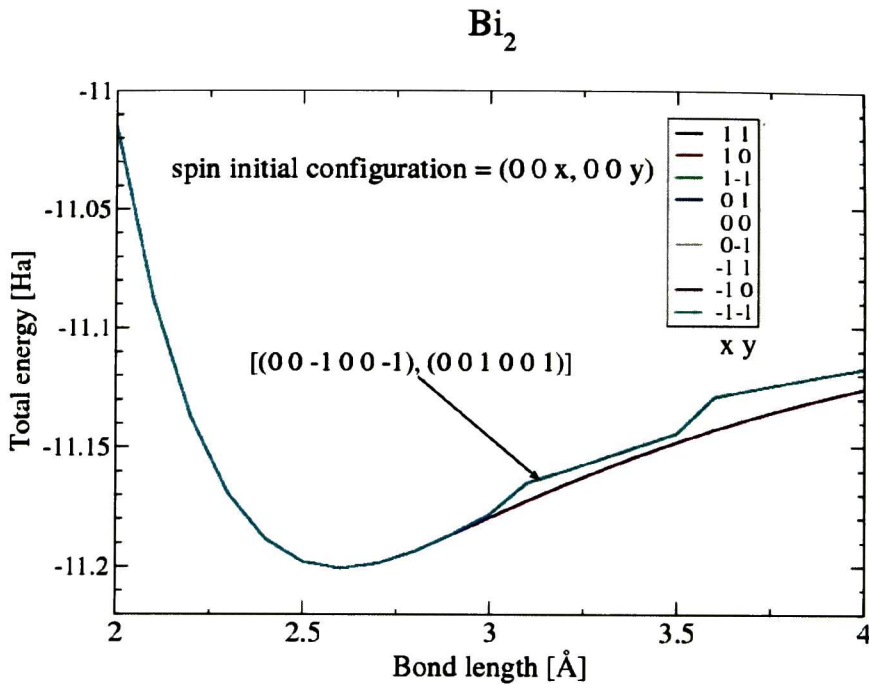
Figure 7.1: Total energy vs bond length. Because bismuth is not magnetic we did not find differences in the magnitude of the total energy neither starting our calculations at short distances between bismuth atoms nor starting the calculations at larger distances

7.4 Tight Binding model

In this section we consider again a bismuth atom and we investigate the many-body treatment of the effect of spin-orbit coupling for the Bi atom using tight binding like a model. Focusing only on the open shell (6p, with three electrons). As taking into account closed shells (6s and others, lower in energy) should not make appear any contribution fromo spin-orbit to first-order, this is the crucial information.
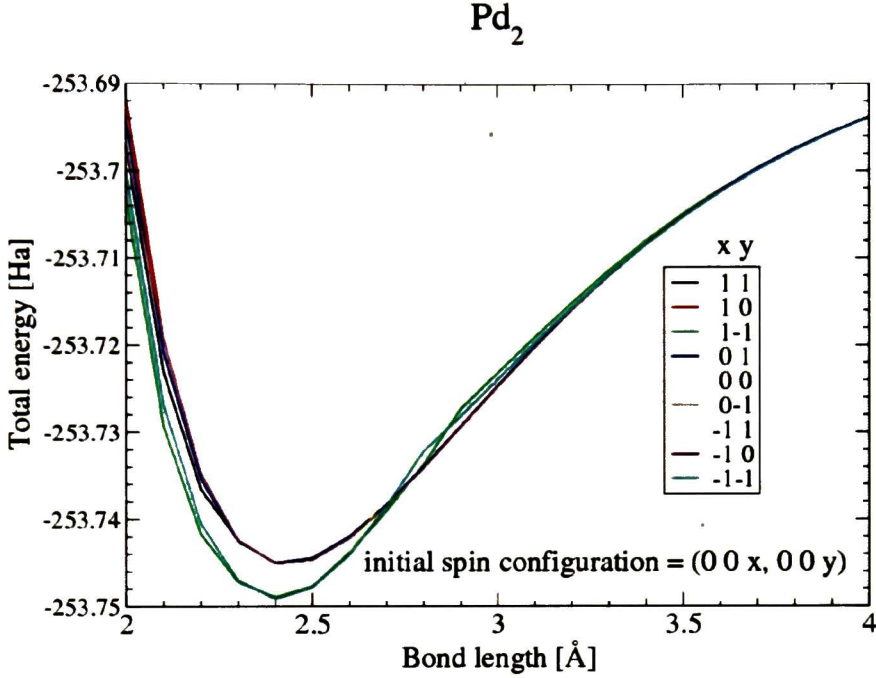
Figure 7.2: Total energy vs bond length. It is clear that there exist a hysteresis effect that split the path in two curves with different energies. This kind of effect does not occur in bismuth dimer.

7.4.1 Evaluation of the expectation value of the Spin-Orbit operator - bismuth atom

The electronic configuration for bismuth is $Bi = [Xe]4f^{14}5d^{10}6s^26p^3$. Considering $l = 1$ (p orbitals) and the two possible values for the spin of the electron, $m_s = \pm 1/2$, the standard basis that should be considered is:

$$(\uparrow \; +1; \; \uparrow \quad 0; \; \uparrow \; -1; \; \downarrow \; +1; \; \downarrow \quad 0; \; \downarrow \; -1). \qquad (7.1)$$

On the other hand, we want to analize the spin-orbit coupling dependence defined in the hamiltonian and also the depencende of this term with respect to a perturbational λ parameter:

$$H_{SOC} = \lambda \, \xi(r)\mathbf{L} \cdot \mathbf{S}. \qquad (7.2)$$

105

The spin-orbit operator, at lowest order in many-body theory, is the sum of independent-particle spin-orbit operators,

$$\sum_i (L_{xi} \cdot S_{xi} + L_{yi} \cdot S_{yi} + L_{zi} \cdot S_{zi}), \tag{7.3}$$

The operator $\mathbf{L} \cdot \mathbf{S}$ related with the spin-orbit interaction can be rewriten in terms of the shift (lowering-raising) operators L_+, L_-, S_+, and S_-, adjoints to each other and the z components,

$$\mathbf{L} \cdot \mathbf{S} = \frac{1}{2}(L_+ S_- + L_- S_+) + L_z S_z, \tag{7.4}$$

where each of the shift operators is defined as:

$$
\begin{aligned}
L_+ &= L_x + iL_y. \\
L_- &= L_x - iL_y. \\
S_+ &= S_x + iS_y. \\
S_- &= S_x - iS_y.
\end{aligned}
\tag{7.5}
$$

Using the basis given by (7.1) and the latter operators,

$$
\begin{aligned}
L_+ S_- | \uparrow \ +1 > &= 0 \\
L_+ S_- | \uparrow \ \ \ 0 > &= \sqrt{2}\,\beta\,| \downarrow \ +1 > \\
L_+ S_- | \uparrow \ -1 > &= \sqrt{2}\,\beta\,| \downarrow \ \ \ 0 > \\
L_+ S_- | \downarrow \ +1 > &= 0 \\
L_+ S_- | \downarrow \ \ \ 0 > &= 0 \\
L_+ S_- | \downarrow \ -1 > &= 0
\end{aligned}
$$

$$
\begin{aligned}
L_- S_+ | \uparrow \ +1 > &= 0 \\
L_- S_+ | \uparrow \ \ \ 0 > &= 0 \\
L_- S_+ | \uparrow \ -1 > &= 0 \\
L_- S_+ | \downarrow \ +1 > &= \sqrt{2}\,\beta\,| \uparrow \ \ \ 0 > \\
L_- S_+ | \downarrow \ \ \ 0 > &= \sqrt{2}\,\beta\,| \uparrow \ -1 > \\
L_- S_+ | \downarrow \ -1 > &= 0
\end{aligned}
$$

$$L_z S_z | \uparrow \; +1 > \; = \; \frac{1}{2} | \uparrow \; +1 >$$

$$L_z S_z | \uparrow \quad 0 > \; = \; 0$$

$$L_z S_z | \uparrow \; -1 > \; = \; -\frac{1}{2} | \uparrow \; -1 >$$

$$L_z S_z | \downarrow \; +1 > \; = \; -\frac{1}{2} | \downarrow \; +1 >$$

$$L_z S_z | \downarrow \quad 0 > \; = \; 0$$

$$L_z S_z | \downarrow \; -1 > \; = \; \frac{1}{2} | \downarrow \; -1 >$$

In order to determine all the eigenvalues it is necessary to determine the secular equation given by,

$$|H_{nm}(\mathbf{k}) - E(\mathbf{k})\delta_{nm}| = 0, \tag{7.6}$$

in matrix notation the secular equation can be written as follow,

$$\begin{pmatrix} \epsilon_\uparrow + \lambda\frac{\alpha}{2} - \epsilon & 0 & 0 & 0 & \lambda\frac{\alpha}{2}\sqrt{2}\beta & 0 \\ 0 & \epsilon_\uparrow - \epsilon & 0 & 0 & 0 & \lambda\frac{\alpha}{2}\sqrt{2}\beta \\ 0 & 0 & \epsilon_\uparrow - \lambda\frac{\alpha}{2} - \epsilon & 0 & 0 & 0 \\ 0 & 0 & 0 & \epsilon_\downarrow - \lambda\frac{\alpha}{2} - \epsilon & 0 & 0 \\ \lambda\frac{\alpha}{2}\sqrt{2}\beta & 0 & 0 & 0 & \epsilon_\downarrow - \epsilon & 0 \\ 0 & \lambda\frac{\alpha}{2}\sqrt{2}\beta & 0 & 0 & 0 & \epsilon_\downarrow + \lambda\frac{\alpha}{2} - \epsilon \end{pmatrix} = 0 \tag{7.7}$$

This matrix can be represented as:

$$\begin{pmatrix} a & 0 & 0 & 0 & g & 0 \\ 0 & b & 0 & 0 & 0 & g \\ 0 & 0 & c & 0 & 0 & 0 \\ 0 & 0 & 0 & d & 0 & 0 \\ g & 0 & 0 & 0 & e & 0 \\ 0 & g & 0 & 0 & 0 & f \end{pmatrix} = 0, \tag{7.8}$$

where the value for each term in the expression (7.8) is directly related with (7.7). We find that the secular equation (7.6) can be rewriten as:

$$cd(ea - g^2)(fb - g^2) = 0 \tag{7.9}$$

The six eigenvalues can be obtained from last equation,

$$\epsilon_1 = \epsilon_\uparrow - \lambda\frac{\alpha}{2};$$

$$\epsilon_2 = \epsilon_\downarrow - \lambda\frac{\alpha}{2};$$

$$\epsilon_{3,4} = \frac{(\epsilon_\downarrow + (\epsilon_\uparrow + \lambda\frac{\alpha}{2}))}{2} \pm \sqrt{\left(\frac{\epsilon_\downarrow - (\epsilon_\uparrow + \lambda\frac{\alpha}{2})}{2}\right)^2 + (\frac{1}{\sqrt{2}}\lambda\alpha\beta)^2}$$

$$\epsilon_{5,6} = \frac{(\epsilon_\uparrow + (\epsilon_\downarrow + \lambda\frac{\alpha}{2}))}{2} \pm \sqrt{\left(\frac{\epsilon_\uparrow - (\epsilon_\downarrow + \lambda\frac{\alpha}{2})}{2}\right)^2 + (\frac{1}{\sqrt{2}}\lambda\alpha\beta)^2}$$

In order to find the value for α it should be enough to put $\lambda = 1$ and to plot a linear value for the energy $\epsilon_{1,2}$. To find the value for β it would be needed to plot the total energy for the non-linear cases $\epsilon_{3,4,5,6}$ and to change β to fix the curve considering $\lambda = 0$ or $\lambda = 1$.

Chapter 8

Conclusions and perspectives

Density Functional Theory has proved to be highly successful in understanding magnetic anisotropies, i.e., magnetic properties where the magnetic moment has a preferential direction. In particular we used this theory to understand one of the most important relativistic effects, the spin orbit interaction, and its effect in vibrational and thermodynamic properties. We also show the important of considering freedom in the orientation of the intrinsic electronic magnetic moment. Finally, we analyze our systems with both approximations. We calculate the total energy on different dimers and these results were compared with calculations using the spin polarized approximation, i.e., we compare our results with approximations where only the spin-up and the spin-down configuration are allowed in a system. The spin-orbit interaction and the noncollinear magnetization are some the most important theoretical considerations in the field of magnetism, but of course, these are not the only approximation that play an important role in to deal with magnetic systems.

It is not necessary to clarify, but important to mention that magnetism is a *young* area of research. Young in the sense that recently, it dates back from 1980's, this field of research has acquired importance. Mainly because the 2007 Nobel Prize in physics was awarded to Albert Fert and Peter Grünberg for the discovery of giant magnetoresistance. Also the discoveries in a new field called spintronic were quite rapid, and the path toward a new technology started to appear quite early. That originated a boom in the field of magnetism. The spintronic not only exploit the fundamental electronic charge of the electrons but also the intrinsic spin of electrons and its associated magnetic moment. The word spintronics is an acronym for spin transport electronics that was first introduced in 1996.

Further applications abound, at present it is normal to apply this effects in the storage density of hard drives or in magnetic random access memory. The conventional electronic is based on the charge of the electron, but thinking in the future, one could imagine to have full control of the other fundamental property of the electron, its intrinsic magnetic moment. To control the spin is very useful to store much more amount of information in hard disks. Another important aspect is the spin momentum transfer that might be useful to send information through long distances in a faster and more secure way. In adition, all these applications are potentially lower in power, for that reason, that is reflected in reduction in energy costs. Complementary-metal-oxide-semiconductor are special magnetic materials like the used in microprocessors, microcontrollers, static RAM, and other digital logic circuits. Another interesting topic is the spin momentum transfer that might be useful to send information through long distances in a faster and more secure way. The purpose of the last thrust, designated quantum spin effects, was to explore the possibility of using the spin degree of freedom as a quantum bit for quantum information processing. Underlying all of these thrusts, one is the development and understanding the behavior of the spin degree of freedom in various semiconductors, both ferromagnetic and non-ferromagnetic, and the vigorous pursuit of new ferromagnetic compounds that have Curie temperatures well above room temperature.

Appendix A

Density Matrix and Spin Density Vector

This appendix is devoted to clarify in a bit more detail the origin of the magnetization components, m_x, m_y, and m_z, in term of the components of the density matrix ρ_{ij}. The comprehension of the continuous variation in the orientation of the magnetization is crucial for studying systems where magnetic excitations play an important role, such as spin waves, or to threat magnetism at finite temperature. More detailed information about it can be found in section 2.4. First we shall introduce the density matrices from the general point view.

In his book on statistical mechanics Feynman makes the following statement about the density matrix. *When we solve a quantum-mechanical problem, what we really do is divide the universe into two parts - the system in which we are interested and the rest of the universe. We then usually act as if the system in which we are interested comprised the entire universe. To motivate the use of density matrices, let us see what happens when we include the part of the universe outside the system* [133].

In that context, let x describe the coordinates of the system, and let y describe the rest of the universe. Let $\varphi_i(x)$ be a complete set of wave functions. The most general wave function can be written,

$$\psi(x, y) = \sum_i C_i(y)\varphi_i(x). \tag{A.1}$$

Using Dirac notation, let $|\varphi_i\rangle$ be a complete set of vectors in the vector space describing the system, and let $|\theta_i\rangle$ be a complete set for the rest of the universe.

$$\varphi_i(x) = \langle x|\varphi_i\rangle \quad \text{and} \quad \theta_i(y) = \langle y|\theta_i\rangle. \tag{A.2}$$

The most general wave function can be written as,

$$|\psi\rangle = \sum_{ij} C_{ij}|\varphi_i\rangle|\theta_j\rangle \tag{A.3}$$

$$\psi(x,y) = \langle y|\langle x|\psi\rangle = \sum_{ij} C_{ij}\langle x|\psi_i\rangle\langle y|\theta_j\rangle. \tag{A.4}$$

Equation (A.1) can be obtaining by taking,

$$C_i(y) = \sum_{j} C_{ij}\langle y|\theta_j\rangle. \tag{A.5}$$

Now let A be an operator that acts only on the system; that is to say, A does not act on the θ_j. When A acts on product states (for example, $|\psi\rangle$) we really mean $A|a\rangle|b\rangle \equiv (A|a\rangle)|b\rangle$. In such a case A does not equal,

$$\sum_{ii'} A_{ii'}|\varphi_i\rangle\langle\varphi_{i'}|, \tag{A.6}$$

but equals,

$$\sum_{ii'j} A_{ii'}|\varphi_i\rangle|\theta_j\rangle\langle\theta_j|\langle\varphi_{i'}|. \tag{A.7}$$

Then,

$$\langle A\rangle = \langle\psi|A|\psi\rangle = \sum_{ij} C_{ij}^* C_{i'j'}\langle\theta_j|\langle\varphi_i|A|\varphi_{i'}\rangle|\theta_{j'}\rangle \tag{A.8}$$

$$= \sum_{iji'} C_{ij}^* C_{i'j}\langle\varphi_i|A|\varphi_{i'}\rangle, \tag{A.9}$$

$$= \sum_{ii'} \langle\varphi_i|A|\varphi_{i'}\rangle\rho_{i'i}, \tag{A.10}$$

$$\tag{A.11}$$

where,

$$\rho_{i'i} = \sum_{j} C_{ij}^* C_{i'j} = \text{density matrix.} \tag{A.12}$$

We define the operator ρ to be such that $\rho_{i'i} = \langle\varphi_{i'}|\rho|\varphi_i\rangle$. ρ operates only on the system described by x.

$$\langle\psi|A|\psi\rangle = \sum_i \langle\varphi_i|A\sum_{i'}|\varphi_{i'}\rangle\langle\varphi_{i'}|\rho|\varphi_i\rangle, \tag{A.13}$$

$$= \sum_i \langle\varphi_i|A\rho|\varphi_i\rangle = \mathrm{Tr}\rho A. \tag{A.14}$$

Where we have used the result,

$$\sum_{i'}|\varphi_{i'}\rangle\langle\varphi_{i'}| = 1 \quad \text{(by completeness arguments)}. \tag{A.15}$$

From Eq. (A.12), it is obvious that ρ is hermitian. Therefore it can be diagonalized with a complete orthonormal set of eigenvectors $|i\rangle$ and real eigenvalues v_i,

$$\rho = \sum_i v_i |i\rangle\langle i|. \tag{A.16}$$

If we let A be 1, we obtain,

$$\sum_i v_i = \mathrm{Tr}\rho = \langle A\rangle = \langle\psi|\psi\rangle = 1. \tag{A.17}$$

If we let A be $|i\rangle\langle i'|$ we have,

$$v_{i'} = \mathrm{Tr}\rho A = \langle A\rangle = \langle\psi|A|\psi\rangle = \sum_j (\langle\psi|i'\rangle|\theta_j\rangle)(\langle\theta_j|\langle i'|\psi\rangle) \tag{A.18}$$

$$= \sum_j |(\langle i'|\langle\theta_j|)|\psi\rangle|^2. \tag{A.19}$$

Therefore,

$$v_i \geq 0 \quad \text{and} \quad \sum_i v_i = 1. \tag{A.20}$$

We now consider the concept of a density matrix independent of the preceding motivation. First let us reformulate quantum mechanics:

Any system is described by a density matrix ρ, where ρ is of the form $\sum_i v_i|i\rangle\langle i|$ and,

a) the set $|i\rangle$ is a complete orthonormal set of vectors.

b) $v_i \geq 0$.

c) $\sum_i v_i = 1$.

d) Given an operator A, the expectation of A is given by

$$\langle A \rangle = \text{Tr}\rho A. \tag{A.21}$$

Notice that,

$$\langle A \rangle = \text{Tr}\rho A \;=\; \sum_{i'} \langle i'|\rho A|i'\rangle = \sum_{i'i} v_i \langle i'|i\rangle \langle i|A|i'\rangle$$
$$=\; \sum_i v_i \langle i|A|i\rangle. \tag{A.22}$$

Since $\langle i|A|i\rangle$ = the expectation value of A in the state $|i\rangle$, it is obvious from (b), (c) and Eq. (A.22) that we can interpret the v_i as the probability that the system is in state i. If all but one of the v_i are zero, we say that the system is in a *pure state*; otherwise it is in a *mixed state*. It is easy to show that a necessary and sufficient condition for a pure state is $\rho = \rho^2$

Now here lets try the specific example of density magnetization vector in terms of the density matrix. In quantum mechanics, it is often convenient to introduce the dimensionless operator $\boldsymbol{\sigma}$, proportional to **S** by,

$$\mathbf{S} = \frac{\hbar}{2}\boldsymbol{\sigma}, \tag{A.23}$$

here, **S** represent the intrinsic magnetic moment of the electrons and the matrices which represent the three components of $\boldsymbol{\sigma}$ in the $\{|+\rangle, |-\rangle\}$ basis are called the *Pauli matrices* which are defined as,

$$\sigma_x = \begin{pmatrix} 0 & 1 \\ 1 & 0 \end{pmatrix}, \qquad \sigma_y = \begin{pmatrix} 0 & -i \\ i & 0 \end{pmatrix}, \qquad \sigma_z = \begin{pmatrix} 1 & 0 \\ 0 & -1 \end{pmatrix}. \tag{A.24}$$

Now, we shall consider an arbitrary 2×2 matrix in term of its components,

$$\rho(\mathbf{r}) = \rho = \begin{pmatrix} \rho_{11} & \rho_{12} \\ \rho_{21} & \rho_{22} \end{pmatrix}, \tag{A.25}$$

this matrix can always be written as a linear combination of the four matrices $\mathbf{I}$, $\boldsymbol{\sigma}_x, \boldsymbol{\sigma}_y, \boldsymbol{\sigma}_z$,

$$
\begin{aligned}
\boldsymbol{\rho} &= \frac{1}{2}\left[n(\mathbf{r})\mathbf{I} + m_x(\mathbf{r})\boldsymbol{\sigma}_x + m_y(\mathbf{r})\boldsymbol{\sigma}_y + m_z(\mathbf{r})\boldsymbol{\sigma}_z\right], \\
&= \frac{1}{2}\begin{pmatrix} n & 0 \\ 0 & n \end{pmatrix} \\
&\quad + \frac{1}{2}\left[\begin{pmatrix} 0 & m_x \\ m_x & 0 \end{pmatrix} + \begin{pmatrix} 0 & -im_y \\ im_y & 0 \end{pmatrix} + \begin{pmatrix} m_z & 0 \\ 0 & -m_z \end{pmatrix}\right], \\
&= \begin{pmatrix} \rho_{11} & \rho_{21} \\ \rho_{21} & \rho_{22} \end{pmatrix},
\end{aligned}
\tag{A.26}
$$

where n, m_x, m_y, and m_z are in general complex numbers and $\mathbf{I}$ is a unitary matrix defined as usual,

$$
\mathbf{I} = \begin{pmatrix} 1 & 0 \\ 0 & 1 \end{pmatrix}.
\tag{A.27}
$$

Considering Eq. (A.26) and writing n and m_i values in term of ρ_{ij} components, it is possible to write the density matrix $\boldsymbol{\rho}$ as,

$$
\boldsymbol{\rho} = \frac{\rho_{11} + \rho_{22}}{2}\mathbf{I} + \frac{\rho_{12} + \rho_{21}}{2}\boldsymbol{\sigma}_x + i\frac{\rho_{12} - \rho_{21}}{2}\boldsymbol{\sigma}_y + \frac{\rho_{11} - \rho_{22}}{2}\boldsymbol{\sigma}_z.
\tag{A.28}
$$

From this equation it is easy to identify $n(\mathbf{r})$, $m_x(\mathbf{r})$, $m_y(\mathbf{r})$, and $m_z(\mathbf{r})$ in terms of the ρ_{ij} components as follow,

$$
\begin{aligned}
n(\mathbf{r}) &= \rho_{11} + \rho_{22}, & \text{(A.29)} \\
m_x(\mathbf{r}) &= \rho_{12} + \rho_{21}, & \text{(A.30)} \\
m_y(\mathbf{r}) &= i(\rho_{11} - \rho_{21}), & \text{(A.31)} \\
m_z(\mathbf{r}) &= \rho_{11} - \rho_{22}, & \text{(A.32)}
\end{aligned}
$$

from here it is clear that $\boldsymbol{\rho}$ is Hermitian, if and only if n, m_i ($i = x, y, z$) are real.

Just to simplify the equation (A.28), we shall write it in a shorter form,

$$\rho(\mathbf{r}) = \frac{1}{2}n(\mathbf{r})\mathbf{I} + \frac{1}{2}\sum_i \left[\{\mathrm{Tr}(\rho\sigma_i)\}\,\sigma_i\right], \qquad (A.33)$$

$$\rho(\mathbf{r}) = \frac{1}{2}n(\mathbf{r})\mathbf{I} + \frac{1}{2}\sum_i m_i(\mathbf{r})\sigma_i. \qquad (A.34)$$

At this point it is important to clarify that letters in Greek represent matrices and letters in Latin represent vectors, that is just to clarify the notation that have been used. Finally, last equation can be written as,

$$\rho(\mathbf{r}) = \frac{1}{2}n(\mathbf{r})\mathbf{I} + \frac{1}{2}\mathbf{m}(\mathbf{r}) \cdot \boldsymbol{\sigma}, \qquad (A.35)$$

here it is easy to realize that $n(\mathbf{r})$ and $\mathbf{m}(\mathbf{r})$ can be written in terms of the matrix traces as follow,

$$n(\mathbf{r}) = \mathrm{Tr}\rho, \qquad (A.36)$$

$$\mathbf{m}(\mathbf{r}) = \mathrm{Tr}(\rho\boldsymbol{\sigma}). \qquad (A.37)$$

From these expressions now it is clear that we can express each component of the spin density magnetization $\mathbf{m}(\mathbf{r})$ in terms of the Pulay matrices $\boldsymbol{\sigma}$ and density matrix $\rho(\mathbf{r})$.

Appendix B

Neutron Inelastic Scattering Experiment

The experimental method explained in this appendix is the one expounded in the paper published by Yarnell J. L., et. al. [72].

The experimental dispersion curves were obtained by observing the coherent inelastic scattering of monoenergetic neutrons due to a process in which a single phonon is created in the sample crystal. If $\hbar\omega$ and $\hbar\mathbf{Q}$ are the energy and momentum transferred from the neutron to the crystal, then this "one-phonon" scattering can take place only when ω and $\mathbf{Q}$ are equal to the frequency and extended-zone wave vector of one of the phonons in the vibration spectrum of the crystal. The first-zone wave vector of the phonon is given by $\mathbf{q} = \mathbf{Q} - \mathbf{G}$, where $\mathbf{G}$ is 2π times a reciprocal lattice vector.

The conditions of the experiment were arranged to keep $\mathbf{Q}$ fixed at a desired value in the reciprocal lattice of the sample crystal, while scanning a preselected range of values of ω. A phonon of wave vector $\mathbf{Q}$ was indicated by the detection of a neutron group centred at the phonon frequency, and having a width determined by the instrumental resolution and the natural width of the phonon.

Thermal neutrons from the Los Alamos Omega West Reactor fall on the mono chromator crystal, which selects those having the desired incident energy by Bragg reflection, and directs them through the incident neutron collimator and monitor counter onto the sample crystal. Similarly, the scattered neutron collimator and analyzer crystal direct neutrons having the desired final energy into the $B^{10}F_3$ counter. The neutron momentum change is determined by the initial and final energies, and the scattering angle B. Orientation of the sample crystal with respect to the neutron momentum-change vector is accomplished

117
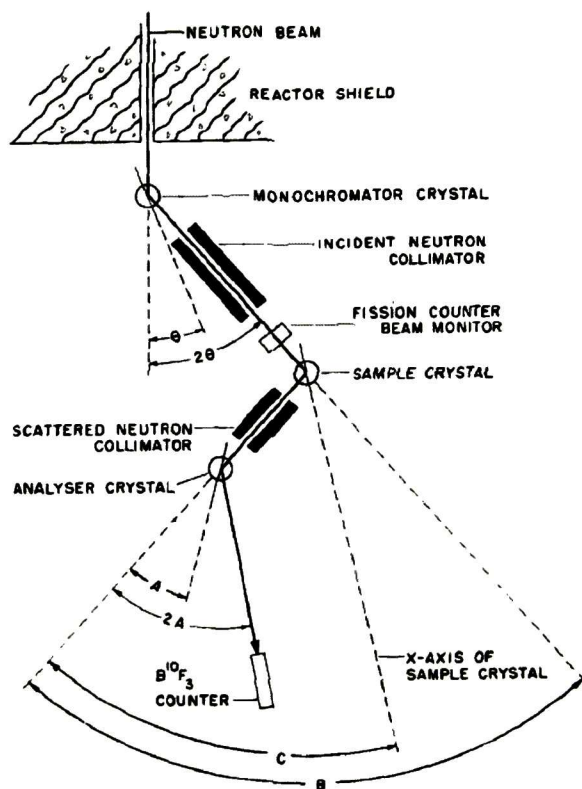
Figure B.1: Schematic diagram of the three-axis spectrometer used to determine dispersion curves in bismuth.

by adjustment of angle C. The sample crystal is initially aligned so that a selected crystallographic plane is parallel to the plane of the spectrometer, and the orientation of some axis in that plane is known in terms of the spectrometer settings. In any given measurement, the incident neutron energy is held constant, while angles A, B, and C are varied automatically according to a precomputed program to produce the desired scan. A diagram of such three-axis neutron diffraction is shown in Fig. B.1.

Appendix C

Calorimeter

In this appendix is explained the experimental setup used to measure the heat capacity at low temperatures as it was done and exposed in previous chapters.

The applied principle, $C = \delta Q/\delta T$, which describes that the heat capacity C of the sample, is determined by the pulse heat δQ supplied to the sample and the temperature rise δT, is well known. Ever since Eucken [129] in 1909 and Nernst [130] in 1910, a great number of improvements have been made to refine the experimental technique of the method. Efforts were especially made to measure small samples as well as to improve the adiabatic circumstance of samples.

In the *relaxation method*, the sample coupled with the addenda is thermally connected by a weak heat link to a heat sink held at constant temperature T_0; the heat capacity is derived from modelling the thermal response to the applied heating power. The methods are therefore beneficial both to permit removal of the heat switch and to measure the heat capacity of small sample down to very low temperature. This method also has, however, their inherent limitation. The *relaxation method* requires a properly selected heat link, or more precisely, a proper τ_1.

Here τ_1 is a time constant used to characterize the temperature equilibrium between the sample holder and the heat sink. In *relaxation method*, for example, if τ_1 becomes too long as to approach the adiabatic region, then the time required for accurate determination of τ_1 as well as the time awaited for thermal equilibrium at a new T_0 would be excessive. On the contrary, if τ_1 is too short, fast electronics are demanded and the serious problem of the "τ_2 effect" [131], arises once poor thermal connection occurs among the sample and the addenda. Since $\tau_1(T) = c_l(T)/\lambda_l(T)$ in *relaxation method*, the limitation on τ_1 results in
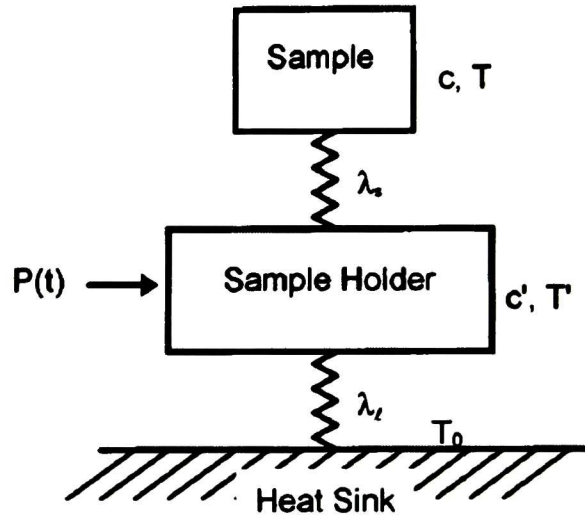
Figure C.1: Model for sample and sample holder with τ_2 effect.

restriction on the sample mass [or $c_l(T)$, more precisely] and the temperature range of measurement (see Figure C.1) [132].

The τ_2 effect, arises from the poor thermal connection between the sample and the sample holder. λ_l is the thermal conductance between the heat sink and the sample holder, and λ_s is the thermal conductance between the sample and the sample holder. Note that this model can be used to describe the dynamic temperature response of a real calorimeter simply by the assumption that the heater and the sensor are firmly attached to the sample holder with immediate thermal response, and that the thermal conductance of the sample and the holder is very large in comparison with λ_l and λ_s . Thus the heat capacities of the sensor and the heater can be included in the holder c' . It is also assumed that λ_l, λ_s , c and c' are all temperature independent within a small temperature rise.

The heat capacities in the temperature range 1.8 K - 100 K for bismuth and 2 K - 50 K for antimony were measured using a Physical Property Measurements System calorimeter Quantum Design, 6325 Lusk Boulevard, San Diego, CA. employing the *relaxation method*. The *relaxation method* is a remarkable nonadiabatic technique favoured for small sample calorimetry. A diagram is showed in Figure C.2.
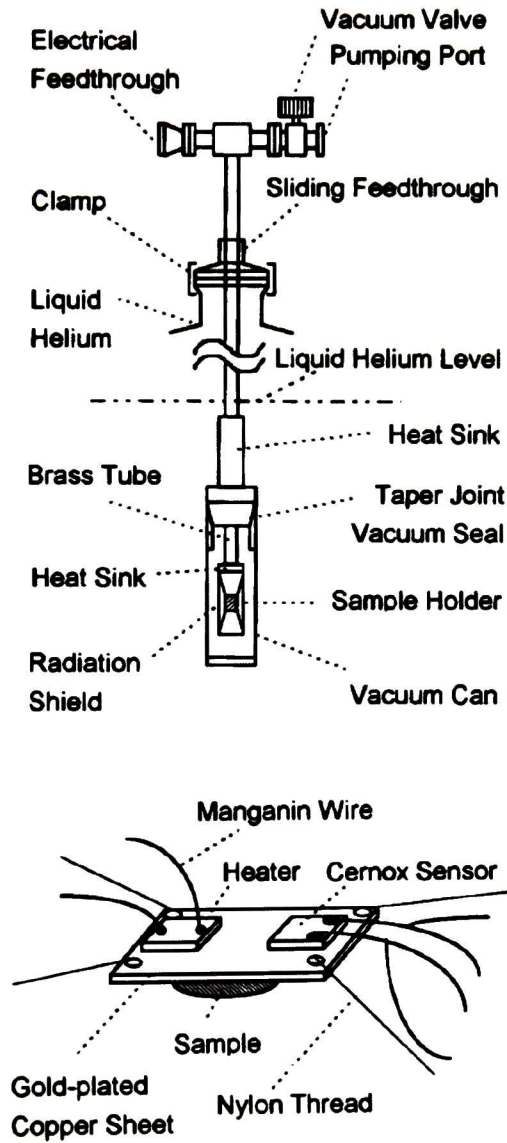
Figure C.2: Schematic diagram of immersion cryostat for heat capacity measurement (up), and Schematic drawing of simple calorimeter for CFM (down).

Appendix D

List of Publications

- L. E. Díaz-Sánchez, A. H. Romero, and X. Gonze, *Phonon band structure and interatomic force constants for bismuth: Crucial role of spin-orbit interaction*, Physical Review B **76**, 104302 (2007).

- L. E. Díaz-Sánchez, A. H. Romero, M. Cardona, R. K. Kremer, and X. Gonze, *Effect of the Spin-Orbit Interaction on the Thermodynamic Properties of Crystals: Specific Heat of Bismuth*, Physical Review Letters **99**, 165504 (2007).

- J. Serrano, R. K. Kremer, M. Cardona, G. Siegle, L. E. Díaz-Sánchez, and A. H. Romero, *Specific heat of Sb: Isotopic and spin-orbit effects from measurements and ab initio calculations*, Physical Review B **77**, 054303 (2008).

APPENDIX D. LIST OF PUBLICATIONS

Bibliography

[1] Neil W. Ashcroft and N. David Mermin, *Solid State Physics*, Saunders College Publishing (1976).

[2] Wolfram Koch, Max C. Holthausen, *A Chemist's Guide to Density Functional Theory, Second edition*, WILEY-VCH (2001).

[3] M. Born and R. Oppenheimer, *Zur Quantentheorie der Molekeln*, Annalen der Physik (Leipzig) **389**, 457 (1927).

[4] Peter Y. Yu and Manuel Cardona, *Fundamentals of Semiconductors, Physics and Materials Properties*, Springer-Verlag Berlin Heidelberg (1996).

[5] Stefano Baroni, Stefano de Gironcoli, and Andrea Dal Corso, and Paolo Giannozzi, *Phonons and related crystal properties from density-functional perturbation theory*, Reviews of Modern Physics **73**, 515 (2001).

[6] Charles Kittel, *Introduction to Solid State Physics*-7th edition, John Wiley & Sons, Inc. (1996).

[7] Richard M. Martin, *Electronic Structure, Basic Theory and Practical Methods*, Cambridge, University Press (2004).

[8] Robert G. Parr and Weitao Yang, *Density-Functional Theory of Atoms and Molecules*, Oxford University Press (1989).

[9] K. Capelle, *A Bird's-Eye View of Density-Functional Theory*, Brazilian Journal of Physics **36**, 1318 (2006).

[10] P. Hohenberg and W. Kohn, *Inhomogeneous electron gas*, Phys. Rev. **136**, B864 (1964).

[11] W. Kohn and L. J. Sham, *Self-Consistent Equations Including Exchange and Correlation Effects*, Phys. Rev. **140**, A 1133 (1965).

[12] Paolo Giannozzi, *Density Functional Theory for Electronic Structure Calculations*, unpublished.

[13] M. C. Payne, M. P. Teter, D. C. Allan, T. A. Arias, and J. D. Joannopoulos, *Iterative minimization techniques for ab initio total-energy calculations: molecular dynamics and conjugate gradients*, Reviews of Modern Physics **64**, 1045 (1992).

[14] Nathan Argaman, and Guy Makov, *Density Functional Theory an introduction*, Am. J. Phys **68**, 69 (2000).

[15] G. Kresse and J. Furthmüller, *Efficiency of ab-initio total energy calculations for metals and semiconductors using a plane-wave basis set*, Comp. Mat. Sci. **6**, 15 (1996).

[16] Péter Pulay, *Convergence acceleration of iterative sequences. the case of scf iteration*, Chemical Physics Letters **73**, 393 (1980).

[17] C. G. Broyden, *A Class of Methods for Solving Nonlinear Simultaneous Equations*, Math. Comput. **19**, 577 (1965).

[18] J. P. Perdew and A. Zunger, *Self-interaction correction to density-functional approximations for many-electron systems*, Physical Review B **23**, 5048 (1981).

[19] D. C. Langreth and J. P. Perdew, *Theory of nonuniform electronic systems. I. Analysis of the gradient approximation and a generalization that works* Phys. Rev. B **21**, 5469 (1980).

[20] D. C. Langreth and M. J. Mehl, *Beyond the local-density approximation in calculations of ground-state electronic properties*, Phys. Rev. B **28**, 1809 (1983).

[21] J. P. Perdew and Y. Wang, *Accurate and simple density functional for the electronic exchange energy: Generalized gradient approximation*, Phys. Rev. B **33**, 8800 (1986).

[22] J. P. Perdew, *Density-functional approximation for the correlation energy of the inhomogeneous electron gas*, Phys. Rev. B **33**, 8822 (1986).

[23] N. Troullier and José Luís Martins, *Efficient pseudopotentials for plane-wave calculations*, Physical Review B **43**, 1993 (1991).

[24] Matthieu Jean Verstraete, *Ab initio calculation of the structural, electronic, and superconducting properties of nanotubes and nanowires*, Thesis. Ph.D. disertation (2005).

[25] G. Kresse and D. Joubert, *From ultrasoft pseudopotentials to the project augmented-wave method*, Physical Review B **59**, 1758 (1999).

[26] D. R. Hamann, M. Schlüter, and C. Chiang, *Norm-Conserving Pseudopotentials*, Physical Review Letters **43**, 1494 (1979).

[27] David Vanderbilt, *Soft self-consistent pseudopotentials in a generalized eigenvalue formalism*, Physical Review B **41**, 7892 (1990).

[28] Leonard Kleinman and D. M. Bylander, *Efficacious Form for Model Pseudopotentials*, Physical Review Letters **48**, 1425 (1982).

[29] C. Hartwigsen, S. Goedecker, and J. Hutter, *Relativistic separable dual-space Gaussian pseudopotentials from H to Rn*, Physical Review B **58**, 3641 (1998).

[30] Martin Fuchs and Matthias Scheffler, *Ab initio pseudopotentials for electronic structure calculations of poly-atomic systems using density-functional theory*, Computer Physics Communications **119**, 67 (1999).

[31] Stefano Baroni, Paolo Giannozzi and Andre Testa, *Elastic Constants of Crystals from Linea-Response Theory* Rev. Mod. Phys. **73**, 515 (2001).

[32] Xavier Gonze, *First-principles responses of solids to atomic displacements and homogeneous electric fields: Implementation of a conjugate-gradient algorithm* Phys. Rev. B **55**, 10337 (1997).

[33] Xavier Gonze, *Interatomic Force Constants in Periodic Solids From Density Functional Pertubation Theory*, Advances in Quantum Chemistry **33**, 225 (1999).

[34] X. Gonze and C. Lee, *Dynamical matrices, Born effective charges, dielectric permittivity tensors, and interatomic force constants from density-functional perturbation theory* Phys. Rev. B **55**, 10355 (1997).

[35] H. J. Monkhorst and J. D. Pack, Phys. Rev. B **13**, 5188 (1976).

[36] T. Morisato and N. Khanna, *First-principles study of the onset of non-collinearity in Mn_n clusters: Magnetic arrangements in Mn_5 and Mn_6*, Physical Review B **72**, 014435 (2005).

[37] L. Tsetseris, *Noncollinear magnetism of iron along the tetragonal Bain transformation*, Physical Review B **72**, 012411 (2005).

[38] J. Kübler, K.-H. Höck, J. Sticht, and A. R. Williams, *Density functional theory of non-collinear magnetism*, J. Phys. F: Met. Phys. **18**, 469 (1988).

[39] J. Kübler, K.-H. Höck, and J. Sticht, *Local spin-density functional theory of noncollinear magnetism*, J. Appl. Phys. **63**, 3482 (1988).

[40] S. W. Lovesey, J. Fernández Rodríguez, J. A. Blanco, and P. J. Brown, *Phase transition, noncollinear magnetism, and magnetoelectric symmetry in gadolinium tetraboride*, Physical Review B **70**, 172414 (2004).

[41] L. M. Sandratskii, *Noncollinear magnetism in itinerant-electron system: theory and applications*, Advances in Physics **47**, 91 (1998).

[42] D. Hobbs, G. Kresse, and J. Hafner, *Fully unconstrained noncollinear magnetism within the projector augmented-wave method*, Physical Review B **62**, 11556 (2000).

[43] Tatsuki Oda, Alfredo Pasquarello, and Roberto Car, *Fully Unconstrained Approach to Noncollinear Magnetism: Application to Small Fe Clusters*, Physical Review Letters **80**, 3622 (1998).

[44] Yong Wang, Ke Xia, Zhao-Bin Su, and Zhongshui Ma, *Consistency in Formulation of Spin Current and Torque Associated with a Variance of Angular Momentum*, Physical Review Letters **96**, 066601 (2006).

[45] K. M. Rabe and J. D. Joannopoulos, *Ab initio relativistic pseudopotential study of the zero-temperature structural properties of SnTe and PbTe*, Phys. Rev. B **32**, 2302 (1985).

[46] L. Kleinman, *Relativistic norm-conserving pseudopotential* Physical Review B **21**, 2630 (1980).

[47] Giovanni B. Bachelet and M. Schlüter, *Relativistic norm-conserving pseudopotentials*, Physical Review B **25**, 2103 (1982).

[48] L. A. Hemstreet, C. Y. Fong, and J. S. Nelson, *First-principles calculations of spin-orbit splittings in solids using nonlocal separable pseudopotentials*, Physical Review B **47**, 4238 (1993).

[49] Andrea Dal Corso and Adriano Mosca Conte, *Spin-orbit coupling with ultrasoft pseudopotentials: Applicationto Au and Pt*, Physical Review B **71**, 115106 (2005).

[50] S. Goedecker, M. Teter, and J. Hutter, *Separable dual-space Gaussian pseudopotentials* Physical Review B **54**, 1703 (1996).

[51] Mark S. Hybertsen and Steven G. Louie, *Spin-orbit splitting in semiconductors and insulators from the ab initio pseudopotential*, Physical Review B **34**, 2920 (1986).

[52] J. Fernández-Rodríguez, J. A. Blanco, P. J. Brown, K. Katsumata, A Kikkawa, F. Iga, and S. Michimura, *Experimental evidence of noncollinear magnetism in gadolinium tetraboride*, Physical Review B **72**, 052407 (2005).

[53] Tatsuki Oda and Alfredo Pasquarello, *Noncollinear magnetism in liquid oxygen: A first-principles molecular dynamics study*, Physical Review B **70**, 134402 (2004).

[54] J. J. Sakurai, *Modern Quantum Mechanics*, Addison-Wesley (1994).

[55] J. J. Sakurai, *Advanced Quantum Mechanics*, Addison-Wesley (1967).

[56] E. van Lenthe, J. G. Snijders, and E. J. Baerends, *The zero-order regular approximation for relativistic effects: The effect of spinorbit coupling in closed shell molecules*, J. Chem. Phys. **105**, 6505 (1996).

[57] John P. Perdew, J. A. Chevary, S. H. Vosko, Koblar A. Jackson, Mark R. Pederson, D. J. Singh, and Carlos Fiolhais, *Atoms, molecules, solids, and surfaces: Applications of the generalized gradient approximation for exchange and correlation*, Physical Review B **46**, 6671 (1992).

[58] A. K. Geim, M. D. Simon, M. I. Boamfa, and L. O. Heflinger, Nature **400**, 323 (1999).

[59] C. A. Hoffman, J. R. Meyer, F. J. Bartoli, A. Di Venere, X. J. Yi, C. L. Hou, H. C. Wang, J. B. Ketterson, and G. K. Wong, Phys. Rev. B **48**, 11431 (1993).

[60] C. Cohen-Tannoudji: *Quantum Mechanics*, Vol. 1-2, John Wiley & Sons, 2005.

[61] X. Gonze and J.-P. Michenaud, and J.-P. Vigneron, Phys. Rev. B **41**, 11827 (1990).

[62] T. Veszprémi and M. Fehér: *Quantum Chemistry; Fundamentals to Applications*. Kluwer, New York, (1999).

[63] M. D. Jones, J. C. Boettger, R. C. Albers, and D. J. Singh, Phys. Rev. B **61**, 4644 (2000).

[64] N. Richard, S. Bernard, F. Jollet, and M. Torrent, Phys. Rev. B **66**, 235112 (2002).

[65] J. Bouchet, F. Jollet, G. Zerah, Phys. Rev. B **74**, 134304 (2006).

[66] D. M. Fritz et al., Science **315**, 633 (2007).

[67] É. D. Murray, S. Fahy, D. Prendergast, T. Ogitsu, D. M. Fritz and D.A. Reis, Phys. Rev. B **75**, 184301 (2007).

[68] X. Gonze, J.-M. Beuken, R. Caracas, F. Detraux, M. Fuchs, G.-M. Rignanese, L. Sindic, M. Verstraete, G. Zerah, F. Jollet, M. Torrent, A. Roy, M. Mikami, P. Ghosez, J. Y. Raty, and D. C. Allan, Comput. Mater. Sci. **25**, 478 (2002).

[69] X. Gonze, G.-M. Rignanese, M. Verstraete, J.-M. Beuken, Y. Pouillon, R. Caracas, F. Jollet, M. Torrent, G. Zerah, M. Mikami, P. Ghosez, Veithen M., J. Y. Raty, V. Olevano, F. Bruneval, L. Reining, R. Godby, G. Onida, D. R. Hamann, and D. C. Allan, Z. Cristall. **220**, 558 (2005).

[70] The *ABINIT* code is a common project of the Université Catholique de Louvain, Corning Incorporated, and other contributors http://www.abinit.org.

[71] H. J. Monkhorst and J. D. Pack, Phys. Rev. B **13**, 5188 (1976).

[72] J. L. Yarnell, J. L. Warren, R. G. Wenzel, and S. H. Koenig, IBM J. of research and development **8**, 234 (1964).

[73] D. B. Smith, Los Alamos Report No. 3773, 1967 (unpublished).

[74] M. Methfessel and A. T. Paxton, Phys. Rev. B **40**, 3616 (1989).

[75] Eeuwe S. Zijlstra, Larisa L. Tatarinova, and Martin E. Garcia, Phys. Rev. B **74**, 220301(R) (2006).

[76] Ph. Ghosez, X. Gonze, and J.-P. Michenaud, Ferroelectrics **206-207**, 205 (1998).

[77] Ph. Ghosez, X. Gonze, and J.-P. Michenaud, Ferroelectrics **194**, 39 (1997).

[78] M. Cardona, R. K. Kremer, M. Sanati, S. K. Estreicher, and T. R. Anthony, Solid State Commun. **133**, 465 (2005).

[79] A. Gibin, G. G. Devyatykh, A. V. Gusev, R. K. Kremer, M. Cardona, and H.-J. Pohl, Solid State Commun. **133**, 569 (2005).

[80] J. Serrano, R. K. Kremer, M. Cardona, G. Siegle, A. H. Romero, and R. Lauck, Phys. Rev. B **73**, 094303 (2006).

[81] M. Cardona, R. K. Kremer, R. Lauck, G. Siegle, J. Serrano, and A. H. Romero, Phys. Rev. B **76**, 075211 (2007).

[82] M. Cardona, R. K. Kremer, R. Lauck, G. Siegle, J. Serrano, and A. H. Romero (to be published).

[83] M. M. Elcombe, Proc. R. Soc. A **300**, 210 (1967).

[84] P. A. Varotsos and K. D. Alexopoulos, *Thermodynamics of Point Defects and Their Relation with Bulk Properties*, NorthHolland, Amsterdam, 1986 , p. 15.

[85] Landolt-Brnstein, *Landolt-Brnstein Tables*, New Series, Group III, **17**, Pt. F, edited by G. Nimtz Springer, Berlin (1983), p. 155.

[86] C. Lee and X. Gonze, Phys. Rev. B **51**, 8610 (1995).

[87] R. Bellisent, C. Bergman, A. Pellegati, R. Ceolin, and J. P. Gaspard, J. Non-Cryst. Solids **1263**, 97 (1987).

[88] L. E. Díaz-Sánchez, A. H. Romero, and X. Gonze, *Phonon band structure and interatomic force constants for bismuth: Crucial role of spin-orbit interaction*, Phys. Rev. B **76** 104302 (2007).

[89] For a compilation of heat capacity data of polycrystalline Bi published before 1964, see Y. S. Touloukian and E. H. Buyco, Thermophysical Properties of Matter (Plenum, New York, 1970), Vol. 4.

[90] P. H. Keesom, Phys. Rev. **96**, 897 (1954).

[91] P. Franzosini and K. Clusius, Z. Naturforsch. **19a**, 1430 (1964).

[92] T. C. Cetas, J. C. Holste, and C. A. Swenson, Phys. Rev. B **182**, 679 (1969).

[93] D. G. Archer, J. Chem. Eng. Data **40**, 1015 (1995)

[94] Measurements below 2 K have been carried out by N. E. Phillips, Phys. Rev. **118**, 644 (1960); and subsequently by H. K. Collan, M. Krusius, and G. R. Pickett, Phys. Rev. B **1**, 2888 (1970) in order to establish the electronic and the nuclear quadrupole contribution to the heat capacity of Bi.

[95] L. J. Norrby, Journal of Chemical Education **68**, 110 (1991).

[96] P. Pyykko, Chem. Rev. **88**, 563 (1988).

[97] M. Sanati, S. K. Estreicher, and M. Cardona, Solid State Commun. **131**, 229 2004.

[98] R. K. Kremer, M. Cardona, E. Schmitt, J. Blumm, S. K. Estreicher, M. Sanati, M. Bockowski, I. Grzegory, T. Suski, and A. Jezowski, Phys. Rev. B **72**, 075209 2005.

[99] J. Donohue, The Structures of the Elements Wiley, New York, 1974.

[100] X. Wang, K. Kunc, I. Loa, U. Schwarz, and K. Syassen, Phys. Rev. B **74**, 134305 (2006).

[101] G. A. Saunders and Y. K. Yognurtu, Phys. Rev. B **30**, 5734 (1984).

[102] L. E. Díaz-Sánchez, A. H. Romero, M. Cardona, R. K. Kremer, and X. Gonze, Phys. Rev. Lett. **99**, 165504 (2007).

[103] V. V. Nogteva, I. E. Paukov, and P. G. Strelkov, Sov. Phys. Solid State **7**, 1884 (1966).

[104] H. V. Culbert, Phys. Rev. **157**, 560 (1967).

[105] W. A. Taylor, D. C. McCollum, B. C. Passenheim, and H. W. White, Phys. Rev. **161**, 652 (1967).

[106] W. DeSorbo, Acta Metall. **1**, 503 (1953).

[107] D. C. McCollum and W. A. Taylor, Phys. Rev. **156**, 782 (1967).

[108] H. K. Collan, M. Krusius, and G. R. Pickett, Phys. Rev. B **1**, 2888 (1970).

[109] K. G. Ramanathan and T. M. Srinivasan, Phys. Rev. **99**, 442 (1955).

[110] I. N. Kalinina and P. G. Strekov, Sov. Phys. JETP **7**, 426 (1958).

[111] X. Gonze, G.-M. Rignanese, and R. Caracas, Z. Kristallogr. New Cryst. Struct. **220**, 458 (2005).

[112] R. I. Sharp and E. Warming, J. Phys. F: Met. Phys. **1**, 570 (1971).

[113] F. Herman and S. Skillman, *Atomic Structure Calculations*, Prentice-Hall, Anglewood Cliffs, NJ, (1963).

[114] J. Serrano, K. Syassen, A. H. Romero, A. Bosak, and M. Krisch, *unpublished*.

[115] K. Balasubramanian, J. Chem. Phys **89**(10) , 6310 (1988).

[116] Songbook Lee, et. al., Physical Review B **39**(8) 4916 (1989).

[117] Taketoshi Nakao, David A. Dixon, and Han Chen, *Electronic Structure of Palladium Dimer from Density Functional Theory*, J. Phys Chem **97**, 12665 (1993).

[118] J. Kielhorn, C. Melber, D. Keller, and Inge Mangelsdorf, *Palladium - A review of exposure and effects to human health*, Int. J. Hyg. Env. Health **205**, 417 (2002).

[119] T. O. Strandberg, C. M. Canali, and A. H. MacDonald, *Calculation of Chern number spin Hamiltonians for magnetic nano-clusters by DFT methods*, Physical Review B **77**, 174416 (2008).

[120] Lars. F. Lundegaard, Gunnar Weck, Malcolm I. McMahon, Serge Desgreniers, and Paul Loubeyre, *Observation of an O_8 molecular lattice in the ε phase of solid oxygen*, Nature **443** 201, 2006.

[121] J. B. Neaton and N. W. Ashcroft, *Low-Energy Linear Structures in Dense Oxygen: Implications for the ε Phase*, Physical Review Letters **88**, 205503 (2002).

[122] Eric Cancès, *Self-consistent field algorithms for Kohn-Sham models with fractional occupation numbers*, Journal of Chemical Physics **114**, 10616 (2001).

[123] Eric Canès, Konstantin N. Kudin, Gustavo E. Scuseria, and Gabriel Turinici, *Quadratically convergent algorithm for fractional occupation numbers in density functional theory*, Journal of Chemical Physics **118**, 5364 (2003).

[124] Bulumoni Kalita and Ramesh C. Deka, *Stability of small Pd_n (n=1-7) clusters on the basis of structural and electronic properties: A density functional approach*, Journal of Chemical Physics **127**, 244306 (2007).

[125] F. W. Averill and G. S. Painter, *Steepest-descent determination of occupation numbers and energy minimization in the local-density approximation*, Physical Review B **46**, 2498 (1992).

[126] P. E. Blochl, *Projector augmented-wave method* **50**, 17053 (1994).

[127] N. A. W. Holzwarth, A. R. Tackett, and G. E. Matthews, *A Projector Augmented Wave (PAW) code for electronic structure calculations, PartI: atompaw for generation atom-centered functions*, Computer Phys. Comm. **135**, 329 (2001)

[128] Marc Torrent, Francois Jollet, Francois Bottin, Gilles Zerah, and Xavier Gonze, *Implementation of the projector augmented-wave method in the ABINIT code: Application to the study of iron under pressure*, Computational Materials Science **42**, 337 (2008).

[129] A. Eucken, Z. Phys. **10**, 586 1909.

[130] W. Nernst, Sitzb. Kgl. Preuss. Akad. Wiss. **12**, 261 1910.

[131] R. Bachmann, F. J. DiSalvo, Jr., T. H. Geballe, R. L. Greene, R. E. Howard, C. N. King, H. C. Kirsch, K. N. Lee, R. E. Schwall, H. U. Thomas, and R. B. Zubeck, Rev. Sci. Instrum. **43**, 205 1972 .

[132] G. R. Steward, Rev. Sci. Instrum. **54**, 1 1983 .

[133] R. P. Feynman, *Statistical Mechanics*, Benjamin/Cummings, Reading, MA (1972)

EL JURADO DESIGNADO POR LA UNIDAD QUERÉTARO DEL CENTRO DE INVESTIGACIÓN Y DE ESTUDIOS AVANZADOS DEL INSTITUTO POLITÉCNICO NACIONAL, APROBÓ LA TESIS DOCTORAL DEL C. LUIS ENRIQUE DÍAZ SÁNCHEZ TITULADA: ANISOTROPÍAS MAGNÉTICAS DESDE PRIMEROS PRINCIPIOS, FIRMAN AL CALCE DE COMÚN ACUERDO LOS INTEGRANTES DE DICHO JURADO, EN LA CIUDAD DE QUERÉTARO, QRO., A LOS VEINTITRÉS DÍAS DE ENERO DE 2009.

DR. ALDO HUMBERTO ROMERO CASTRO

PROF. XAVIER GONZE

DR. SERGIO JOAQUÍN JIMÉNEZ SANDOVAL

DR. ALBERTO HERRERA GÓMEZ

DR. MARIO ENRIQUE RODRÍGUEZ GARCÍA